Star Formation[1]

Kohji Tomisaka
National Astronomical Observatory Japan

May 8, 2007

[1] http://yso.mtk.nao.ac.jp/~tomisaka/Lecture_Notes/StarFormation/3.pdf

version 0.5: August 5, 2001
version 1.0: August 30, 2001
version 2.0: November 8, 2003
version 3.0: June 1, 2004

Contents

Chapter 1

Introduction

1.1 Interstellar Matter

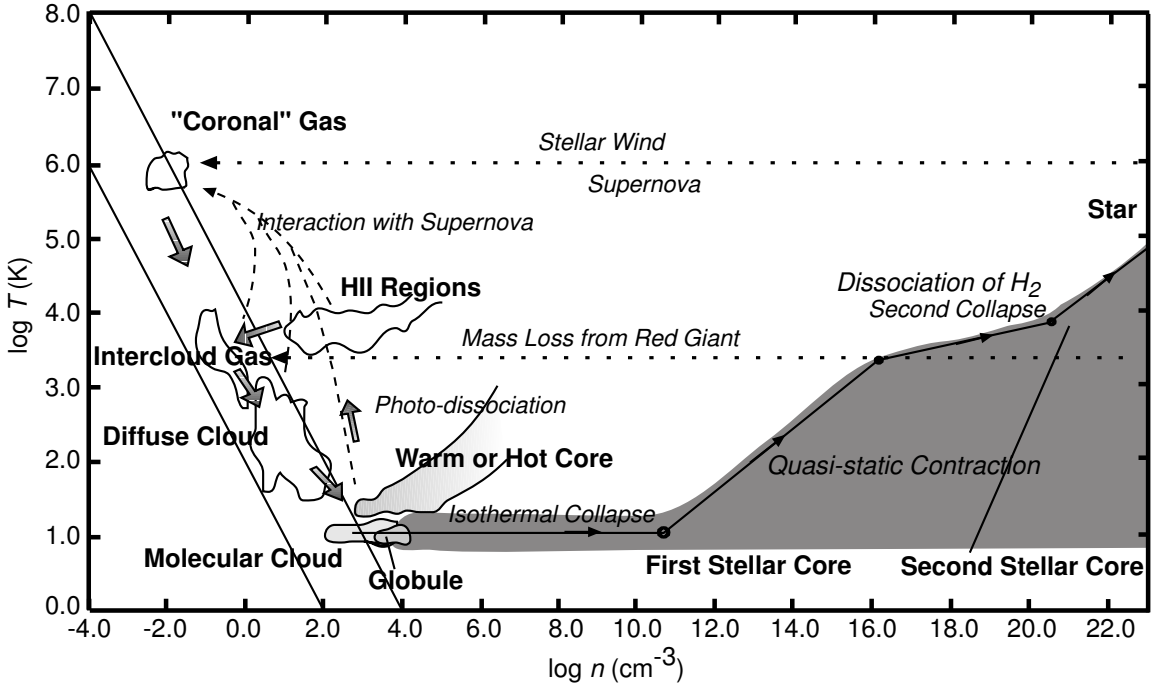

Figure 1.1: Multiphases of the interstellar medium. The temperature and number density of gaseous objects of the interstellar medium in our Galaxy are summarized. Originally made by Myers (1978), reconstructed by Saigo (2000).

Figure 1.1 shows the temperature and number density of gaseous objects in our Galaxy. Cold interstellar medium forms molecular clouds ($T \sim 10$K) and diffuse clouds ($T \sim 100$K). Warm interstellar medium $10^3\mathrm{K} \lesssim T \lesssim 10^4\mathrm{K}$ are thought to be pervasive (wide-spread). HII regions are ionized by the Ly continuum photons from the nearby early-type stars. There are coronal (hot but tenuous) gases with $T \sim 10^6$ K in the Galaxy, which are heated by the shock fronts of supernova remnants. Pressures of these gases are in the range of $10^2\mathrm{K\,cm^{-3}} \lesssim p \lesssim 10^4\mathrm{K\,cm^{-3}}$, except for the HII regions. This may suggest that gases are in the pressure equilibrium.

In this figure, a theoretical path from the molecular cloud core to the star is also shown. We will see the evolution more closely in Chapter 4.

Globally, the molecular form of Hydrogen H_2 is much abundant inside the Solar circle, while the atomic hydrogen HI is more abundant than molecular H_2 in the outer Galaxy. In Figure 1.2 (left), the radial distributions of molecular and atomic gases are shown. The right panel shows similar distributions for four typical external galaxies (M51, M101, NGC6946, and IC342). This indicates these distributions are similar with each other. HI is distributed uniformly, while H_2 density increases greatly reaching the galaxy center. In other words, only in the region where the total (HI+H_2) density exceeds some critical value, H_2 molecules are distributed.

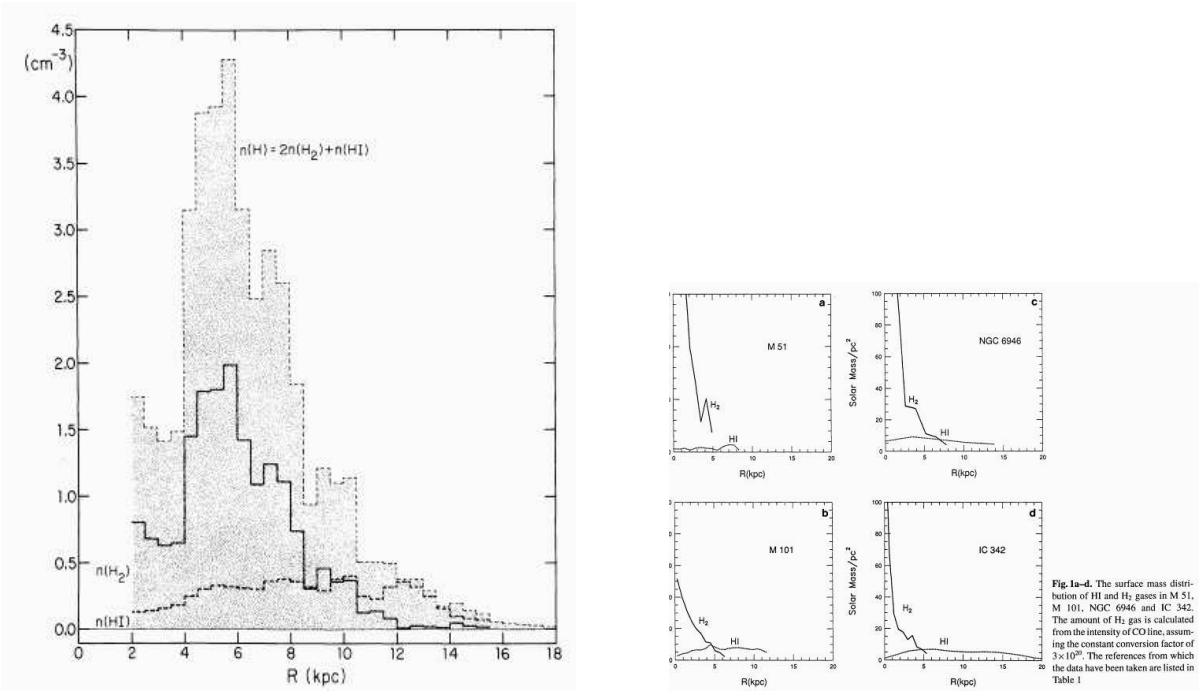

Figure 1.2: Radial distribution of H_2 (solid line) and HI (dashed line) gas density. (Left:) our Galaxy. Converting from CO antenna temperature to H_2 column deity, $n(\mathrm{CO})/n(\mathrm{H_2}) = 6 \times 10^{-5}$ is assumed. Taken from Gordon & Burton (1976). (Right:) Radial distribution of H_2 and HI gas for external galaxies. The conversion factor is assumed constant $X(\mathrm{H_2/CO}) = 3 \times 10^{20} \mathrm{H_2/K\,km\,s^{-1}}$. Taken from Honma et al (1995).

1.2 Case Study — Taurus Molecular Clouds

Figure 1.3 (*left*) shows the ^{13}CO total column density map of the Taurus molecular cloud (Mizuno et al 1995) whose distance is 140 pc far from the Sun. Since ^{13}CO contains ^{13}C, a rare isotope of C, the abundance of ^{13}CO is much smaller than that of ^{12}CO. Owing to the low abundance, the emission lines of ^{13}CO are relatively optically thiner than that of ^{12}CO. Using ^{13}CO line, we can see deep inside of the molecular cloud. The distributions of T Tauri stars and ^{13}CO column density coincide with each other. Since T Tauri stars are young pre-main-sequence stars with $M \sim 1 M_\odot$, which are in the Kelvin-Helmholtz contraction stage and do not reach the main-sequence Hydrogen burning stage, it is shown that stars are newly formed in molecular clouds.

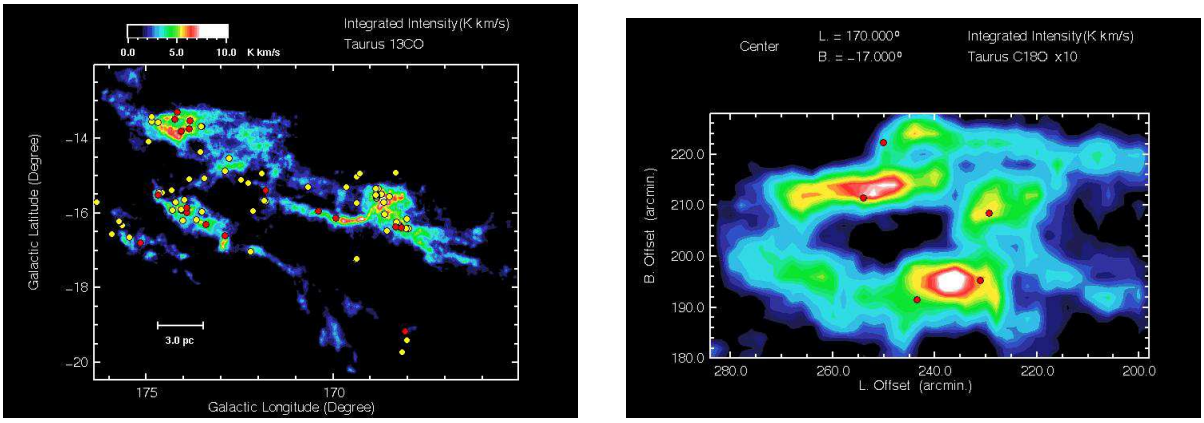

Figure 1.3: (*Left*) ^{13}CO total column density map of the Taurus molecular cloud (Mizuno et al 1995). Taken from their home page with URL of http://www.a.phys.nagoya-u.ac.jp/nanten/taurus.html (in Japanese). T Tauri stars, which are thought to be pre-main-sequence stars in the Kelvin-Helmholtz contraction stage, are indicated by bright spots. (*Right*) C^{18}O map of Heiles cloud 2 region in the Taurus molecular cloud (Onishi et al. 1996). This shows clearly that the cloud is composed of a number of high-density regions.

Since ^{18}O is much more rare isotope (^{18}O/^{16}O $\ll$ ^{13}C/^{12}C), the distribution of much higher-density gases is explored using C^{18}O lines. Figure 1.3 (right) shows C^{18}O map of Heiles cloud 2 in the Taurus molecular cloud by Onishi et al (1996). This shows us that there are many molecular cloud cores which have much higher density than the average. Many of these molecular cloud cores are associated with IRAS sources and T Tauri stars. It is shown that star formation occurs in the molecular cloud cores in the molecular cloud. They found 40 such cores in the Taurus molecular cloud. Typical size of the core is ~ 0.1 pc and the average density of the core is as large as $\sim 10^4 \mathrm{cm}^{-3}$. The mass of the C^{18}O cores is estimated as $\sim 1 - 80 M_\odot$.

H^{13}CO$^+$ ions are excited only after the density is much higher than the density at which CO molecules are excited. H^{13}CO$^+$ ions are used to explore the region with higher density than that observed by C^{18}O. Figure 1.4 shows the map of cores observed by H^{13}CO$^+$ ions. The cores shown in the lower panels are accompanied with infrared sources. The energy source of the stellar IR radiation is thought to be maintained by the accretion energy. That is, since the gravitational potential energy at the surface of a protostar with a radius R_* and a mass M_* is equal to $\Phi \simeq -GM_*/R_*$, the kinetic energy of the gas accreting on the stellar surface is approximately equal to $\sim GM_*/R_*$. The energy inflow rate owing to the accretion is $(\sim GM_*/R_*) \times \dot{M} \sim (GM_*/R_*) \times A(c_s^3/G)$, where $\dot{M} = A(c_s^3/G)$ is the mass accretion rate. In the upper panels, the cores without IR sources are shown. This core does not show accretion but collapse. That is, before a proto**star** is formed, the core itself contract owing to the gravity, which is explained closely in chapter 4.

In Figure 1.4, H^{13}CO$^+$ total column density maps of the C^{18}O cores are shown. Cores in the lower panels have associated IRAS sources, while the cores in the upper panels have no IRAS sources. Since the IRAS sources are thought to be protostars or objects in later stage, the core seems to evolve from that without an IRAS sources to that with an IRAS source. From this, the core with an IRAS source is called **protostellar core**, which means that the cores contain protostars. On the other hand, the core without IRAS source is called pre-protostellar core or, in short, **pre-stellar core**.

Figure 1.4 shows that the prestellar cores are less dense and more extended than the protostellar core. This seems to suggest the density distribution around the density peak changes between before

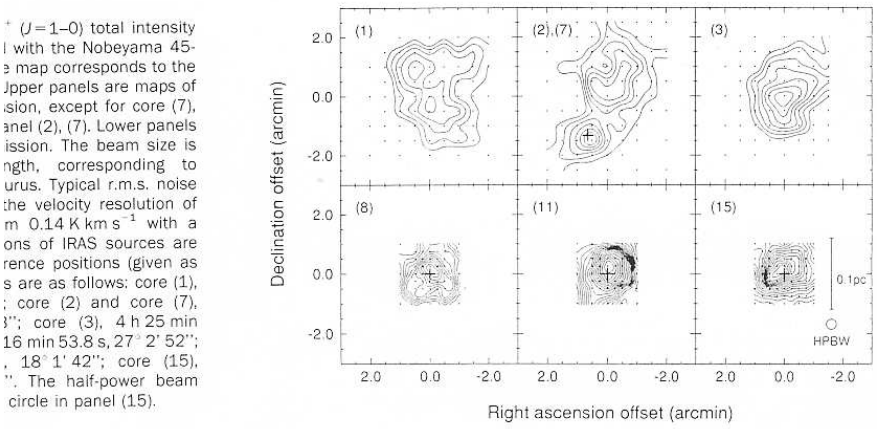

$^+$ (J=1–0) total intensity
l with the Nobeyama 45-
e map corresponds to the
Upper panels are maps of
sion, except for core (7),
anel (2), (7). Lower panels
ission. The beam size is
ngth, corresponding to
urus. Typical r.m.s. noise
the velocity resolution of
m 0.14 K km s^{-1} with a
ons of IRAS sources are
rence positions (given as
s are as follows: core (1),
; core (2) and core (7),
3"; core (3), 4 h 25 min
16 min 53.8 s, 27° 2' 52";
, 18° 1' 42"; core (15),
". The half-power beam
circle in panel (15).

Figure 1.4: Pre-protostellar vs protostellar cores ($H^{13}CO^+$ map). Upper panel shows the $C^{18}O$ cores without associated IRAS sources. Lower panel shows the cores with IRAS sources. Taken from Fig.1 of Mizuno et al. (1994)

and after the protostar formation.

1.3 T Tauri Stars

T Tauri stars are observationally late-type stars with strong emission lines and irregular light variations associated with dark or bright nebulosities. T Tauri stars are thought to be low-mass pre-main-sequence stars, which are younger than the main-sequence stars. Since these stars are connecting between protostars and main-sequence stars, they attract attention today. More massive counterparts are called Herbig Ae-Be stars. They are doing the Kelvin-Helmholtz contraction in which the own gravitational energies released as it contracts gradually and this is the energy source of the luminosity. Many emission lines are found in the spectra of T Tauri stars. WTTS (Weak emission T Tauri Stars or Weak line T Tauri Stars) and CTTS (Classical T Tauri Stars) are classified by their equivalent widths (EWs) of emission lines. That is, the objects with an EW of Hα emission $<$ 1nm = 10Å is usually termed a WTTS. Figure 1.5 is the HR diagram ($T_{\rm eff} - L_{\rm bol}$) of T Tauri stars in Taurus-Auriga region (Kenyon & Hartman 1995). WTTSs distribute near the main-sequence and CTTSs are found even far from the main-sequence. A number of theoretical evolutional tracks for pre-main-sequence stars with $M \sim 0.1M_\odot - 2.5M_\odot$ are shown in a solid line, while the isochorones for ages of 10^5yr, 10^6yr, and 10^7yr are plotted in a dashed line. Vertical evolutional paths are the Hayashi convective track. Since D=^{2}H has a much lower critical temperature (and density) for a fusion nuclear reaction to make He than ^{1}H, Deuterium begins to burn before reaching the zero-age-main sequence. This occurs near the isochrone for the age of 10^5yr and some activities related to the ignition of Deuterium seem to make the central star visible (Stahler 1983).

Disk Frequency

Infrared studies of T Tauri stars in star-forming regions have suggected that initial disk frequency if rather high and that the disk lifetimes are relatively short $3 - 15$Myr. From JHKL photometry, Haish, Lada, & Lada (2001) obtained the fraction of disk-bearing stars for 6 star firmation regions. L band excess emission indicates an accompanied disk. The fraction is a decreasing function of age

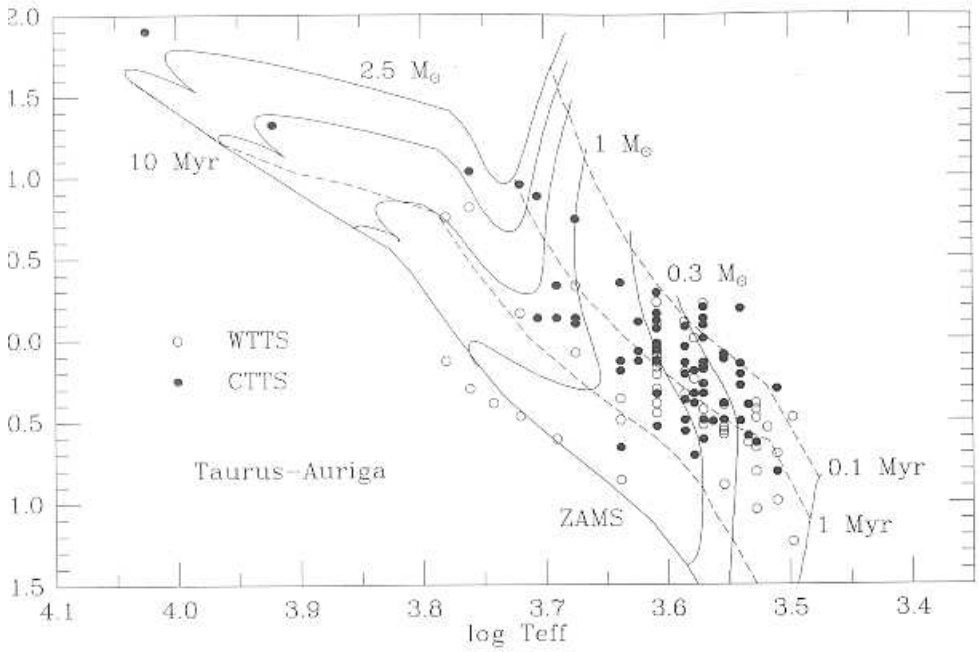

1.2. HR diagram positions of young stars lying within the Taurus–Auriga molec-
cloud complex (Figure 1.1). For comparison, theoretical evolutionary tracks for
main-sequence stars of masses 2.5, 2.0, 1.5, 1.0, 0.5, 0.3, and 0.1 $M_\odot$ are shown.
dashed lines are isochrones for ages of 10^5, 10^6, and 10^7 yr (0.1, 1, and 10 Myr),
the hydrogen-fusion 'zero-age main sequence' or ZAMS shown as the lowest
running from upper left to lower right. The open circles refer to weak-emission
auri stars (WTTS; see text), while the filled circles denote the positions of the
sical T Tauri stars (CTTS). Stellar properties taken from Kenyon & Hartmann
5); evolutionary tracks are from D'Antona & Mazzitelli (1994).

Figure 1.5: HR diagram of T Tauri stars. Many emission lines are found in the spectra of T Tauri stars. WTTS (Weak Emission T Tauri Stars) and CTTS (Classical T Tauri Stars) are classified by the equivalent widths of emission lines. That is, the objects with an EW of Hα emission $<$ 1nm is usually termed a WTTS. Taken from Fig.1.2 of Hartmann (1998).

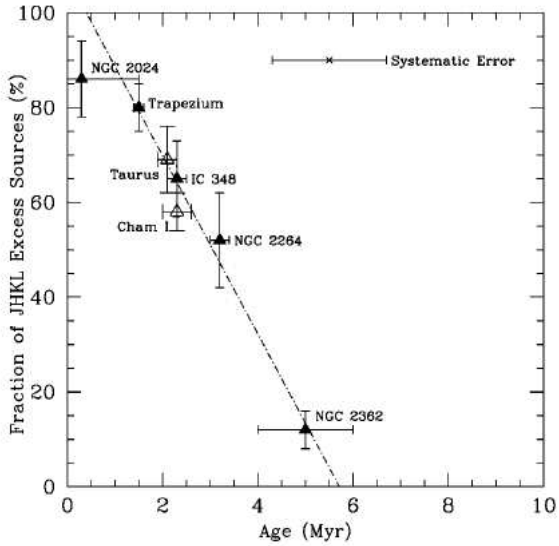

Figure 1.6: Fractions of IR excess sources in respective clusters are plotted againt the age of the clusters.

of the cluster as in Figure 1.6. This figure shows clearly that the disk fraction is initially very high ($\gtrsim$80%) and rapidly decreases with increasing cluster age. In 3 Myr a half of the disk stars lose their disks. Overall disk lifetime is estimated as $\sim$ 6Myr.

1.4 Spectral Energy Distribution (SED)

A tool to know the process of star formation is provided by the spectral energy distribution (SED) mainly in the near- and mid-infrared light. T Tauri stars and protostars have typical respective SEDs. IR SEDs of T Tauri stars were classified into three as Class I, Class II, and Class III, from a standpoint of relative importance of the radiation from a dust disk to the stellar black-body radiation. Today, the classification is extended to the protostars, which is precedence of the T Tauri stars, and they are called Class 0 objects. (Unfortunately, there is no zero in Roman numerals.) In Figure 1.7, typical SEDs and models of emission regions are shown.

1. Class III is well fitted by a black-body spectrum, which shows the energy mainly comes from a central star. This SED is observed in the weak-line T Tauri stars. Although T Tauri stars show emission lines of such as the Hydrogen Balmar sequence, the weak-line T Tauri stars do not show prominent emission lines, which indicates the amount of gas just outside the star (this seems to be supplied by the accretion process) is small. In this stage, a disk has been disappeared or an extremely less-massive disk is still alive.

2. Class II SED is fitted by a single-temperature black-body plus excess IR emission. This shows that there is a dust disk around a pre-main sequence star and it is heated by the radiation from a central star. The width of the spectrum of the disk component is much wider than that expected from a single-temperature black-body radiation. Thus, the disk has a temperature gradient which decreases with increasing the distance from the central star. In this stage, the dust disk is more massive than that of Class III sources. Classical T Tauri stars have such SEDs.

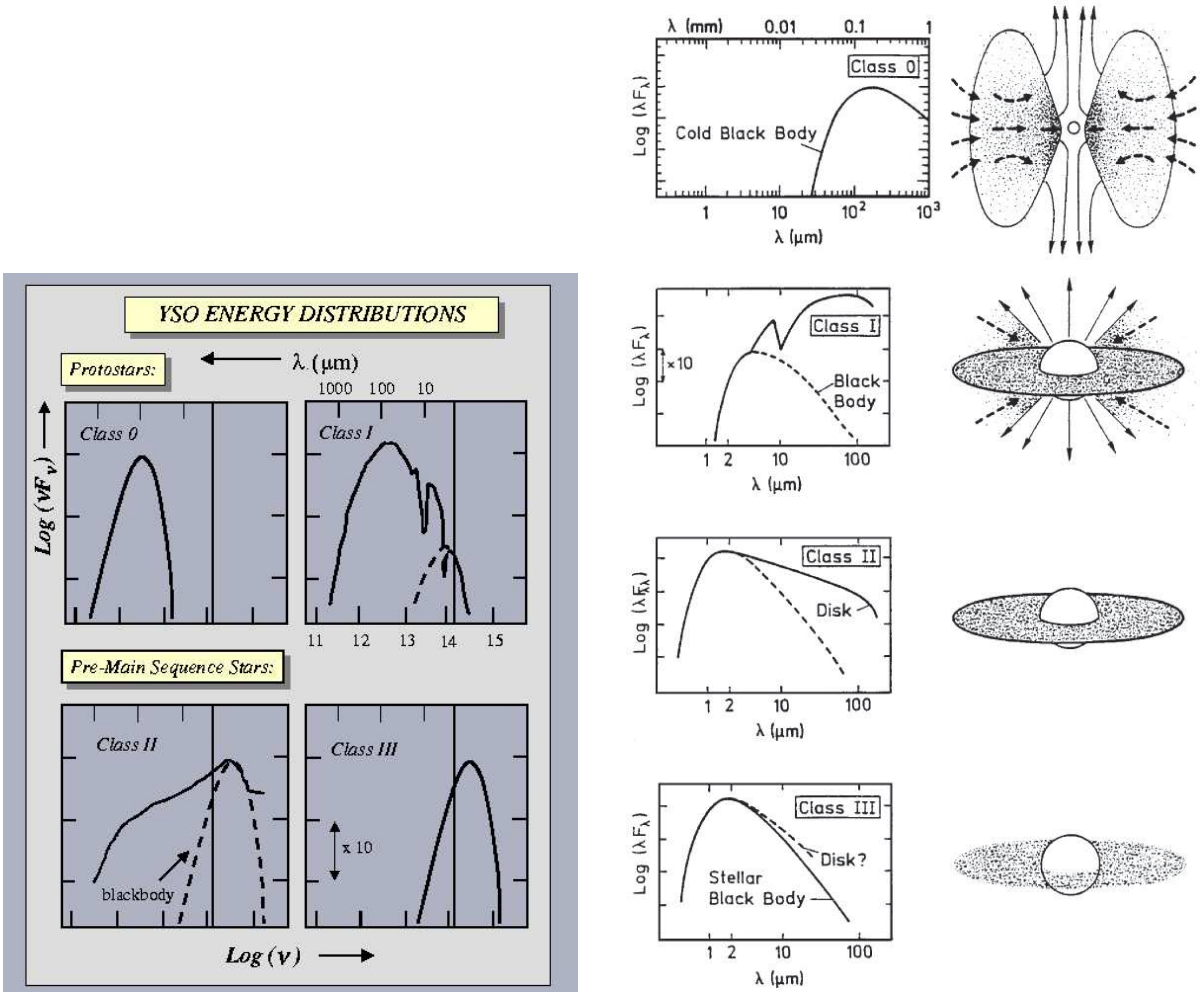

Figure 1.7: Spectral Energy Distribution (SED) of young stellar objects (YSOs) and their models. (*Left*:) $\nu - \nu F_\nu$ plot taken from Lada (1999). (*Right*:) $\lambda - \lambda F_\lambda$ plot taken from André (1994)

3. In Class I SED, the mid infrared radiation which seems to come from the dust envelope is predominant over the stellar black-body radiation. Since the stellar black-body radiation seems to escape at least partially from the dust envelope, a relatively large solid angle is expected for a region where the dust envelope does not intervene.

4. Class 0 SED seems to be emitted by an isothermal dust with $\sim$ 30K. The protostar seems to be completely covered by gas and dust and is obscured with a large optical depth by the dust envelope. No contribution can be reached from the stellar-black body radiation.

The reason why the emission from the disk becomes wide in the spectral range is understood (Fig.1.8) as follows: Temperature of the disk is determined by a balance of heating and cooling. Assuming the disk is geometrically thin but optically thick, the cooling per unit area is given by the equation of the black-body Planck radiation. Therefore, the temperature is determined by the heating predominantly by viscous heating and extra heating by the radiation from the central star.

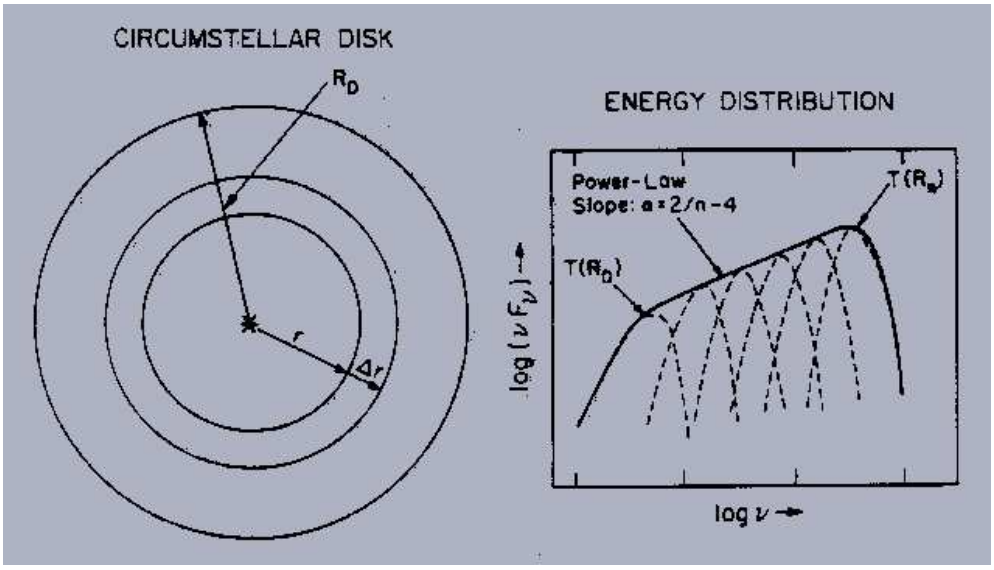

Figure 1.8: Explanation for the spectral index of the emission from a geometrically thin but optically thick disk. Taken from Fig.16 of Lada (1999).

The flux density emitted by the disk is given by

$$\nu F_\nu \sim \int \nu \pi B_\nu[T(r)] 2\pi r dr \sim r(T \text{ or } \nu)^2 \nu B_\nu. \tag{1.1}$$

Assuming the radial distribution of temperature as

$$T = T_0 \left(\frac{R}{R_0}\right)^{-q}, \tag{1.2}$$

($q = 3/4$ for the standard accretion disk) and taking notice that each temperature in the disk radiates at a characteristic frequency $\nu \propto T$ (the Wien's law for black-body radiation)

$$\nu F_\nu \sim r^2 \nu B_\nu \propto \nu^4 T^{-2/q} \propto \nu^{4-2/q}, \tag{1.3}$$

where we used the fact that the peak value of $B_\nu \propto \nu^3$. Therefore, it is shown that

$$\nu F_\nu \propto \nu^n; \qquad n = 4 - \frac{2}{q}. \tag{1.4}$$

As shown in the previous section, we have no young **stellar** objects found by IR before a protostar is formed. These kind of objects (pre-protostellar core) are often called Class -1. The classification was originally based on the SED and did not exactly mean an evolution sequence. However, today YSOs are considered to evolve as the sequence of the classes: Class -1 → Class 0 → Class I → Class II → Class III → main-sequence star.

1.5 Protostars

1.5.1 B335

B335 is a dark cloud (Fig.1.9) with a distance of $D \simeq 250$pc. Inside the dark cloud, a Class 0 IR source is found. The object is famous for the discovery of gas infall motion. In Figure 1.10, the

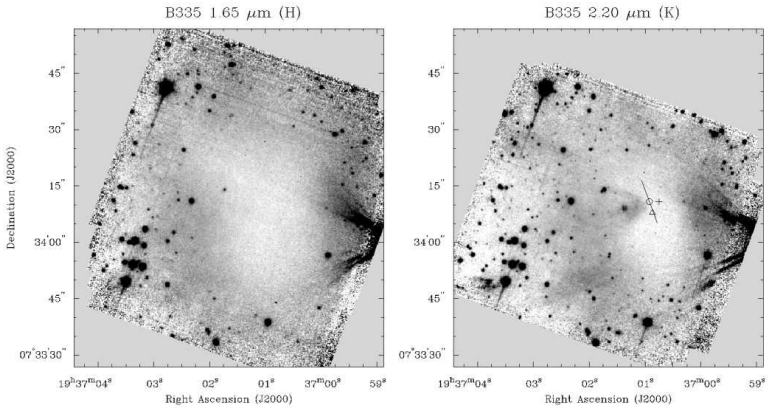

Figure 1.9: Near infrared images of B335, which is Class 0 source.

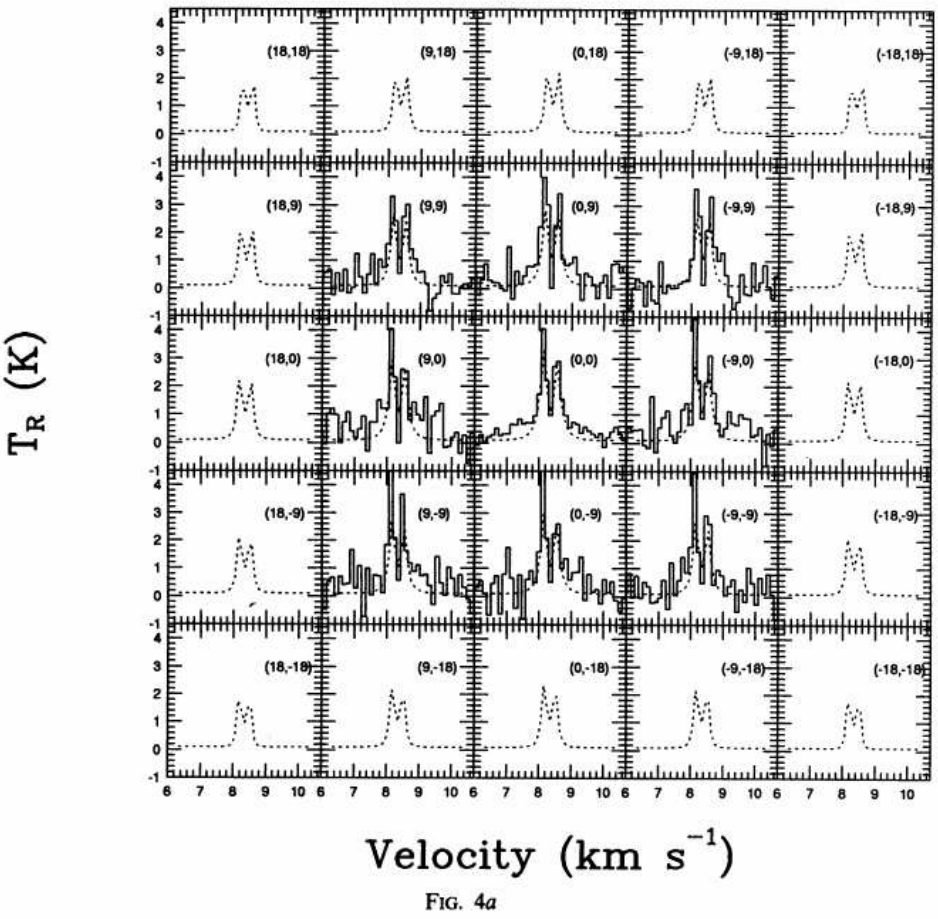

Figure 1.10: Line profile of CS $J = 2 - 1$ line radio emission. Model spectra illustrated in a dashed line (Zhou 1995) are overlaid on to the observed spectra in a solid line (Zhoug et al 1993).

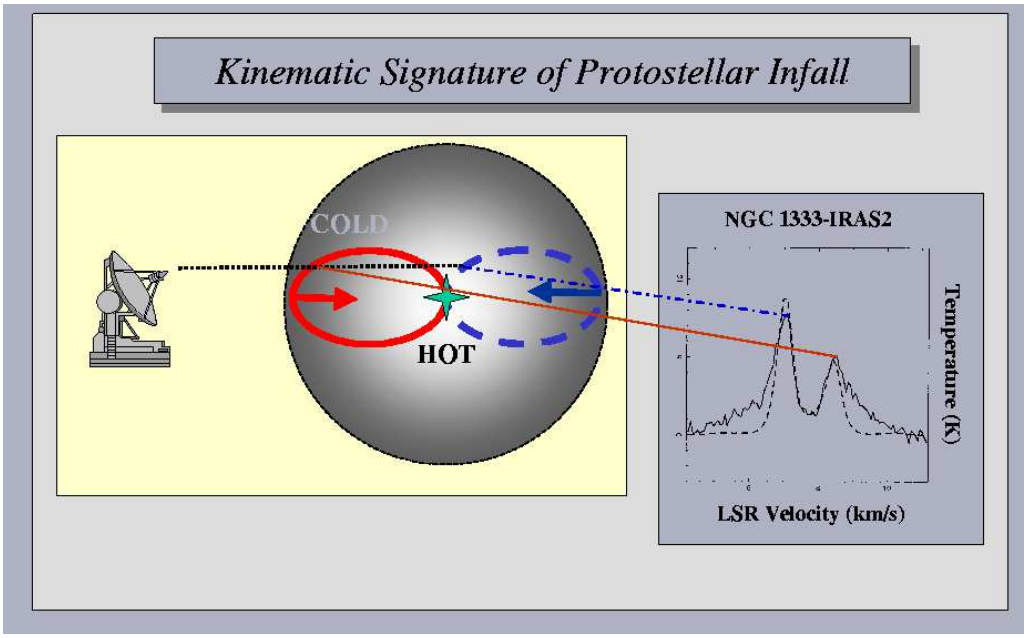

Figure 1.11: Explanation of blue-red asymmetry when we observe a spherical symmetric inflow motion. An isovelocity curve for the red-shifted gas is plotted in a solid line. That for the blue-shifted gas is plotted in a dashed line. Taken from Fig.14 of Lada (1999).

line profiles of CS $J = 2 - 1$ line emissions are shown (Zhou et al. 1993). The relative position of the profiles correspond to the position of the beam. (9,9) represents the offset of (9",9") from the center. At the center (0,0), the spectrum shows two peaks and the blue-shifted peak is brighter than the red-shifted one. This is believed to be a sign of gas infall motion. The blue-red asymmetry is explained as follows:

1. Considering a spherical symmetric inflow of gas, whose inflow velocity v_r increases with reaching the center (a decreasing function of r)

2. Considering a gas element at $\mathbf{r}$ moving at a speed of $v_r(\mathbf{r}) < 0$, the velocity projected on a line-of-sight is equal to

$$v_{\rm line-of-sight} = v_{\rm systemic} + v_r \cos\theta, \tag{1.5}$$

   where $v_{\rm systemic}$ represents the systemic velocity of the cloud (line-of-sight velocity of the cloud center) and θ is the angle between the line-of-sight and the position vector of the gas element. The isovector lines, the line which connect the positions whose procession/recession velocities are the same, become like an ellipse shown in Fig.1.11.

3. An isovelocity curve for the red-shifted gas is plotted in a solid line. That for the blue-shifted gas is plotted in a dashed line. If the gas is optically thin, the blue-shifted and red-shifted gases contribute equally to the observed spectrum and the blue- and red-shifted peaks of the emission line should be the same.

4. In the case that the gas has a finite optical depth, for the red-shifted emission line a cold gas in the fore side absorbs effectively the emission coming from the hot interior. On the other hand, for the blue-shifted emission line, the emission made by the hot interior gas escapes from the cloud without absorbed by the cold gas (there is no cold blue-shifted gas).

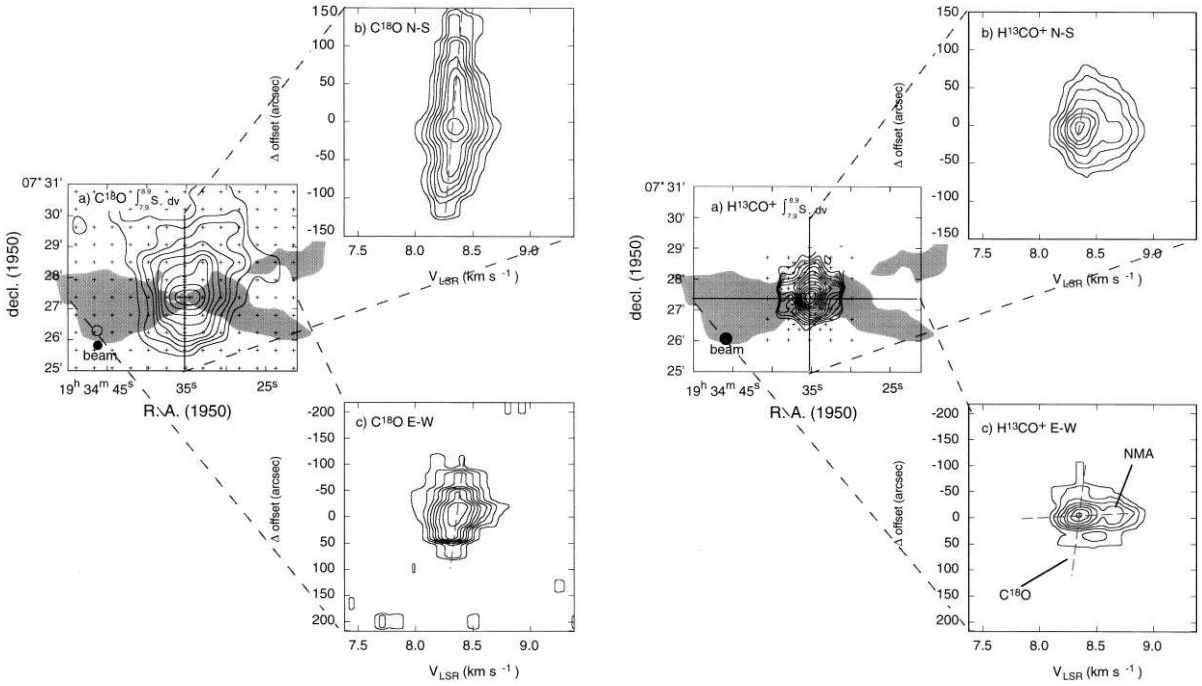

Figure 1.12: $C^{18}O$ total column density map (left) and $H^{13}CO^+$ channel map (right) of B335 along with the position-velocity maps along the major and minor axes. Taken from Fig.3 of Saito et al (1999).

5. As a result, the blue peak of the emission line becomes more prominent than that of the read-shifted emission. This is the explanation of the blue-red asymmetry.

In Figure 1.10, model spectra calculated with the Sobolev approximation (Zhou 1995) are shown. These show the blue-red asymmetry (the blue line > the red line).

Early observation of star forming regions have revieled fast molecular outflow are often ejected from the central protostar with $\gtrsim$10km s^{-1}. B335 is also a typical outflow source. In Figure 1.12, distributions of high density gases traced by the $C^{18}O$ and $H^{13}CO^+$ lines are shown as well as the bipolar outflow whose outline is indicated by a shadow (Hirano et al 1988). Comparing left and right panels, it is shown that the distribution of $C^{18}O$ gas is more extended than that of $H^{13}CO^+$ which traces higher-density gas. And the distribution of the $H^{13}CO^+$ is more compact and the projected surface density seems to show the the actual distribution is spherical. And the molecular outflow seems to be ejected in the direction of the minor axis of the high-density gas. It may suggest that (1) a molecular outflow is focused or collimated by the effect of density distribution or that (2) collimation is made by the magnetic fields which run preferentially perpendicularly to the gas disk. This gas disk is observed by these high density tracers.

Combining the $C^{18}O$ and $H^{13}CO^+$ distributions, the surface density distribution along the major axis is obtained by Saito et al (1999). From the lower panel of Figure 1.13, the column density distribution is well fitted in the range from 7,000 to 42,000 AU in radius,

$$\Sigma(r) = 6.3 \times 10^{21} \mathrm{cm}^{-2} \left(\frac{r}{10^4 \mathrm{AU}} \right)^{-0.95}, \tag{1.6}$$

where they omitted the data of $r \lesssim 7000$ since the beam size is not negligible. Similar power-law density distributions are found by the far IR thermal dust emission.

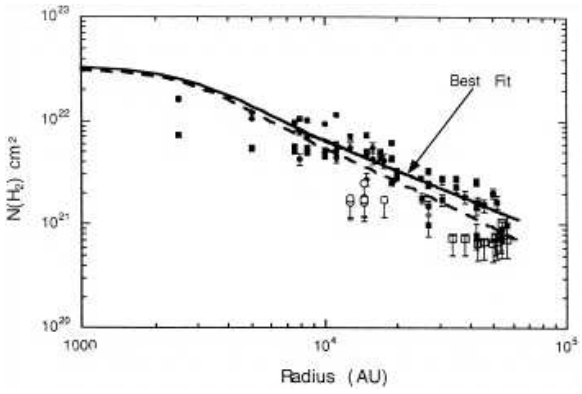

Figure 1.13: Column density distribution $N_{\rm H}(r)$ derived from the $H^{13}CO^+$ and $C^{18}O$ data taken by the Nobeyama 45 m telescope. Taken from Fig.9 of Saito et al (1999).

1.5.2 L1551 IRS 5

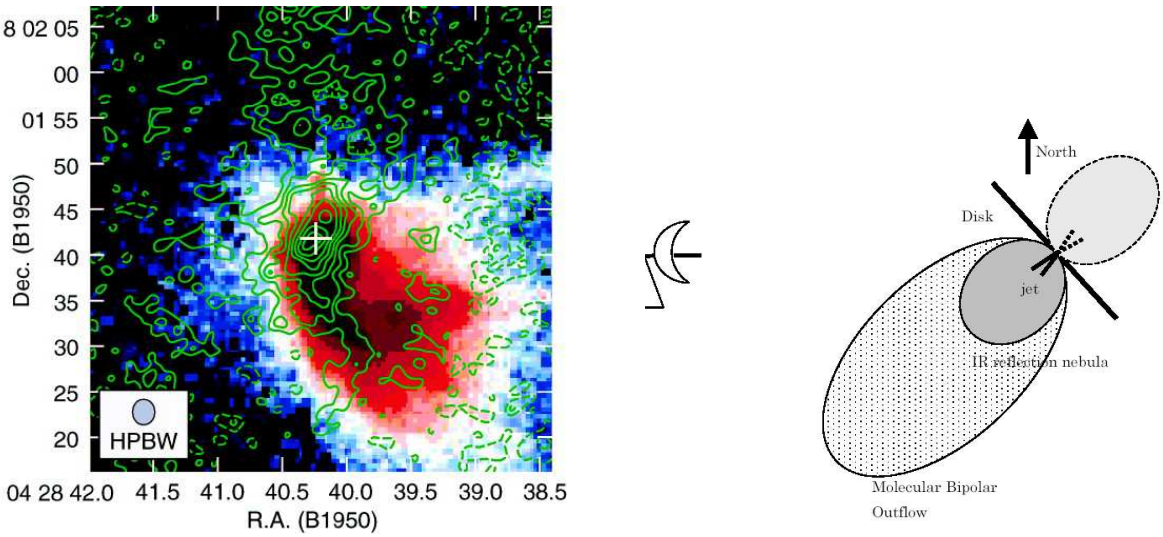

Figure 1.14: (*Left*:) ^{13}CO column density distribution. The contour lines represent the distribution of ^{13}CO column density. 2.2 μm infra-red reflection nebula is shown in grey scale which was observed by Hoddap (1994). (*Right*:) Schematic view of L1551 IRS5 region.

L1551 IRS 5 is one of the most well studied protostellar objects. This has an infra-red emission nebulosity (Fig.1.14). It is believed that there is a hole perpendicular to the high-density disk and the emission from the central star escapes through the hole and irradiate the nebulosity. In this sense this is a reflection nebula. L1551 IRS 5 has an elongated structure of dense gas similar to that observed in B335. The gas is extending in the direction from north-west to south-east [Fig.1.14 (left)]. Since the opposite side of the nebulosity is not observed, the opposite side of nebulosity seems to be located beyond the high-density disk and be obscured by the disk. This is possible if we see the south surface of the high-density disk as in Figure 1.14 (right).

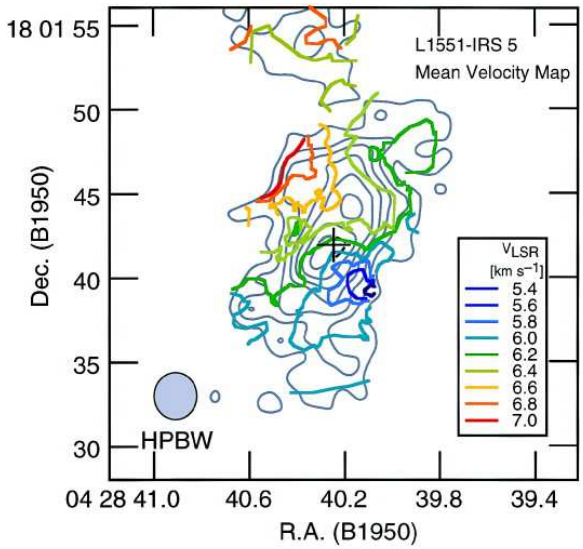

Figure 1.15: Isovelocity contours measured by the ^{13}CO $J = 1 - 0$ line. It should be noticed that the isovelocity lines run parallelly to the major axis. The north-eastern side shows a red-shift and the south-western side shows a blue-shift.

Infall Motion

The inflow motion is measured. Figure 1.15 shows the isovelocity contours measured by the ^{13}CO $J = 1-0$ observation (Ohashi et al 1996). It should be noticed that the isovelocity lines run parallelly to the major axis. The north-eastern side shows a red-shift and the south-western side shows a blue-shift. Considering the configuration of the gas disk shown in Fig.1.14 (right), this pattern of isovelocity contours indicates not outflow but inflow. That is, the north-east side is a near side of the disk and the south-west side is a far side. Since a red-shifted motion is observed in the near side and a blue-shifted motion is observed in the far side, it should be concluded that the gas disk of the L1551 IRS5 is now infalling.

Optical Jet

HST found two optical jets emanating from L1551 IRS5. This has been observed by SUBARU telescope, which found jet emission is dominated by [FeII] lines in the J- and H-bands. The jet extents to the south-western direction and disappears at $\sim$ 10" $\simeq$ 1400AU from the IRS5. The width-to-length ratio is very small $\lesssim 1/10$ or less, while the bipolar molecular outflow shows a less collimated flow. As for the origin of the two jets, these two jets might be ejected from a single source. However, since there are at least two radio continuum sources in IRS5 within the mutual separation of $\sim$ 0."5 [see Fig.1.16 (right)], these jets seem to be ejected from the two sources independently.

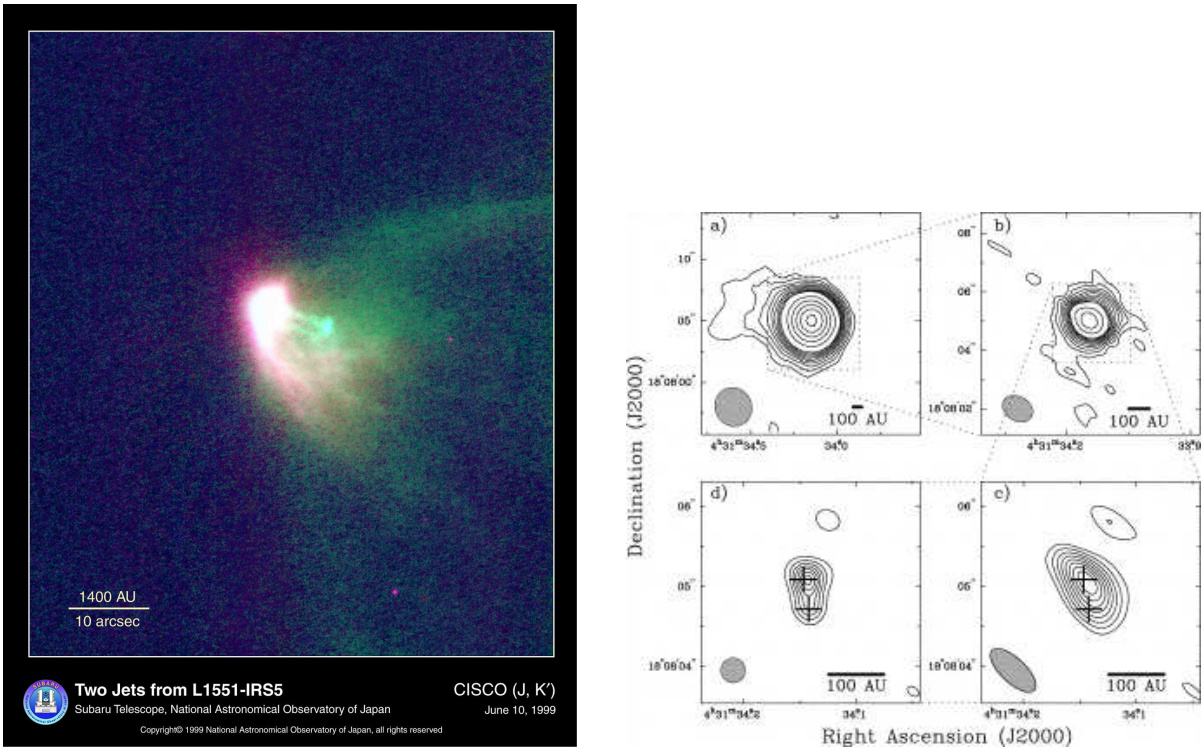

Figure 1.16: (*Left*:) Infrared image (J- and K-band) of the IR reflection nebula around L1551 IRS5 by SUBARU telescope. Taken from Fig.1 of Itoh et al. (2000). (A jpeg file is available from the following url: `http://SubaruTelescope.org/Science/press_release/9908/L1551.jpg`). (*Right*:) Central 100 AU region map of L1551 IRS5. This is taken by the $\lambda = 2.7$cm radio continuum observation. Deconvolved map (lower-left) shows clearly that IRS5 consists of two sources. Taken from Looney et al. (1997).

Although the lengths of these jets are restricted to 10", Herbig-Haro jets, which are much larger than the jets in L1551 IRS5, have been found. HH30 has a $\sim$ 500 AU-scale jet whose emission is mainly from the shock-excited emission lines. One of the largest ones is HH111, which is a member of the Orion star forming region and whose distance is as large as $D \sim 400$pc, and a jet with a length of $\sim$ 4pc is observed. Source of HH111 system is thought to consist of at least binary stars or possibly triple stars [Reipurth et al (1999)]. Star A, which coincides with a $\lambda = 3.6$ cm radio continuum source (VLA 1), shows an elongation in the VLA map whose direction is parallel to the axis of the jet. Therefore, star A is considered to be a source of the jet. Since the VLA map of star A shows another elongated structure perpendicular to the jet axis, star A may be a binary composed by two outflow sources.

1.6 L 1544: Pre-protostellar Cores

L1544 is known as a pre-protostellar core (Taffala et al 1998). That shows an infall motion but this contains no IR protostars. In Figure 1.18(*left*), CCS total column density map is shown, which shows an elongated structure. Ohashi et al (1999) have found both rotation and infall motion in the cloud. Position-velocity (PV) diagram along the minor axis shows the infall motion. That along the major axis indicates a rotational motion, which is shown by a velocity gradient. Due to a finite size of the beam, a contraction motion is also shown in the PV diagram along the major axis.

1.7 Magnetic Fields

Directions of magnetic field are studied by (1) measuring the polarization of light which is suffered from interstellar absorption. In this case the direction of magnetic field is parallel to the polarization vector. The reason is explained in Figure 1.19. In the magnetic fields, the dusts are aligned in a way that their major axes are perpendicular to the magnetic field lines. Such aligned dusts absorb selectively the radiation whose E-vector is parallel to their major axes. As a result, the detected light has a polarization parallel to the magnetic field lines.

However, the polarization measurement in the near IR wavelength limited to the region with low gas density, because background stars suffer severe absorption and becomes hard to be observed if we want to measure the polarization of the high-density region. More direct method is (2) the measurement of the linear polarization of the thermal emission from dusts in the mm (or sub-mm) wavelengths; in this case the direction of magnetic field is perpendicular to the polarization vector. The mechanism is explained in Figure 1.19b. The aligned dusts, whose major axes are perpendicular to the magnetic field lines, emit the radiation whose E-vector is parallel to the major axes. Since the absorption does not have a severe effect in this mm wavelengths, this gives information the magnetic fields deep inside the clouds.

1.7.1 Prestellar Core

Figure 1.20 illustrates the polarization maps of three prestellar cores (L1544, L183, and L43) done in the 850 μm band by JCMT-SCUBA. In L1544 and L183 the mean magnetic fields are at an angle of 30 deg to the minor axes of the cores. L43 is not a simple object; there is a T Tauri star located in the second core which extends to south-western side of the core (an edge of this core is seen near the western SCUBA frame boundary). And a molecular outflow from the source seems to affect the core. The magnetic field as well as the gas are swept by the molecular outflow. L43 seems an exception. The fact that the mean magnetic fields are parallel to the minor axis of the high-density

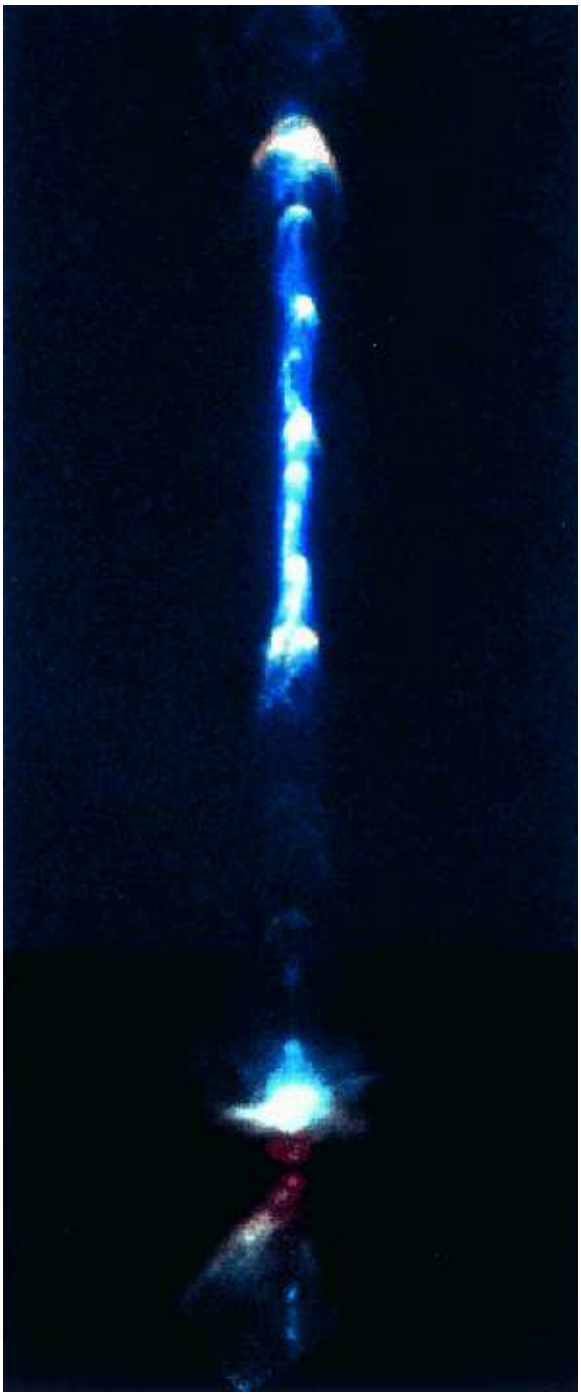

Figure 1.17: A mosaic image of HH 111 based on HST NICMOS images (bottom) and WFPC2 images (top). Taken from Fig.1 of Reipurth et al (1999).

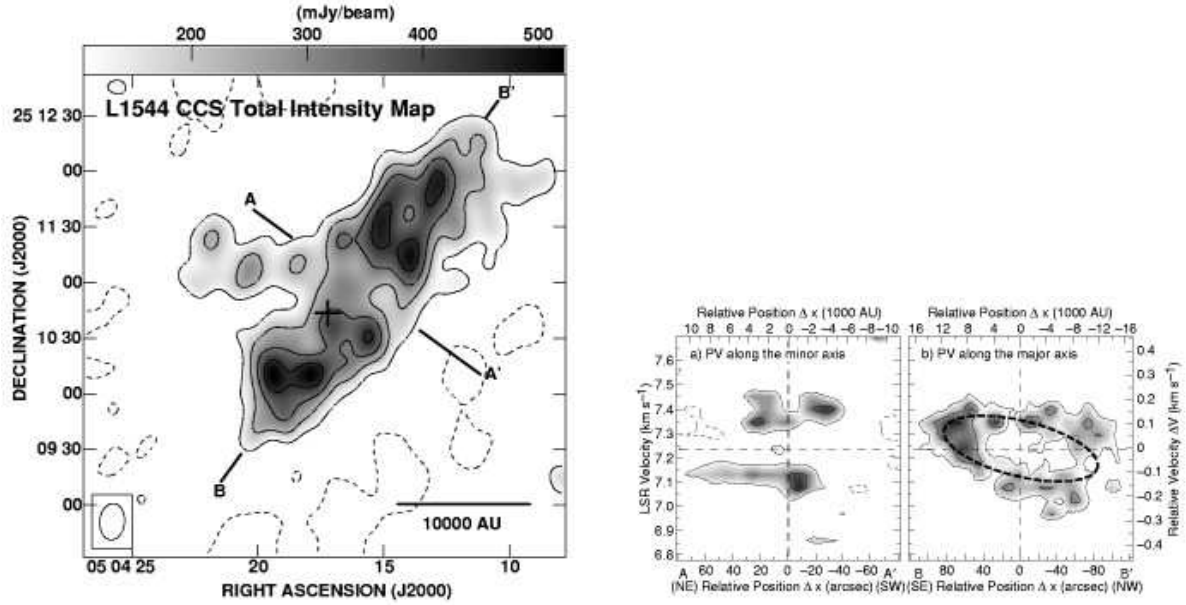

Figure 1.18: CCS image of prestellar core L1544. (*Left*:) Total intensity map. (*Right*:) PV diagrams along the minor axis (left) and along the major axis (right).

gas distribution seems to mean gas contracts preferentially in the direction parallel to the magnetic fields.

1.7.2 Cores with Protostars

Bok Globules

Bok globules are isolated dark clouds. Wolf, Launhardt & Henning (2003) have studied the relation between the magnetic field and outflow directions. Figure 1.21 displays the direction of the magnetic field obtained with JCMT-SCUBA polarization observation in 850μm as well as the outflow found by 13CO observation of Chandler & Sargent (1993) and ^{12}CO observation by Yun & Clemens (1994). In B 335, CB 230 and CB 244 outflows are oriented in the direction perpendicular to the major axis of the globules. The magnetic field is running parallel to the outflow but perpendicular to the major axis. This means that a disk is formed with a gas flowing along the magnetic field. Further, the outflow is generated by a twisted magnetic field which is an outcome of a rotating disk. In globule CB 54, the alignment is not perfect, that is, magnetic field direction is slightly aligned with the outflow (Wolf, Launhardt & Henning 2003). This seems to stengthen the magnetic origin of the outflow and magnetically guided disk formation.

It is clearly shown that the polarization anti-correlates with the intensity of the thermal emission. This might be due to the observational error in the low intensity region (or low S/N region). This may be related to physical processes such as (1) the alingnment owing to the magnetic field becomes inefficient in high density region or (2) the magnetic field is tangled in the dense region and the polarization due to the aligned dust is canceled.

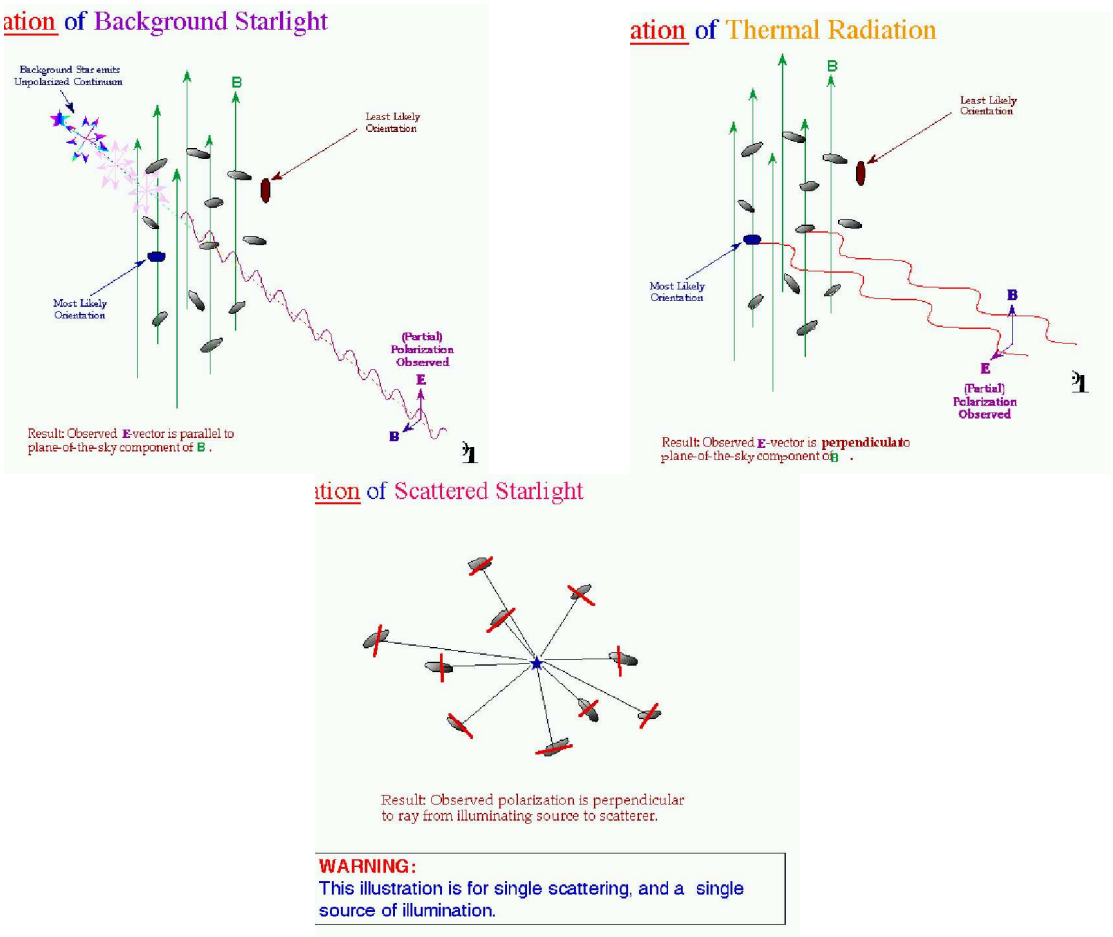

Figure 1.19: Explanation how the polarized radiation forms. Taken from Weintraub et al.(2000).

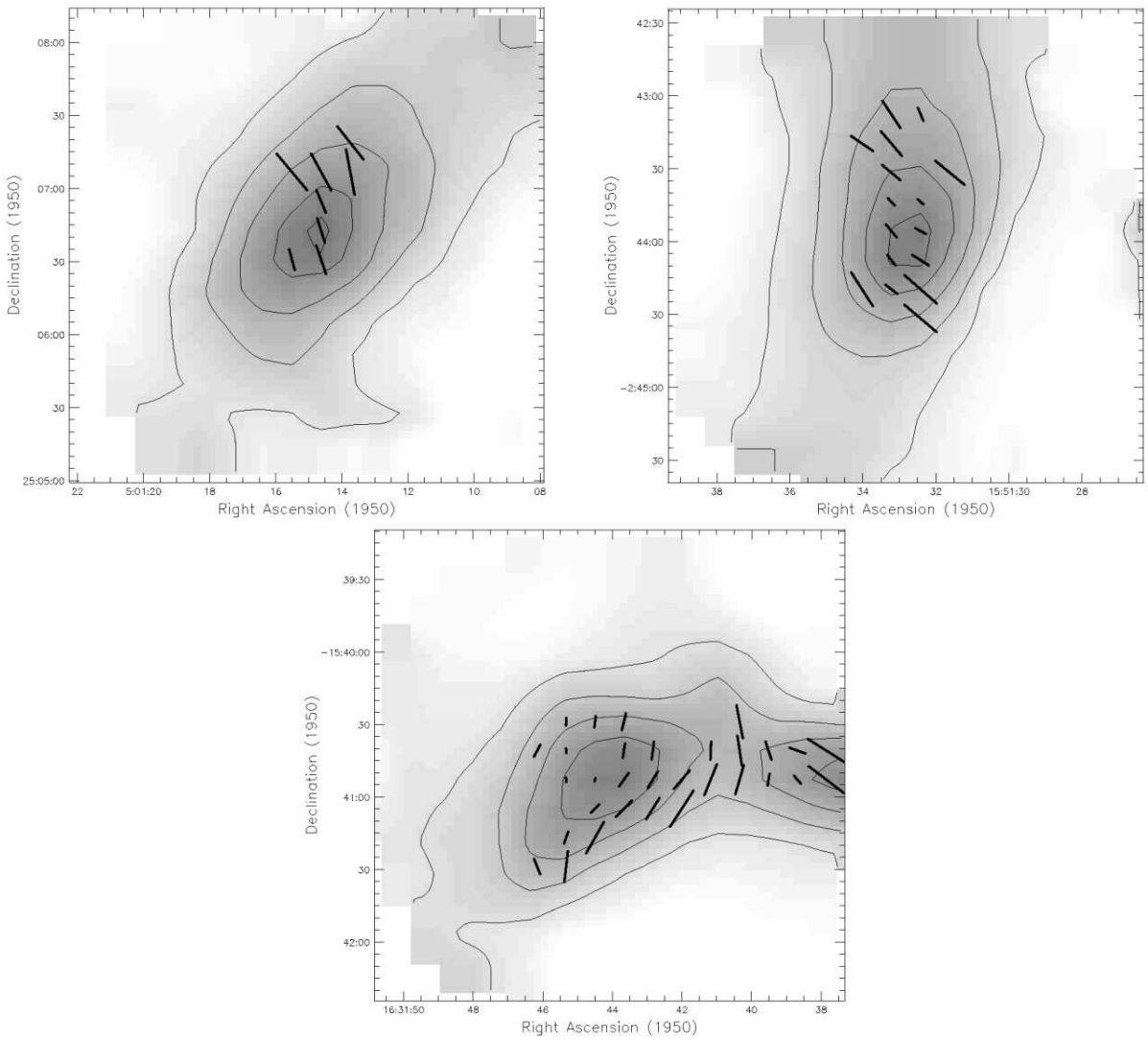

Figure 1.20: Directions of B-Field are shown from the linear polarization observation of 850 μm thermal emission from dusts by JCMT-SCUBA. L 1544 and L183, the magnetic field and the minor axis of the molecular gas distribution coincide with each other within $\sim$ 30deg. Taken from Ward-Thompson et al (2000).

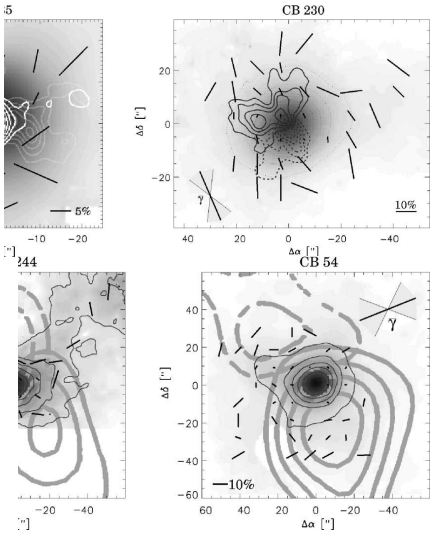

Figure 1.21: Directions of magnetic field are shown from the linear polarization observation of 850 μm thermal emission from dusts by JCMT-SCUBA. These four objects are known as Bok globules.

T Tauri Disks

Magnetic field at the position of protostars and T Tauri stars are measured for IRAS 16293-2422, L1551 IRS5, NGC1333 IRAS 4A, and HL Tau (Tamura et al. 1995). Although HL Tau is a T Tauri star, it has a gas disk. Thus this is a Class I source. The others are believed to be in protostellar phase (Class 0 sources). It is known that IRAS 16293-2422, L1551 IRS5, and HL Tau have disks with the radii of 1500-4000 AU from radio observations of molecular lines. Further, near infrared observations have shown that these objects have 300-1000 AU dust disks. Figure 1.22 shows the E-vector of polarized light. If this is the dust thermal radiation, the direction of magnetic fields is perpendicular to the polarization E-vector. Figure shows the magnetic fields run almost perpendicular to the elongation of the gas disk. Global directions of magnetic field outside the gas disk and the direction of CO outflows are also shown in the figure by arrows. It is noteworthy that the directions of local magnetic fields, global magnetic fields, and outflows coincide with each other within $\sim$ 30 deg.

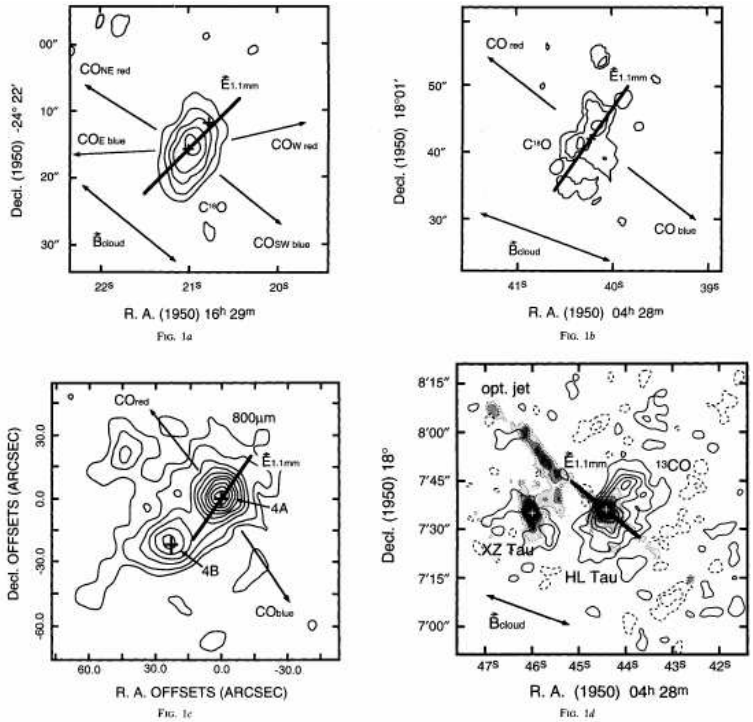

FIG. 1.—(*a*) IRAS 16293−2422; Geometrical relationship among the electric vector of the 1.1 mm continuum polarization (19″ beam), the embedding cloud magnetic field from optical or near-infrared polarimetry, the envelope/disk structure of gas or dust, and the directions of blue/red lobes of high-velocity CO outflows (this work; Vrba et al. 1976; Tamura 1988; Mundy et al. 1990; Mizuno et al. 1990). Note that the direction of the envelope/disk magnetic field inferred from the 1 mm polarization is perpendicular to the electric vector. (*b*) Same as (*a*) except for L1551 IRS 5 (this work; Vrba et al. 1976; Sargent et al. 1988; Snell et al. 1980). (*c*) Same as (*a*) except for NGC 1333 IRAS 4A (this work; Sandell et al. 1991; Sandell & Aspin 1933). (*d*) Same as (*a*) except for HL Tau. The optical jet is also shown (this work; Hayashi et al. 1993; Vrba et al. 1976; Mundt, Ray, & Bührke 1988).

Figure 1.22: Polarization of the radio continuum $\lambda = 1$mm, $\lambda = 0.8$mm. IRAS 16293-2422 (*upper-left*), L1551 IRS5 (*upper-right*), NGC1333 IRAS 4A (*lower-left*), and HL Tau (*lower-right*). Taken from Tamura et al (1995).

1.8 Density Distribution

Motte & André (2001) made λ =1.3 mm continuum mapping survey of the embedded young stellar objects (YSOs) in the Taurus molecular cloud. Their maps include several isolated Bok globules, as well as protostellar objects in the Perseus cluster. For the protostellar envelopes mapped in Taurus, the results are roughly consistent with the predictions of the self-similar inside-out collapse model of Shu and collaborators (section 4.5.1). The envelopes observed in Bok globules are also qualitatively consistent with these predictions, providing the effects of magnetic pressure are included in the model. By contrast, the envelopes of Class 0 protostars in Perseus have finite radii $\lesssim$10000 AU and are a factor of 3 to 12 denser than is predicted by the standard model.

Another method to measure the density distribution is to use the near IR extinction. From $(H-K)$ colors of background stars, the local value of A_V in a dark cloud can be obtained using a standard reddening law,

$$A_V = 15.87E(H-K) \tag{1.7}$$

if the intrinsic colors of background stars are known. Here, the color excess is defined as the difference between the observed color and the intrinsic color: $E(H-K) \equiv (H-K)_{\rm obs} - (H-K)_{\rm intrinsic}$. We can convert the extinction to the column density assuming the gas/dust ratio is constant

$$N({\rm H}+{\rm H_2}) = 2\times 10^{21}{\rm cm^{-2}mag^{-1}}A_V. \tag{1.8}$$

This is a standard method to obtain the local column density of the dark cloud using the near IR photometry.

See Figure 1.23. If the density distribution is expressed as

$$\rho(r) = \rho_0 \left(\frac{r}{r_0}\right)^{-\alpha}, \tag{1.9}$$

where r is a physical distance from the center. The column density distribution against the projected distance of the line-of-sight from the center of the cloud is given as

$$N_\rho(p) = 2\int_0^{(R^2-p^2)^{1/2}} \rho\left[(s^2+p^2)^{1/2}\right] ds, \tag{1.10}$$

where R represents the outer radius of the cloud. Using equation (1.8), this yields A_V distribution

$$A_V(p) = 10^{-23}\rho_0 r_0^\alpha \int_0^{(R^2-p^2)^{1/2}} (s^2+p^2)^{-\alpha/2} ds. \tag{1.11}$$

If background stars are uniformly distributed, the number of stars with $A_V|_{\rm obs}$ is proportional to the area which satisfies $A_V|_{\rm obs} = A_V(p)$. That is, if we plot $A_V(p)$ against $2\pi p dp$, this gives the number distribution of background stars with A_V. Figure 1.25 shows the result of L977 dark cloud by Alves et al (1998).

Recently, Alves et al (2001) derived directly the radial distribution of N_H by comparing the $N_H(p)$ model distribution for B68. They obtained a distribution is well fitted by the Bonner-Ebert sphere in which a hydrostatic balance between the self-gravity and the pressure force is achieved (lower panels of Fig.1.25) (see section 4.1.1).

In this fields, we should pay attention to the density distribution in cylindrical clouds. As seen in the Taurus molecular cloud, there are may filamentary structures in a molecular cloud. In §4.1, we will give the distribution for a hydrostatic spherically symmetric and that of a cylindrical cloud. The former is proportional to $\rho \propto r^{-2}$ and the latter is $\rho \propto r^{-4}$. Therefore, the distribution $\rho \propto r^{-4}$

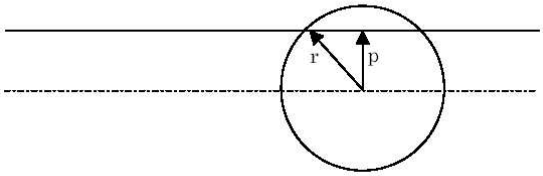

Figure 1.23: Schematic view to explain an A_V distribution.

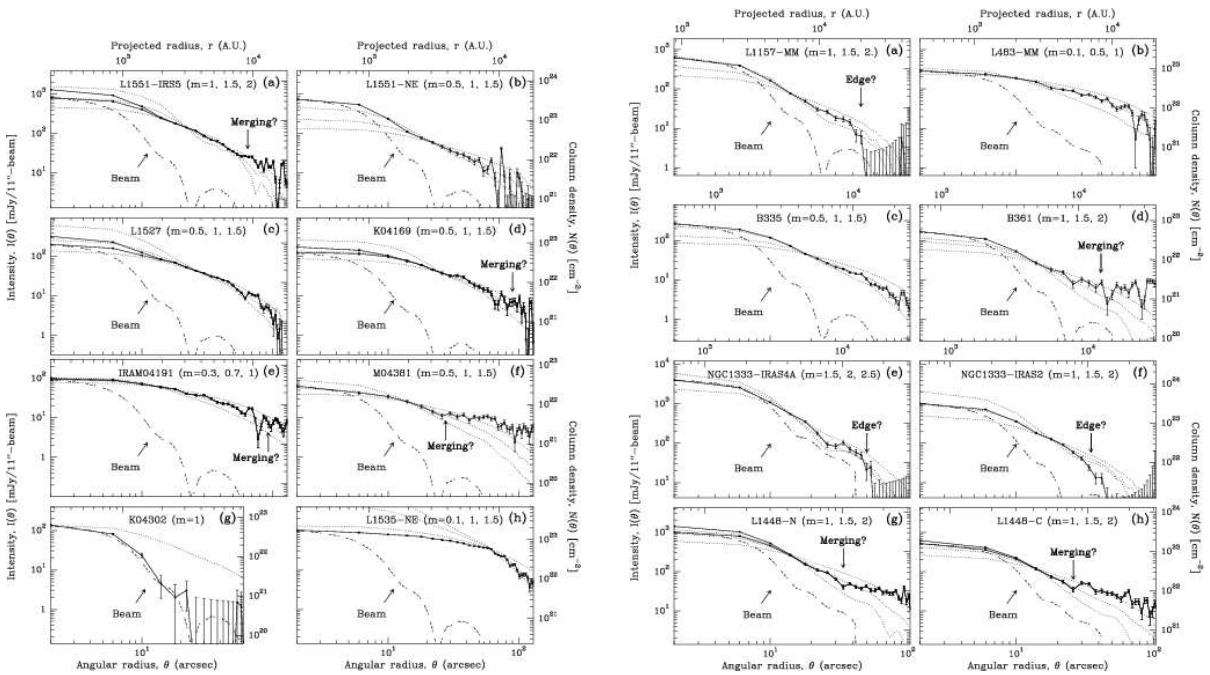

Figure 1.24: (*Left*:) Radial intensity profiles of the environment of 7 embedded YSOs (a-g) and 1 starless core (h). (*Right*:) Same as left panel but for 4 isolated globules (a-d) and 4 Perseus protostars (e-h). Taken from Motte & Andre (2001).

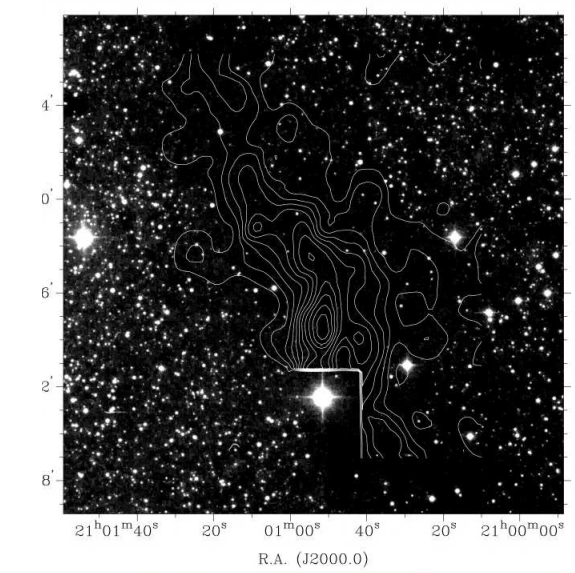

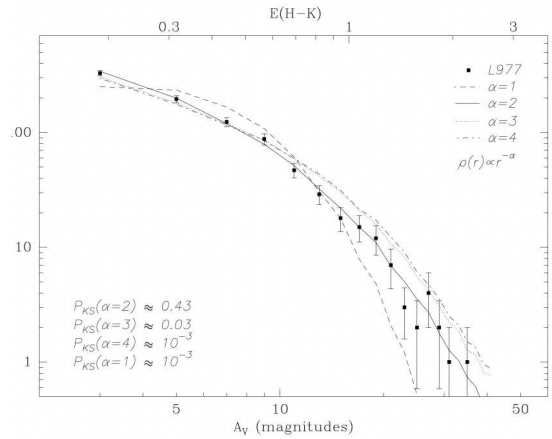

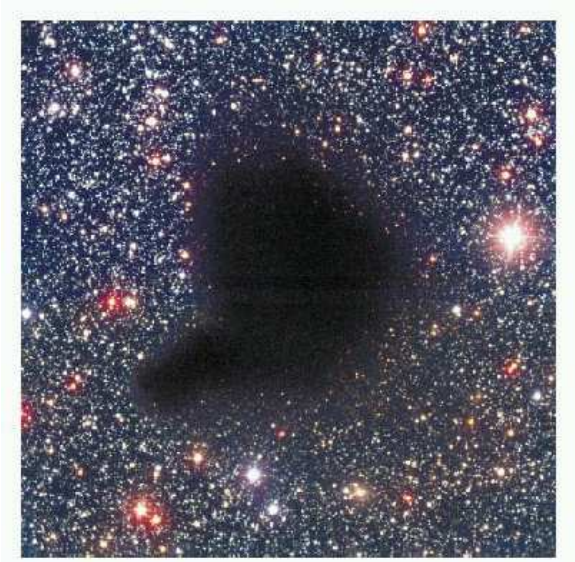

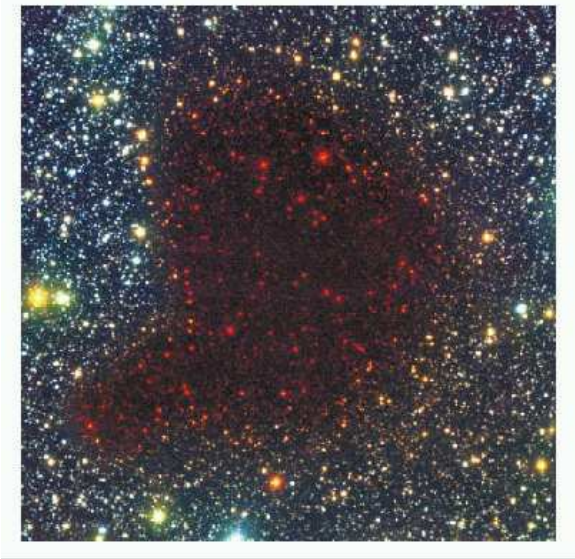

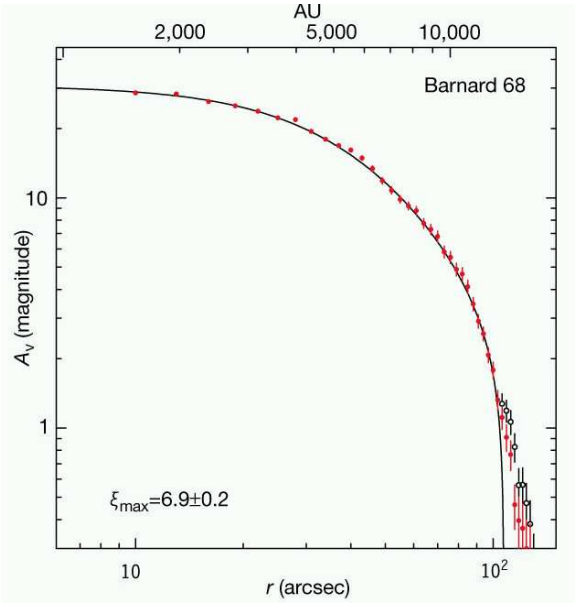

Figure 1.25: Density distribution of L977 (top) and B68 (bottom) dark clouds. (Top-left:) L977 dark cloud dust extinction map derived from the infrared (H-K) observations. (Top-right:) Observed frequency distribution of extinction measurements for L977 and the predictions from clouds models with density structures $\rho(r) \propto r^{-\alpha}$ having $\alpha = 1$ (dashed line), 2 (solid line), 3 (dotted line), and 4 (dash-dotted line). (Bottom-left:) B68 images (false color images made from B, V, and I images (top), and B, I, and K images (bottom)). (Bottom-right:) Spatial distribution of the column density,

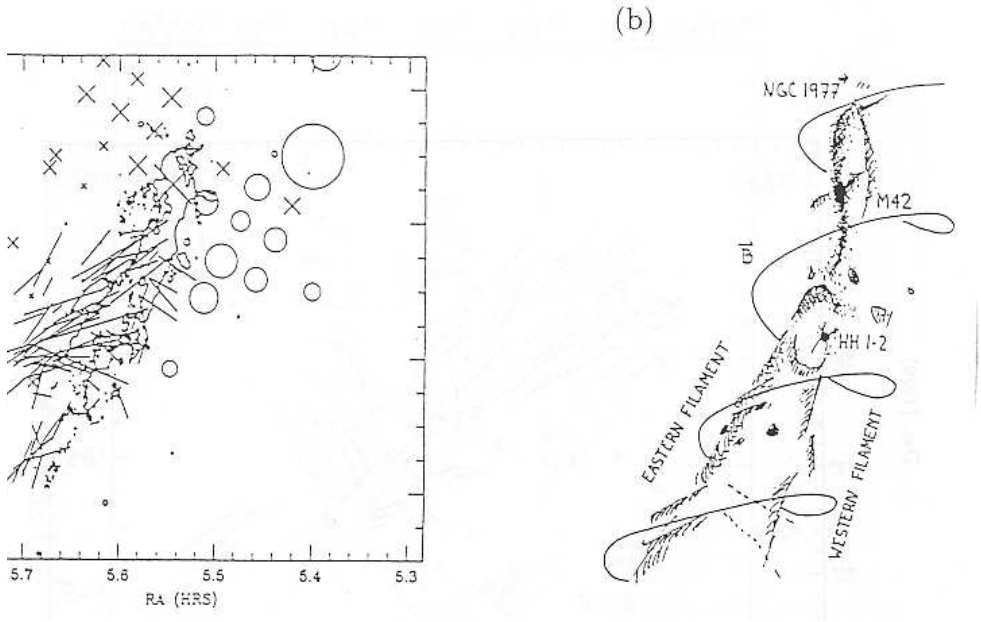

Figure 1.26: A structure of magnetic fields in the L1641 region. Polarization of light from embedded stars (Vrba et al. 1988) is shown by a bar. The direction of magnetic fields in the line-of-sight is observed using the HI Zeeman splitting, which is shown by a circle and cross (Heiles 1989).

was expected for cylindrical cloud. From near IR extinctions observation (Alves et al 1998), even if a cloud is rather elongated [Fig.1.25 (top-left)], the power of the density distribution is equal to not -4 but $\simeq -2$. Fiege, & Pudritz (2001) proposed an idea that a toroidal component of the magnetic field, B_ϕ, plays an important role in the hydrostatic balance of the cylindrical cloud (Fig.1.26).

1.9 Mass Spectrum

We have seen that a molecular cloud consists in many molecular cloud cores. For many years, there are attempts to determine the mass spectrum of the cores.

From a radio molecular line survey, a mass of each cloud core is determined. Plotting a histogram number of cores against the mass, we have found that a mass spectrum can be fitted by a power law as

$$\frac{dN}{dM} = M^n \tag{1.12}$$

where dN/dM represents the number of cores per unit mass interval. Many observation indicate that $n \sim -1.5$ as Table 1.1.

Figure 1.27 (Motte et al 2001) shows the cumulative mass spectrum ($N(> M)$ vs. M) of the 70 starless condensations identified in NGC 2068/2071. The mass spectrum for the 30 condensations of the NGC 2068 sub-region is very similar in shape. The best-fit power-law is $N(> M) \propto M^{n+1} \propto M^{-1.1}$ above $M \gtrsim 0.8 M_\odot$. That is, $n = -2.1$. This power derived from the dust thermal emission is different from that derived by the radio molecular emission lines. The power $n + 1 = -1.1$ which is close to the Salpeter's IMF for new born stars, $N(> M_*) \propto M_*^{-1.35}$ might be meaningful. The reason of the difference is not clear. For example, Tothill et al. (2002) observed the Lagoon nebula

Table 1.1: Mass spectrum indicies derived with molecular line surveys.

Paper	n	Region	Mass range
Loren (1989)	-1.1	ρ Oph	$10M_\odot \lesssim M \lesssim 300M_\odot$
Stutzki & Guesten (1990)	-1.7 ± 0.15	M17 SW	a few $M_\odot \lesssim M \lesssim$ a few $10^3 M_\odot$
Lada et al (1991)	-1.6	L1630	$M \gtrsim 20M_\odot$
Nozawa et al (1991)	-1.7	ρ Oph North	$3M_\odot \lesssim M \lesssim 160M_\odot$
Tatematsu et al. (1993)	-1.6 ± 0.3	Orion A	$M \gtrsim 50M_\odot$
Dobashi et al (1996)	-1.6	Cygnus	$M \gtrsim 100M_\odot$
Onish et al (1996)	-0.9 ± 0.2	Taurus	$3M_\odot \lesssim M \lesssim 80M_\odot$
Kramer et al.(1998)	$-1.6 \sim -1.8$	L1457 etc*	$10^{-4}M_\odot \lesssim M \lesssim 10^4 M_\odot$
Heithausen et al (2000)	-1.84	MCLD123.5+24.9,Polaris Flare	$M_J \lesssim M \lesssim 10M_\odot$
Onishi et al. (2002)	-2.5	Taurus $H^{13}CO^+$	$3.5M_\odot \lesssim M \lesssim 20.1M_\odot$

* MCLD126.6+24.5, NGC 1499 SW, Orion B South, S140, M17 SW, and NGC 7538

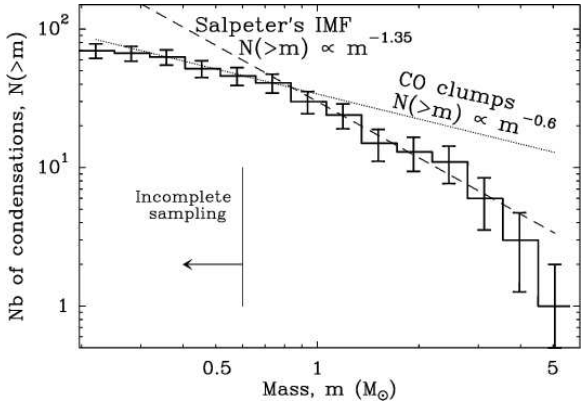

Figure 1.27: Cumulative mass distribution of the 70 pre-stellar condensations of NGC 2068/2071. The dotted and dashed lines are power-laws corresponding to the mass spectrum of CO clumps (Kramer et al. 1996) and to the IMF of Salpeter (1955), respectively. Taken from Fig.3 of Motte et al (2001).

around the edge of the HII region M8. From the continum emission $\lambda = 450\mu$m, 850μm, 1.3mm, they obtained index of -1.7 ± 0.6, which is consistent with other molecular line studies.

1.10 Line Width - Size Relation

Larson (1981) compiled the observations for molecular cloud complexes, molecular cloud and molecular clumps published in 1974-1979. He obtained an empirical relation that the size of a structure is well correlated to the random velocity in the structure which is measured by the width of the emission line (see Appendix E). Figure 1.28(left) shows this correlation and this is well expressed as

$$\sigma \simeq 1.10 \mathrm{km\,s^{-1}} \left(\frac{L}{1\mathrm{pc}}\right)^{0.38}, \tag{1.13}$$

where σ and L represent respectively the three-dimensional random speed of gas and the size of the structure. A similar correlation is found only for giant molecular clouds (Sanders, Scoville, & Solomon 1985) as

$$\sigma = \left(\frac{3}{2^3 \ln 2}\right)^{1/2} \Delta V_{\mathrm{FWHM}} = (0.535 \pm 0.16) \mathrm{km\,s^{-1}} \left(\frac{L}{1\mathrm{pc}}\right)^{0.62}, \tag{1.14}$$

for GMCs whose sizes are larger than 10pc (be careful the typos in their abstract: power was -0.62). He also found another correlation between the mass M and the random velocity like Figure 1.28(right), which is expressed as

$$\sigma \simeq 0.43 \mathrm{km\,s^{-1}} \left(\frac{M}{1M_\odot}\right)^{0.20}. \tag{1.15}$$

In the next chapter (§2.9), we will see the virial relation, that is, for an isolated system to achieve a mechanical equlibrium the gravitaional to thermal energy ratio has to be equal to 2:1 for $\gamma = 5/3$ gas. The ratio of the gravitational energy $\sim (3/5)GM^2/(L/2)$ to the thermal energy $M\sigma^2/2$ is also fitted as

$$\frac{12}{5}\frac{GM}{\sigma^2 L} \simeq 1.1 \left(\frac{L}{1\mathrm{pc}}\right)^{0.14}, \tag{1.16}$$

which is weakly dependent of the size or the mass. This seems to mean the ratio is nearly constant irrespective of the mass or size of the clouds.

Since there is a mutual relation between mass, size, and the velocity dispersion to achive a mechanical equlibrium (the Virial relation), there is only one independent correlation in the above two correlations (eqs.[1.13] and [1.15]). Although several reasons to explain the correlation are proposed, we have no consensus yet.

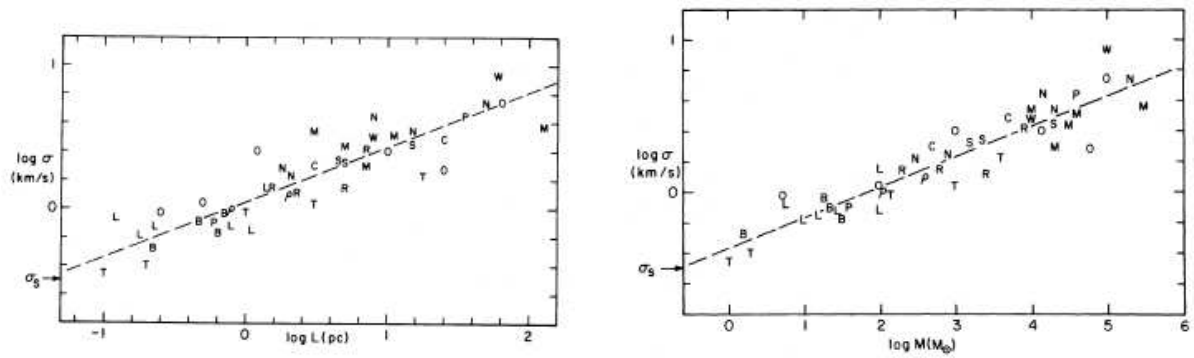

Figure 1.28: The left shows the relation between cloud size (holizontal axis) and the three-dimensional internal velocity (vertical axis). The right shows a similar correlation between mass and the random velocity.

Chapter 2

Physical Background

2.1 Basic Equations of Hydrodynamics

The basic equation of hydrodynamics are (1) the continuity equation of the density [equation (A.11)],

$$\frac{\partial \rho}{\partial t} + \mathrm{div}(\rho \mathbf{v}) = 0, \tag{2.1}$$

(2) the equation of motion [equation (A.7)]

$$\rho \left[\frac{\partial \mathbf{v}}{\partial t} + (\mathbf{v} \cdot \nabla)\, \mathbf{v} \right] = -\nabla p + \rho \mathbf{g}, \tag{2.2}$$

and (3) the equation of energy [equation (A.23)]

$$\frac{\partial \epsilon}{\partial t} + \mathrm{div}(\epsilon + p)\mathbf{v} = \rho \mathbf{v} \cdot \mathbf{g}. \tag{2.3}$$

Occasionally barotropic relation $p = P(\rho)$ substitutes the energy equation (2.3). Especially polytropic relation $p = K\rho^{\Gamma}$ is often used on behalf of the energy equation. In the case that the gas is isothermal or isentropic, the polytropic relations of

$$p = c_{is}^2 \rho \quad \text{(isothermal)} \tag{2.4}$$

and

$$p = c_s^2 \rho^{\gamma} \quad \text{(isentropic)} \tag{2.5}$$

are substitution to equation (2.3). [We can replace equation (2.3) with equations (2.4) and (2.5).]

2.2 The Poisson Equation of the Self-Gravity

In this section, we will show the basic equation describing how the gravity works. First, compare the gravity and the static electric force. Consider the electric field formed by a point charge Q at a distance r from the point source as

$$E = \frac{1}{4\pi\epsilon_0} \frac{Q}{r^2}, \tag{2.6}$$

where ϵ_0 is the electric permittivity of the vacuum. On the other hand, the gravitational acceleration by the point mass of M at the distance r from the point mass is written down as

$$g = -G \frac{M}{r^2}, \tag{2.7}$$

where $G = 6.67 \times 10^{-8}\mathrm{kg}^{-1}\,\mathrm{m}^3\,\mathrm{s}^{-2}$ is the gravitational constant. Comparing these two, replacing Q with M and at the same time $1/4\pi\epsilon_0$ to $-G$ these equations (2.6) and (2.7) are identical with each other.

The Gauss theorem for electrostatic field as

$$\mathrm{div}\,\mathbf{E} = \frac{\rho_e}{\epsilon_0}, \tag{2.8}$$

and another expression using the electrostatic potential ϕ_e as

$$\nabla^2\phi_e = -\frac{\rho_e}{\epsilon_0}, \tag{2.9}$$

lead to the equations for the gravity as

$$\mathrm{div}\,\mathbf{g} = -4\pi G\rho, \tag{2.10}$$

and

$$\nabla^2\phi = 4\pi G\rho, \tag{2.11}$$

where ρ_e and ρ represent the electric charge density and the mass density. Equation (2.11) is called the Poisson equation for the gravitational potential and describes how the potential ϕ is determined from the mass density distribution ρ.

Problem

Consider a spherically symmetric density distribution. Using the Poisson equation, obtain the potential (ϕ) and the gravitational acceleration (g) for a density distribution shown below.

$$\rho \begin{cases} = \rho_0 & \text{for } r < R \\ = 0 & \text{for } r \geq R \end{cases}$$

Hint: The Poisson equation (2.11) for the spherically symmetric system is

$$\frac{1}{r^2}\frac{\partial}{\partial r}\left(r^2\frac{\partial\phi}{\partial r}\right) = 4\pi G\rho.$$

2.3 Free-fall Time

If the pressure force can be neglected in the equation of motion (A.1), the gravitational force remains. Assuming the spherical symmetry, consider the gravity $g_r(r)$ at the position of radial distance from the center being equal to r. Using the Gauss' theorem, g_r is related to the mass inside of r, which is expressed by the equation

$$M_r = \int_0^r \rho 4\pi r^2 dr, \tag{2.12}$$

and g_r is written as

$$g_r(r) = -\frac{GM_r}{r^2}. \tag{2.13}$$

This leads to the equation motion for a cold gas under a control of the self-gravity is written

$$\frac{d^2r}{dt^2} = -\frac{GM_r}{r^2}. \tag{2.14}$$

Chapter 4

Local Star Formation Process

4.1 Hydrostatic Balance

Consider a hydrostatic balance of isothermal cloud. By the gas density, ρ, the isothermal sound speed, $c_{\rm is}$, and the gravitational potential, Φ, the force balance is written as

$$-\frac{c_{\rm is}^2}{\rho}\frac{d\rho}{dr} - \frac{d\Phi}{dr} = 0, \tag{4.1}$$

and the gravity is calculated from a density distribution as

$$-\frac{d\Phi}{dr} = -\frac{GM_r}{r^2} = -\frac{4\pi G}{r^2}\int_0^r \rho r^2 dr, \tag{4.2}$$

for a spherical symmetric cloud, where M_r represents the mass contained inside the radius r. The expression for a cylindrical cloud is

$$-\frac{d\Phi}{dr} = -\frac{G\lambda_r}{r} = -\frac{2\pi G}{r}\int_0^r \rho r dr, \tag{4.3}$$

where λ_r represents the mass per unit length within a cylinder of radius being r.

For the spherical symmetric case, the equation becomes the Lane-Emden equation with the polytropic index of ∞ (see Appendix C.1). This has no analytic solutions. However, the numerical integration gives us a solution shown in Figure 4.1 (left). Only in a limiting case with the infinite central density, the solution is expressed as

$$\rho(r) = \frac{c_{\rm is}^2}{2\pi G} r^{-2}. \tag{4.4}$$

Increasing the central density, the solution reaches the above Singular Isothermal Sphere (SIS) solution.

On the other hand, a cylindrical cloud has an analytic solution (Ostriker 1964) as

$$\rho(r) = \rho_c \left(1 + \frac{r^2}{8H^2}\right)^{-2}, \tag{4.5}$$

where

$$H^2 = c_{\rm is}^2/4\pi G\rho_c. \tag{4.6}$$

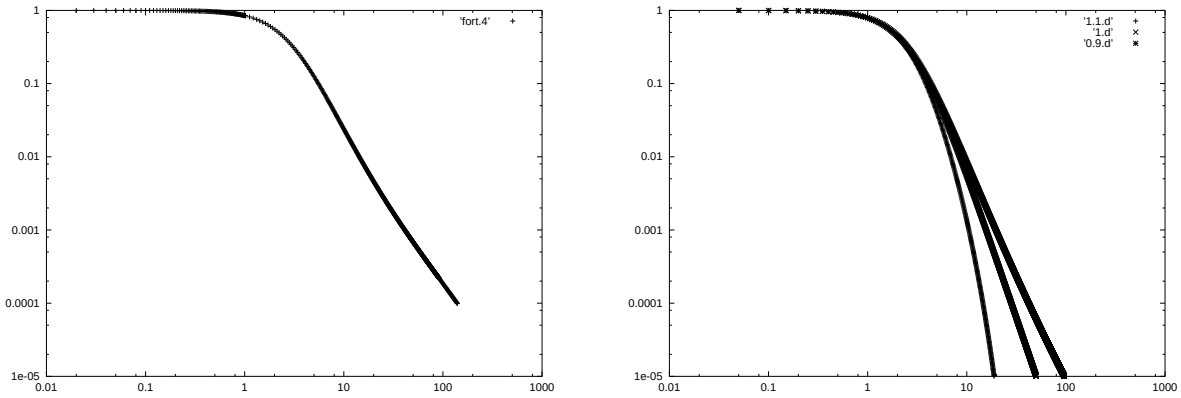

Figure 4.1: Radial density distribution. A spherical cloud (left) and a cylindrical cloud (right). In the right panel, solutions for polytropic gases with $\Gamma = 1.1$ (relatively compact) and $\Gamma = 0.9$ (relatively extended) are plotted as well as the isothermal one.

Far from the cloud symmetric axis, the distribution of equation (4.5) gives

$$\rho(r) \propto r^{-4}, \tag{4.7}$$

while the spherical symmetric cloud has

$$\rho(r) \propto r^{-2} \tag{4.8}$$

distribution.

Problem 1

Show that the SIS is a solution of equations (4.1) and (4.2).

Problem 2

Show that the density distribution of [equation (4.5)] is a solution of equations (4.1) and (4.3).

4.1.1 Bonnor-Ebert Mass

In the preceding section [Fig.4.1 (left)], we have seen the radial density distribution of a hydrostatic configuration of an isothermal gas. Consider a circumstance that such kind of cloud is immersed in a low-density medium with a pressure p_0. To establish a pressure equilibrium, the pressure at the surface $c_{\rm is}^2\rho(R)$ must equal to p_0. This means that the density at the surface is constant $\rho(R) = p_0/c_{\rm is}^2$.

Figure 4.2 (left) shows three models of density distribution, $\rho_c = \rho(r = 0) = 10\rho_s$, $10^2\rho_s$, and $10^3\rho_s$. Comparing these three models, it should be noticed that the cloud size (radius) decreases with increasing the central density ρ_c. The mass of the cloud is obtained by integrating the distribution, which is illustrated against the central-to-surface density ratio ρ_c/ρ_s in Figure 4.2 (right). The y-axis represents a normalized mass as $m = M/[4\pi\rho_s(c_{\rm is}/\sqrt{4\pi G\rho_s})^3]$. The maximum value of $m = 4.026$ means

$$M_{\rm max} \simeq 1.14\frac{c_{\rm is}^2}{G^{3/2}p_0^{1/2}}. \tag{4.9}$$

This is the maximum mass which is supported against the self-gravity by the thermal pressure with an isothermal sound speed of $c_{\rm is}$, when the cloud is immersed in the pressure p_0. This is called Bonnor-Ebert mass [Bonnor (1956), Ebert (1955)]. It is to be noticed that the critical state $M_{\rm cl} = M_{\rm max}$ is achieved when the density contrast is rather low $\rho_c \simeq 16\rho_s \equiv \rho_{\rm cr}$.

Another important result from Figure 4.2 (right) is the stability of an isothermal cloud. Even for a cloud with $M_{\rm cl} < M_{\rm max}$, any clouds on the part of $\partial M_{\rm cl}/\partial\rho_c < 0$ are unstable, whose clouds are distributed on the branch with $\rho_c > \rho_{\rm cr}$. This is understood as follows: For a hydrostatic cloud the mass should be expressed with the external pressure and the central density [Fig.4.2 (right)] as

$$M_{\rm cl} = M_{\rm cl}(p_{\rm ext}, \rho_c). \tag{4.10}$$

In this case, a relation between the partial derivatives such as

$$\left(\frac{\partial M_{\rm cl}}{\partial p_{\rm ext}}\right)_{\rho_c} \cdot \left(\frac{\partial p_{\rm ext}}{\partial \rho_c}\right)_{M_{\rm cl}} \cdot \left(\frac{\partial \rho_c}{\partial M_{\rm cl}}\right)_{p_{\rm ext}} = -1, \tag{4.11}$$

is satisfied, unless each term is equal to zero. Figure 4.1 (left) shows that the cloud mass $M_{\rm cl}$ is a decreasing function of the external pressure $p_{\rm ext} = \rho_s c_{\rm is}^2$, if the central density is fixed. Since this means

$$\left(\frac{\partial M_{\rm cl}}{\partial p_{\rm ext}}\right)_{\rho_c} < 0, \tag{4.12}$$

equation (4.11) gives us

$$\left(\frac{\partial p_{\rm ext}}{\partial \rho_c}\right)_{M_{\rm cl}} \cdot \left(\frac{\partial \rho_c}{\partial M_{\rm cl}}\right)_{p_{\rm ext}} > 0. \tag{4.13}$$

For a cloud with $\rho_c < \rho_{\rm cr} = 16 p_{\rm ext}/c_{\rm is}^2$ the mass is an increasing function of the central density as

$$\left(\frac{\partial M_{\rm cl}}{\partial \rho_c}\right)_{p_{\rm ext}} > 0. \tag{4.14}$$

Thus, equation (4.13) leads to the relation

$$\left(\frac{\partial \rho_c}{\partial p_{\rm ext}}\right)_{M_{\rm cl}} > 0, \tag{4.15}$$

for $\rho < \rho_{\rm cr}$. This means that gas cloud contracts (the central density and pressure increase), when the external pressure increases. This is an ordinary reaction of a stable gas.

On the other hand, the cloud on the part of $(\partial M_{\rm cl}/\partial\rho_c)_{p_{\rm ext}} < 0$ (for $16 \lesssim \rho_c/(p_{\rm ext}/c_{\rm is}^2) \lesssim 2000$) behaves

$$\left(\frac{\partial \rho_c}{\partial p_{\rm ext}}\right)_{M_{\rm cl}} < 0, \tag{4.16}$$

and this represents that an extra external pressure decreases the central density and thus the pressure. Pressure encourages expansion. This reaction is unstable.

4.1.2 Equilibria of Cylindrical Cloud

In Figure 4.1 (right) we plotted the structure for a polytropic cloud. Inner structure is not dependent of Γ, it is clear the slope of the outer envelope is dependent on Γ.

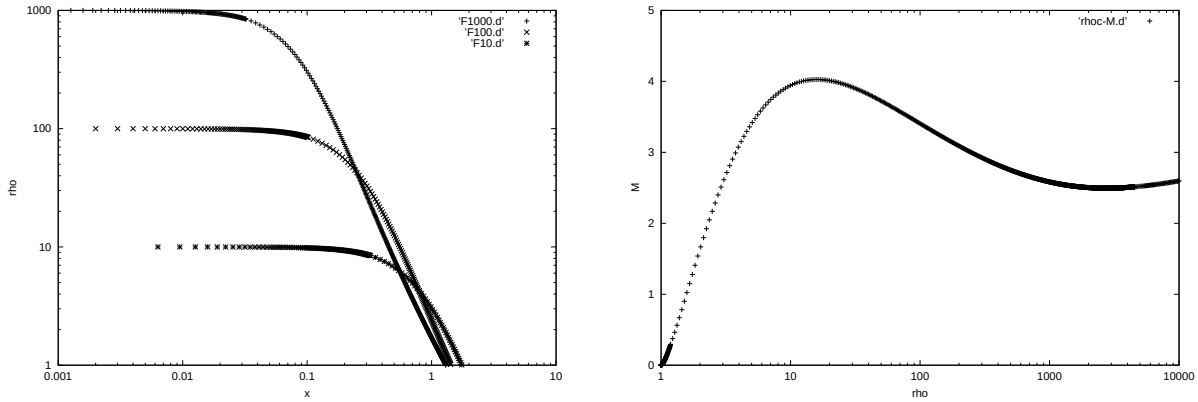

Figure 4.2: (Left) radial density distribution. Each curve has different ρ_c. The x-axis denotes the radial distance normalized by a scale-length as $c_{\rm is}^2/\sqrt{4\pi G p_{\rm ext}}$. It is shown that the radius increases with decreasing ρ_c in this range ($\rho_c = (10, 10^2, 10^3) \times p_{\rm ext}/c_{\rm is}^2$). (Right) The relation between mass ($M_{\rm cl}$) and the central density (ρ_c) is plotted, under the condition of constant external pressure. The x-axis represents the central density normalized by $\rho_s \equiv p_{\rm ext}/c_{\rm is}^2$. The y-axis represents the cloud mass normalized by $4\pi\rho_s(c_{\rm is}/\sqrt{4\pi G\rho_s})^3$.

1. In the case of the spherically symmetric, consider a polytrope ($p \propto \rho^\Gamma$) with $\Gamma < 6/5$ (at least the envelope of $\Gamma = 6/5$ cloud extends to ∞.), in which gas extends to ∞. if $\rho \propto r^{-p}$, the mass inside of r is proportional to $M_r \propto r^{3-p}$. Thus, the gravity per unit volume at a radius r, $GM\rho/r^2$, is proportional to $GM\rho/r^2 \propto r^{1-2p}$. On the other hand the pressure force is $|(\partial p/\partial r)| = (\partial p/\partial\rho)|(\partial\rho/\partial r)| \propto (r^{-p})^{\Gamma-1} r^{-p-1} \propto r^{-p\Gamma-1}$. These two powers become the same, only if $p = 2/(2-\Gamma)$.

2. In the case of cylindrical cloud with $\Gamma \leq 1$, the mass per unit length $\lambda \propto r^{2-p}$. The gravity at r, $G\lambda\rho/r \propto r^{1-2p}$. Note that the power is the same as the spherical case. Since the power of the pressure force should be the same as the spherical case, the resultant p should be the same $p = 2/(2-\Gamma)$.

The case of $\Gamma = 0.9$, an envelope extending to a large radius indicates the power-law distribution much shallower than that of the isothermal $\Gamma = 1$ one.

4.2 Virial Analysis

Hydrodynamic equation of motion using the Lagrangean time derivative [eq.(A.3)] is

$$\rho\left(\frac{d\boldsymbol{v}}{dt}\right) = -\boldsymbol{\nabla}p - \rho\boldsymbol{\nabla}\Phi. \tag{4.17}$$

Multiplying the position vector $\mathbf{r}$ and integrate over a volume of a cloud, we obtain the Virial relation as

$$\frac{1}{2}\frac{d^2I}{dt^2} = 2(T - T_0) + W, \tag{4.18}$$

where

$$I = \int \rho r^2 dV, \tag{4.19}$$

is an inertia of the cloud,

$$T = \int \left(\frac{3}{2} p_{\rm th} + \frac{1}{2} \rho v^2 \right) dV = \frac{3}{2} \bar{p} V_{\rm cl}, \tag{4.20}$$

is a term corresponding to the thermal pressure plus turbulent pressure,

$$T_0 = \int_S P_{\rm th} \mathbf{r} \cdot \mathbf{n} dS = \frac{3}{2} P_0 V_{\rm cl} \tag{4.21}$$

comes from a surface pressure, and

$$W = -\int \rho \mathbf{r} \cdot \nabla \Phi dV = -\frac{3}{5} \frac{GM^2}{R} \tag{4.22}$$

is a gravitational energy. To derive the last expression in each equation, we have assumed the cloud is spherical and uniform. Here we use a standard notation as the radius R, the volume $V_{\rm cl} = 4\pi R^3/3$, the average pressure $\bar{P}$, and the mass M.

To obtain a condition of mechanical equilibrium, we assume $d^2I/dt^2 = 0$. Equation (4.18) becomes

$$4\pi \bar{p} R^3 - 4\pi p_0 R^3 - \frac{3}{5} \frac{GM^2}{R} = 0. \tag{4.23}$$

Assuming the gas is isothermal $p = c_{\rm is}^2 \rho$, the average pressure is written as

$$\bar{p} = c_{\rm is}^2 \bar{\rho} = c_{\rm is}^2 \frac{3M}{4\pi R^3}. \tag{4.24}$$

Using equation (4.24) to eliminate $\bar{p}$ from equation (4.18), the external pressure is related to the mass and the radius as

$$p_0 = \frac{3 c_{\rm is}^2 M}{4\pi R^3} - \frac{3GM^2}{20\pi R^4}. \tag{4.25}$$

Keeping M constant and increasing R from zero, p_0 increases first, but it takes a maximum, $p_{0,\rm max} = 3.15 c_{\rm is}^8/(G^3 M^2)$, and finally declines. This indicates that the surface pressure must be smaller than $p_{0,\rm max}$ for the cloud to be in an equilibrium. In other words, keeping p_0 and changing R, it is shown that M has a maximum value to have a solution. The maximum mass is equal to

$$M_{\rm max} = 1.77 \frac{c_{\rm is}^4}{G^{3/2} p_0^{1/2}}. \tag{4.26}$$

The cloud massive than $M_{\rm max}$ cannot be supported against the self-gravity. This corresponds to the Bonnor-Ebert mass [eq.(4.9)], although the numerical factors are slightly different.

4.2.1 Magnatohydrostatic Clouds

Consider here the effect of the magnetic field. In the magnetized medium, the Lorentz force

$$\boldsymbol{F} = \frac{1}{4\pi} (\boldsymbol{\nabla} \times \boldsymbol{B}) \times \boldsymbol{B} = -\frac{1}{8\pi} \boldsymbol{\nabla} \boldsymbol{B^2} + \frac{1}{4\pi} (\boldsymbol{B} \cdot \boldsymbol{\nabla}) \boldsymbol{B} \tag{4.27}$$

works in the ionized medium. The first term of equation (4.27), which is called the **magnetic pressure**, has an effect to support the cloud against the self-gravity.

The virial analysis is also applicable to the magnetohydrostatic clouds. The terms related to the magnetic fields are

$$\begin{aligned} M &= \int \frac{B^2}{8\pi} dV + \int_S (\boldsymbol{r}\cdot\boldsymbol{B})\boldsymbol{B}\cdot\boldsymbol{n} dS - \int_S \frac{B^2}{8\pi}\boldsymbol{r}\cdot\boldsymbol{n} dS \\ &\simeq \int \frac{B^2 - B_0^2}{8\pi} dV \simeq \frac{1}{6\pi^2}\left(\frac{\Phi_B^2}{R} - \frac{\Phi_B^2}{R_0}\right), \end{aligned} \tag{4.28}$$

where Φ_B represents a magnetic flux and it is assumed to be conserved if we change the radius, R, that is $\Phi_B = \pi B_0 R_0^2 = \pi B R^2$. Equation (4.23) becomes

$$4\pi\bar{p}R^3 - 4\pi p_0 R^3 - \frac{3}{5}\frac{GM^2}{R} + \frac{1}{6\pi^2}\frac{\Phi_B^2}{R} = 0, \tag{4.29}$$

where we ignored the term $\frac{1}{6\pi^2}\frac{\Phi_B^2}{R_0}$. The last two terms are rewritten as

$$\frac{3}{5}\frac{G}{R}\left(M^2 - M_\Phi^2\right), \tag{4.30}$$

where M_Φ is defined as $3GM_\Phi^2/5 = \Phi_B^2/6\pi^2$.

This shows the effects of the magnetic fields:

1. B-fields effectively reduce the gravitational mass as $M^2 - M_\Phi^2 = M^2 - 5\Phi_B^2/(18\pi^2 G)$. This plays a part to support a cloud.

2. However, even a cloud contracts (decreasing its radius from R_0 to R), the ratio of the gravitational to the magnetic terms keeps constant since these two terms are proportional to $\propto R^{-1}$. Thus, if the magnetic term does not work initially, the gravitational term continues to predominate over the magnetic term.

If $M < M_\Phi$, a sum of last two terms in equation (4.29) is positive. Since the second term of rhs of equation (4.25) is positive, there is one R which satisfies equation (4.29) irrespective of the external pressure p_0. While, if $M > M_\Phi$, there is a maximum allowable external pressure p_0. Therefore, $M = M_\Phi$ gives a criterion whether the magnetic fields work to support the cloud or not. More realistic calculation [Mouschovias (1976a,1976b), Tomisaka et al (1988)] gives us a criterion

$$G^{1/2}\frac{dm}{d\Phi_B} = \frac{G^{1/2}\sigma}{B} = 0.17 \simeq \frac{1}{2\pi}, \tag{4.31}$$

where σ and B means the column density and the magnetic flux density. A cloud with a mass

$$M > \frac{\Phi_B}{2\pi G^{1/2}} \tag{4.32}$$

is sometimes called **magnetically supercritical**, while that with

$$M < \frac{\Phi_B}{2\pi G^{1/2}} \tag{4.33}$$

is **magnetically subcritical**.

More precisely speaking, the criterion showed in equations (4.32) and (4.33) should be applied for a cloud which has a much larger mass than the Bonnor-Ebert mass. That is, even without magnetic fields, the cloud less-massive than the Bonnor-Ebert mass has a hydrostatic configuration shown in

Figure 4.2 (left). The cloud with central density of $\rho_c = 10$ has a stable density distribution. To fit the numerical results, Tomisaka et al (1988) obtained an expression for the critical mass when the cloud has a mass-to-flux ratio $dm/d\Phi_B$, the isothermal sound speed $c_{\rm is}$, and the external pressure p_0 as

$$M_{cr} = 1.3 \left\{ 1 - \left[\frac{1/2\pi}{G^{1/2} dm/d\Phi_B|_{r=0}} \right]^2 \right\}^{-3/2} \frac{c_s^4}{p_0^{1/2} G^{3/2}}. \tag{4.34}$$

This shows that the critical mass is a decreasing function of the mass-to-flux ratio or increasing function of the magnetic flux. And the critical mass becomes much larger than the Bonnor-Ebert mass $\simeq c_s^4/(p_0^{1/2} G^{3/2})$ only when the mass-to-flux ratio at the center of the cloud is reaching $1/2\pi$ at which the term in the curry bracket goes to zero. Hereafter, we call here the cloud/cloud core with mass larger than the critical mass $M_{\rm cr}$ a supercritical cloud/cloud core. The cloud/cloud core less-massive than the critical mass is subcritical.

4.3 Subcritical Cloud vs Supercritical Cloud

We have seen there is a critical mass above which the cloud has no (magneto)hydrostatic configuration but below which the cloud has at least an equilibrium state. This gives us an idea that there are two kind of clouds/cloud cores: that with a mass larger than the critical mass which has to collapse dynamically and that with a mass smaller than the critical mass which is in an equilibrium state. In the density range of $10^4{\rm cm}^{-3} \lesssim n \lesssim 10^{10}{\rm cm}^{-3}$, the interstellar gas is essentially isothermal. In this region a major cooling agent is dusts; that is, the dust is heated by the collision of molecules. The excess energy liberated at the collision increases the dust temperature. Finally the thermal emission from the dust cools down the dust again. By this process, the thermal energy of the gas is reduced. Therefore, we consider the cloud/cloud core is isothermal and study the collapse of the isothermal cloud.

Since the supercritical cloud has no hydrostatic configuration, it must evolve in a dynamical way. On the other hand, since the subcritical cloud is in a static state, it evolves in much longer time-scale of the free-fall time. Such cloud evolves by the effect called the ambipolar diffusion.

4.4 Ambipolar Diffusion

4.4.1 Ionization Rate

In the dense clouds, the ionization fraction is low. Since the uv/optical radiations from stars can not reach the cloud center, potential ionization comes from the cosmic ray particles. In this case the rate of ionization per volume is given as ζn_n, where $\zeta \sim 10^{-17}{\rm s}^{-1}$. In Figure 4.3, the ionization fraction for various density is shown (Nakano, Nishi, & Umebayashi 2002). This clearly shows that the fraction of ions decrease approximately in proportion to $n_{\rm H}^{-1/2}$ for $n_{\rm H} \lesssim 10^8{\rm cm}^{-3}$. This is understood as follows: Equilibrium balance between one kind of ion m^+ and its neutral m^0

$$m^0 \leftrightarrow m^+ + e^-, \tag{4.35}$$

is considered. The recombination (reaction from the right to left) rate per unit volume is expressed $\alpha n_e n_{m^+}$, while the ionization rate (left to right) per unit volume is ζn_{m^0}, where α means the recombination rate coefficient. Nakano (1984) obtained in the range of $10^2{\rm cm}^{-3} \lesssim n \lesssim 10^8{\rm cm}^{-3}$

$$\rho_i = C \rho_n^{1/2}, \tag{4.36}$$

where the numerical factor $C = 4.46 \times 10^{-16} {\rm g}^{1/2}\,{\rm cm}^{-3/2}$.

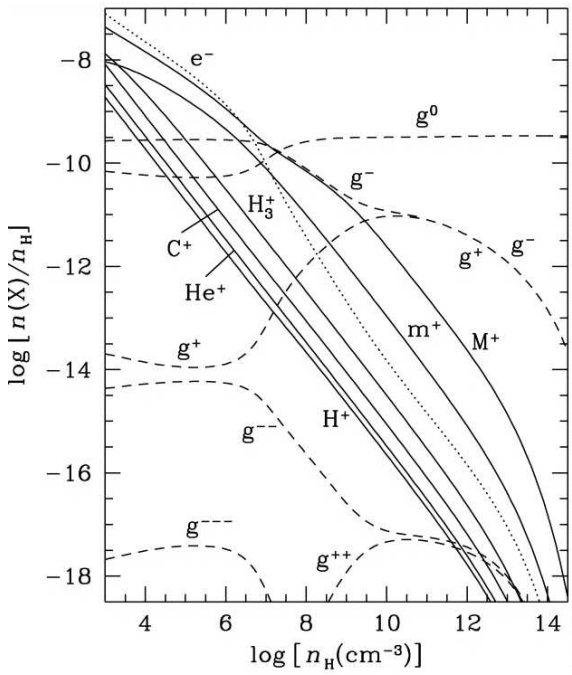

Figure 4.3: Ionization fractions $X/n_{\rm H}$ are plotted against the number density $n_{\rm H}$. The ionization rate of an H_2 molecule by cosmic rays outside the cloud is taken $\zeta_0 = 1 \times 10^{-17}{\rm s}^{-1}$. 20% of C and O and 2% of metallic elements are assumed to remain in the gas phase and the rest in grains.

4.4.2 Ambipolar Diffusion

The ionization fraction of the gas in the cloud is low. Neutral gas and the ions are coupled via mutual collisions and ions are coupled with the magnetic field. Thus, the neutral molecules, a major component of the gas, are coupled with the magnetic field indirectly via ionized ions. Equation of motion for the molecular gas is

$$\rho \frac{d\boldsymbol{u}_n}{dt} = -c_s^2 \nabla\rho - \rho\nabla\psi + \rho r\omega^2 \boldsymbol{e}_r + \boldsymbol{F}, \tag{4.37}$$

where the forces appeared in the rhs represent, respectively, the pressure force, the self-gravity, the centrifugal force, and the force exerted on the neutral component per unit volume through two-body collision with ions. The friction force has a form

$$\boldsymbol{F} = \rho_i \rho_n \gamma (\boldsymbol{v}_i - \boldsymbol{v}_n). \tag{4.38}$$

We have assumed $\rho \simeq \rho_n$ since the mass density of the charged component is much smaller than that of the neutral one. On the other hand, that for ions is

$$\rho_i \frac{d\boldsymbol{u}}{dt} = \frac{1}{4\pi}(\boldsymbol{\nabla} \times \boldsymbol{B}) \times \boldsymbol{B} - \boldsymbol{F}, \tag{4.39}$$

where we ignored the pressure and self-gravity forces compared with the Lorentz force. If the inertia of the ions are ignored [lhs of eq.(4.39)=0], equations (4.37) and (4.39) give the equation of motion similar to that of the one-fluid as follows:

$$\rho \frac{d\boldsymbol{u}}{dt} = -c_s^2 \nabla\rho - \rho\nabla\psi + \rho r\omega^2 \boldsymbol{e}_r + \frac{1}{4\pi}(\boldsymbol{\nabla} \times \boldsymbol{B}) \times \boldsymbol{B}. \tag{4.40}$$

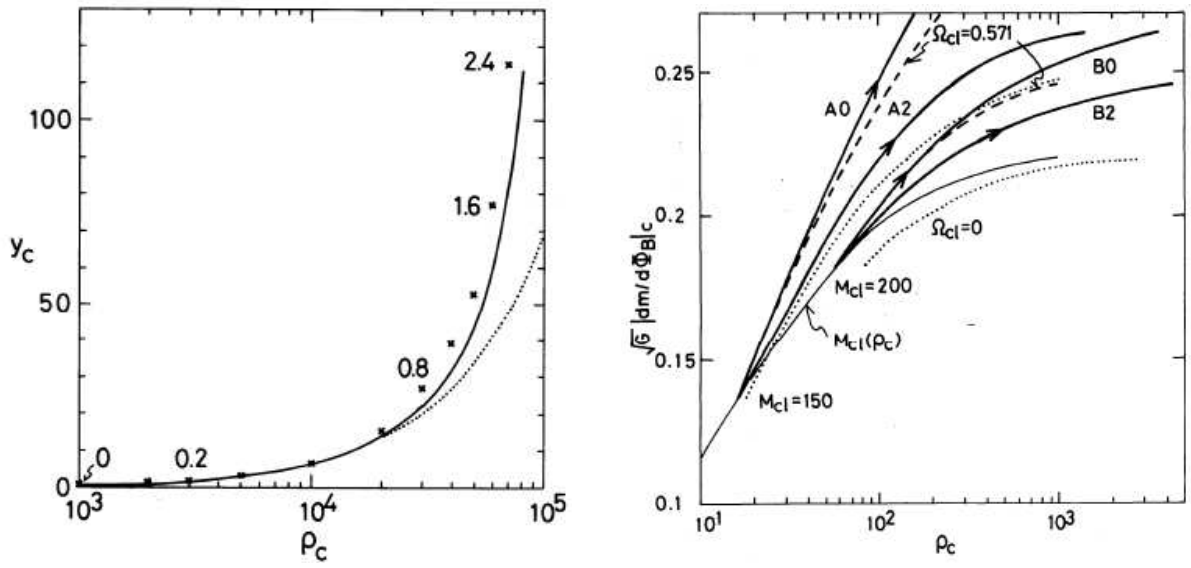

Figure 4.4: Relation central density ρ_c against mass-to-flux ratio M/Φ. Plane-parallel and axisymmetric models are illustrated in the left and right panels, respectively.

Ignoring the inertia of the ions, equation (4.39) indicates that the friction force should be balanced with the Lorentz force as

$$\boldsymbol{F} = \frac{1}{4\pi}(\boldsymbol{\nabla} \times \boldsymbol{B})\times\boldsymbol{B}. \tag{4.41}$$

Using equations (4.36) and (4.38), this gives the drift velocity of ions against the neutrals as

$$\begin{aligned} \boldsymbol{v}_D &\equiv \boldsymbol{v}_i - \boldsymbol{v}_n, \\ &= \frac{\boldsymbol{F}}{\rho_i \rho_n \gamma}, \\ &= \frac{1}{4\pi\rho_i\rho_n\gamma}(\boldsymbol{\nabla} \times \boldsymbol{B})\times\boldsymbol{B}, \\ &= \frac{1}{4\pi C\gamma\rho_n^{3/2}}(\boldsymbol{\nabla} \times \boldsymbol{B})\times\boldsymbol{B}. \end{aligned} \tag{4.42}$$

Since the Lorentz force works outwardly, the drift velocity $\boldsymbol{v}_D$ also points outwardly. Viewing from the ions and magnetic field lines, $\boldsymbol{v}_n - \boldsymbol{v}_i$ points inwardly. Thus, the mass in a flux tube varies with time; that of the cloud center increases while that of the cloud surface decreases. The ambipolar diffusion is a process to change the mass distribution against the magnetic flux tube.

How is the structure affected by the increase of mass/flux ratio at the cloud center? Here, we will derive the relation between the mass-to-flux ratio and central density and answer the question. Numerical calculation is necessary for the axisymmetric (realistic) cloud. However, this can be obtained for the case of a plane-parallel disk in which the magnetic field is running parallel to the disk, For the plane-parallel disk the hydrostatic balance is achieved as

$$\frac{\partial}{\partial z}\left(p + \frac{B^2}{8\pi}\right) = -\rho\frac{\partial\psi}{\partial z} = -2\pi G\rho\sigma, \tag{4.43}$$

where $\sigma = \int_{-z}^{z}\rho dz$. Equation (4.43) is integrated to obtain the relation between the variables at the

center $z = 0$ as

$$p_c + \frac{B_c^2}{8\pi} - \left(p_s + \frac{B_s^2}{8\pi} \right) = \frac{\pi G}{2} \sigma_s^2, \tag{4.44}$$

where we used $d\sigma/dz = 2\rho$. This is rewritten as

$$\frac{\rho_c}{\rho_s} + \frac{1}{8\pi} \left(\frac{B_c}{\rho_c} \right)^2 \frac{\rho_s}{c_s^2} \left(\frac{\rho_c}{\rho_s} \right)^2 - \frac{1}{8\pi} \left(\frac{B_s}{\rho_s} \right)^2 \frac{\rho_s}{c_s^2} = \frac{\pi G \sigma_s^2}{2\rho_s c_s^2} + 1. \tag{4.45}$$

In the second term of lhs, $y_c \equiv (\rho_c/B_c)(c_s/\rho_s^{1/2})$ is a nondimensional mass flux ratio at the center and this is related to the center-to-surface density ratio $\rho_c' \equiv \rho_c/\rho_s$. Using these nondimensional variables, equation (4.45) is expressed as

$$\rho_c' + \frac{(\rho_c')^2}{8\pi y_c^2} - \frac{1}{8\pi y_s^2} = \bar{\rho}_c', \tag{4.46}$$

where $\bar{\rho}_c' \equiv \pi G \sigma_s^2/(2\rho_s c_s^2) + 1$ represents the central density necessary for the disk to be supported without a magnetic field ($y \to \infty$). Figure 4.4 (left) illustrates this relation. This shows that if the central mass-to-flux ratio increases (moving upward), the central density increases. In low density, $\rho_c' \ll \bar{\rho}_c'$, equation (4.46) indicates that $\rho_c' \propto y_c \propto \rho_c/B_c$. This means that on the low density regime, the density increases but the strength of magnetic field does not increase. Equation (4.46) also indicates that y_c increase much as $y_c \to \bar{\rho}_c' y_s$ when $\rho_c' \to \bar{\rho}_c'$. This relation between mass-to-flux ratio and the central density is well fitted to the numerical calculation of plane-parallel disk cloud driven by the ambipolar diffusion by Mouschovias, Paleologou, & Fiedler (1985). Does this indicate that the mass-to-flux ratio increases much when the central density increases, for example, from $10^4 \mathrm{cm}^{-3}$ to $10^6 \mathrm{cm}^{-3}$?

From this point, quasistatic evolution of the magnetized cloud was first studied by Nakano (1979) adopting a method seeking for magnetohydrostatic configuration (Mouschovias 1976a, 1976b). He obtained that the magnetic flux to mass ratio near the center of the cloud does not decrease much below a critical density above which magnetohydrostatic configurations no more exist. Paleologou & Mouschovias (1983), Shu (1983), and Mouschovias, Paleologou, & Fiedler (1985) gave a completely different result. That is, the magnetic flux to mass ratio near the center decreases much when the density becomes larger than $n \gtrsim 10^6 \mathrm{cm}^{-3}$. Critical discussion has been done between them[1] . However, we have now realized that the difference comes from the geometry assumed.

Relation of the mass-to-flux ratio to the central density for the axisymmetric realistic (not plane-parallel disk) cloud is plotted in Figure 4.4 (right) (Tomisaka, Ikeuchi, & Nakamura 1990). The central mass-to-flux ratio increases by the ambipolar diffusion. This increase the central density. Lines with arrows indicate the evolutionary paths driven by the ambipolar diffusion. It is to be noticed that the relation is completely different from that of the plane-parallel disk. Increase of the mass-flux ratio is small although the central density increases much. This indicates that in the quasistatic evolution driven by the ambipolar diffusion the mass-flux ratio does not increase much in contrast to the plane-parallel case.

In fully ionized plasma, the magnetic field is coupled to the matter. However, in the low ionized gas the magnetic field is coupled only to the ions. Thus the induction equation of magnatic field should be written

$$\frac{\partial \boldsymbol{B}}{\partial t} + \boldsymbol{\nabla} \times (\boldsymbol{v_i} \times \boldsymbol{B}) = 0. \tag{4.47}$$

[1] One of the reasons why large increase in the mass/flux ratio is favored is understood as follows: There have been a long-standing "magnetic flux problem of stars" in which the magnetic flux of, say, $1 M_\odot$ main-sequence star $\Phi \sim XX\mathrm{G\,cm}^2$ is much smaller than that of the parent cloud $\Phi \sim XX\mathrm{G\,cm}^2$. The magnetic flux must be reduced in the star formation process. If the mass-flux ratio increases much in these density range, this might resolve the magnetic flux problem of stars.

This leads to the final expression as

$$\frac{\partial \boldsymbol{B}}{\partial t} + \boldsymbol{\nabla} \times (\boldsymbol{v_n} \times \boldsymbol{B}) + \boldsymbol{\nabla} \times \left\{ \frac{1}{4\pi C \gamma \rho_n^{3/2}} [(\boldsymbol{\nabla} \times \boldsymbol{B}) \times \boldsymbol{B}] \times \boldsymbol{B} \right\} = 0, \tag{4.48}$$

where we used the expression of the drift velocity [equation (4.42)]. In the isothermal cloud, there is a maximum mass supported by the magnetic field. Since in the subcritical cloud $M < M_{cr}$ the magnetic flux escapes from the center, the critical mass decreases with time. After the critical mass becomes smaller than the actual mass ($M_{\rm cl} > M_{cr}$), there is no hydrostatic configuration. The cloud evolves into the supercritical cloud region and experiences dynamical collapse.

4.5 Dynamical Collapse

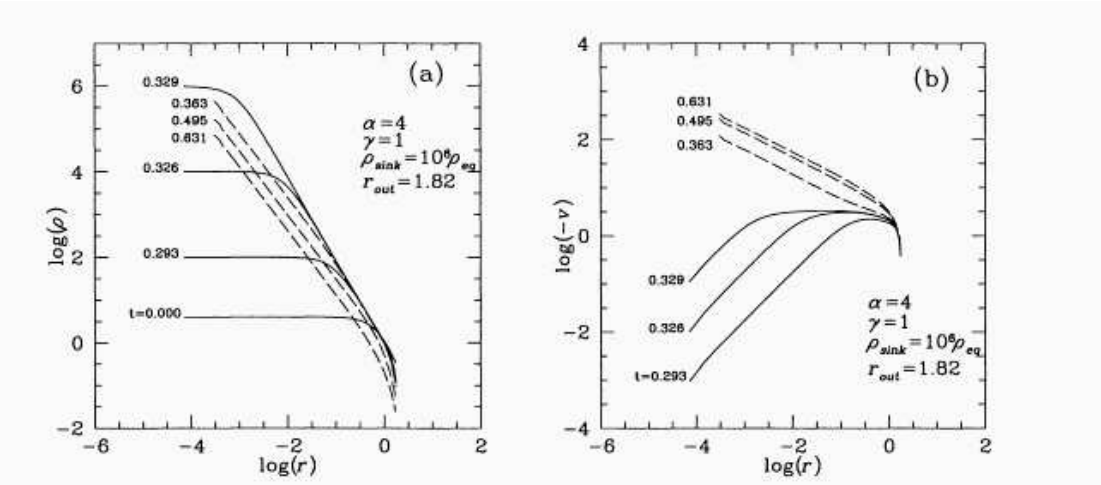

g. 1. Radial profiles of (a) density and (b) velocity for the $\alpha = 4$ isothermal model (model A2). The solid and dashed curves denote the physical quantities before and after core formation, respectively. The number attached to each curve denotes the evolution time from the initial state. In this model, we set $\rho_{\rm sink} = 10^6 \rho_{\rm eq}$.

Figure 4.5: Evolution of isothermal clouds massive than the Bonnor-Ebert mass. Density (*left*) and velocity (*right*) distributions are illustrated. Solid lines show the cores of the preprotostellar phase (prestellar core) and dashed lines show those of protostellar phase (protostellar core). The evolution of the protostellar phase is studied by the sink-cell method, where we assume the gas that entered in the sink-cells is removed from finite-difference grids and add to the point mass sitting at the center of the sink-cells which corresponds to a protostar.

In 1969, Larson (1969) and Penston (1969) found a self-similar solution which is suited for the dynamical contraction. Figure 4.5 is a radial density distribution for a spherical collapse of an isothermal cloud, where the cloud has a four-times larger mass than that of the Bonnor-Ebert mass. Although the figure is taken from a recent numerical study by Ogino et al (1999), a similar solution was obtained in Larson (1969). We can see that the solution has several characteristic points as follows:

1. The cloud evolves in a self-similar way. That is, the spatial distribution of the density (left) at $t = 0.326$ is well fitted by that at $t = 0.293$ after shifting in the $-x$ and the $+y$ directions. As for the infall velocity spatial distribution, only a shift in the $-x$ direction is needed.

2. The density distribution in the envelope, which is fitted by $\propto r^{-2}$, is almost unchanged. Only the central part of the cloud (high-density region) contracts.

3. The time before the core formation epoch (the core formation time t_0 is defined as the time at which the central density increases greatly) is a good indicator to know how high the central density is. That is, reading from the figure, at $t - t_0 = 0.003$ ($t = 0.326$) the central density reaches $\rho_c \simeq 10^4$ and at $t - t_0 = 0.036$ ($t = 0.293$) the density is equal to $\rho_c \simeq 10^2$. This shows the maximum (central) density is approximately proportional to $(t - t_0)^2$, which is reasonable from the description of the free-fall time $\propto \rho^{-1/2}$.

The basic equations of spherical symmetric isothermal flow are

$$\frac{\partial \rho}{\partial t} + \frac{1}{r^2}\frac{\partial}{\partial r}(r^2 \rho v) = 0, \tag{4.49}$$

$$\frac{\partial v}{\partial t} + v\frac{\partial v}{\partial r} + \frac{c_{\rm is}^2}{\rho}\frac{\partial \rho}{\partial r} + \frac{GM}{r^2} = 0, \tag{4.50}$$

$$M(r,t) = M(0,t) + \int_0^r 4\pi r'^2 \rho(r',t) dr', \tag{4.51}$$

where $M(r,t)$ represents the mass included in the radius r and $M(0,t)$ denotes the mass of the protostar. A self-similar solution which has a form

$$\rho(r,t) = \frac{\Omega(\xi)}{4\pi G(t-t_0)^2}, \tag{4.52}$$

$$v(r,t) = c_{\rm is} V(\xi), \tag{4.53}$$

$$M(r,t) = \frac{c_{\rm is}^3 |t-t_0|}{G} m(\xi) \tag{4.54}$$

$$\xi = \frac{r}{c_{\rm is}|t-t_0|}, \tag{4.55}$$

should be found, where Ω and V are functions only on ξ. For example, equation (4.52) asks the shape of the density distribution is the same after resizing of equation (4.55) $r \to r/c_s|t-t_0|$ and re-normalizing $\rho \to \rho \cdot 4\pi G(t-t_0)^2$ as $\Omega(\xi)$. Since

$$\frac{\partial}{\partial t} = \frac{d}{d\xi}\left(\frac{\partial \xi}{\partial t}\right)_r = \frac{r}{c_{\rm is}|t-t_0|^2}\frac{d}{d\xi}, \tag{4.56}$$

and

$$\frac{\partial}{\partial r} = \frac{d}{d\xi}\left(\frac{\partial \xi}{\partial r}\right)_t = \frac{1}{c_{\rm is}|t-t_0|}\frac{d}{d\xi}, \tag{4.57}$$

the basic equations for the spherical symmetric model yield

$$m = (\xi - V)\xi^2 \Omega, \tag{4.58}$$

$$\left[(\xi - V)^2 - 1\right]\frac{dV}{d\xi} = \left[\Omega(\xi - V) - \frac{2}{\xi}\right](\xi - V), \tag{4.59}$$

$$\frac{(\xi - V)^2 - 1}{\Omega}\frac{d\Omega}{d\xi} = \left[\Omega - \frac{2}{\xi}(\xi - V)\right](\xi - V), \tag{4.60}$$

Equations (4.59) and (4.60) have a singular point at which $(\xi - V)^2 - 1 = 0$ or $V = \xi \pm 1$. Since the point of ξ =const moves with $c_{\rm is}$, the flow velocity relative to this ξ =const is equal to $v - c_{\rm is}\xi = (V - \xi)c_{\rm is}$.

Thus the singular point ξ_* at which $V = \xi \pm 1$ corresponds to a sonic point. Therefore, since the flow has to pass the sonic point smoothly, the rhs of equations (4.59) and (4.60) have to be equal to zero at the singular point ξ_*. This gives at the sonic pont $\pm\xi_* > 0$,

$$\Omega - \frac{2(\xi - V)}{\xi} = \Omega(\xi - V) - \frac{2}{\xi} = 0, \tag{4.61}$$

which leads to

$$V_* = \xi_* \mp 1, \tag{4.62}$$

$$\Omega_* = \pm\frac{2}{\xi_*}. \tag{4.63}$$

These equations (4.58), (4.59) and (4.60) have an analytic solution

$$V(\xi) = 0, \quad \Omega = \frac{2}{\xi^2}, \quad m = 2\xi, \quad -\infty < \xi < \infty \tag{4.64}$$

This is a solution which agrees with the Chandrasekhar's SIS. Generally, solutions are obtained only by numerical integration. $|\xi \to \infty|$ the solution have to converge to an asymptotic form of

$$V(\xi) = V_\infty - \frac{A-2}{\xi} + \frac{V_\infty}{\xi^2} + \frac{4V_\infty + (A-2)(A-6)}{6\xi^3} + \mathcal{O}(\xi^{-4}), \tag{4.65}$$

$$\Omega(\xi) = \frac{A}{\xi^2} - \frac{\Omega_\infty(A-2)}{2\xi^4} + \mathcal{O}(\xi^{-6}), \tag{4.66}$$

This shows that for sufficiently large radius the gas flows with a constant inflow velocity $V_\infty c_{\rm is}$.

This has a solution in which the density and the infall velocity should be regular with reaching the center ($\xi \ll 1$). Such kind of solution is plotted in Figure 4.6 (left) and Figure 4.6 (right) with $t < 0$. This time evolution is expected from the self-similar solution. This shows that

$$\rho \quad \begin{cases} \simeq \rho_c & \text{(in the central region)} \\ \propto r^{-2} & \text{(in the outer envelope)} \end{cases} \tag{4.67}$$

$$v \quad \begin{cases} \propto r & \text{(in the central region)} \\ \simeq 3.28 c_{\rm is} & \text{(in the outer envelope)} \end{cases} \tag{4.68}$$

Reaching the outer boundary the numerical solution (Fig.4.5) differs from the self-similar solution (Fig.4.6). For example, v is reduced to zero in the numerical simulations, while it reaches a finite value 3.28 in the self-similar solution. And as for the density distribution, ρ drops near the outer boundary in the numerical simulations while it decreases proportional to $\propto r^{-2}$. However, in the region except for the vicinity of the outer boundary the self-similar solution expresses well the dynamical collapse of the spherical isothermal cloud. This solution gives the evolution of a pre-protostellar core formed in a supercritical cloud/cloud core.

4.5.1 Inside-out Collapse Solution

In 1977 Shu found another self-similar solution which is realized after a central protostar with infinitesimal mass is formed in the singular isothermal sphere solution. The gas begins to accrete to the protostar. Outside the region where the accretion occurs, the initial SIS is kept unchanged, since the SIS is a hydrostatic solution. And the front of accretion expands radially outward in time. Since the inflow region expand outwardly, he called it **the inside-out collapse solution**. In Figure 4.7, the

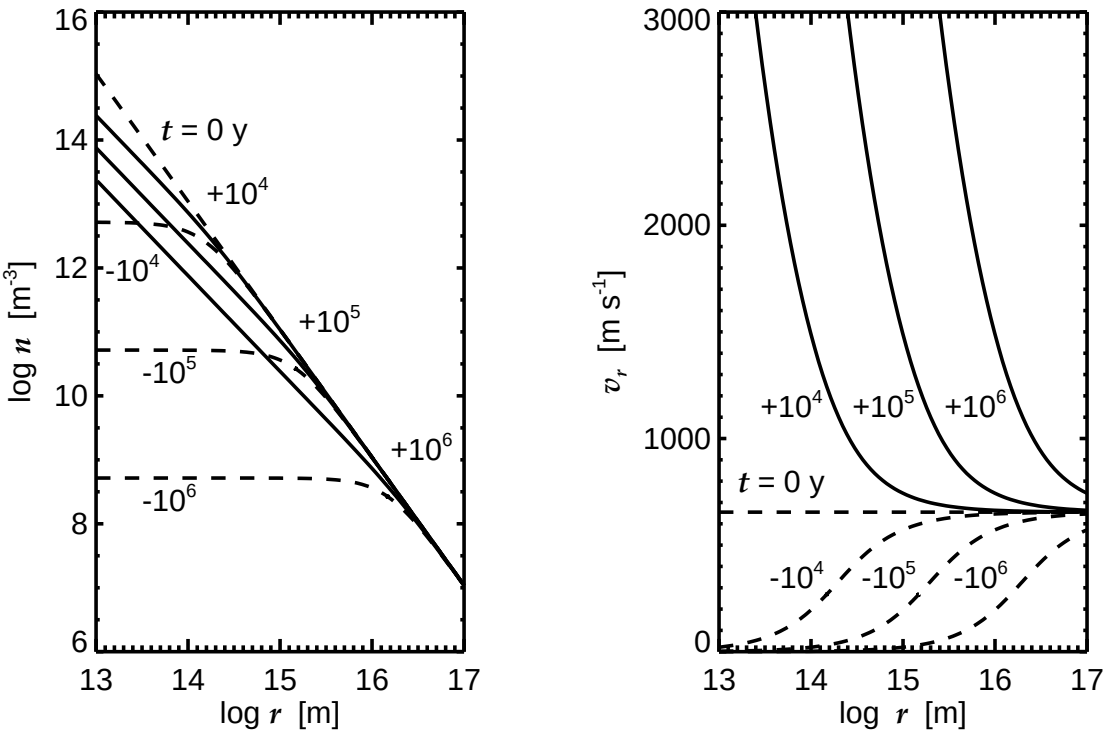

Figure 4.6: A self-similar solution indicating a dynamical collapse of isothermal spherical cloud (Larson-Penston solution). Spatial distribution of the density and inflow velocity which are expected from the self-similar solution are plotted. Dashed lines show the evolution prestellar core and solid lines show that of protostellar core. Taken from Hanawa (1999).

evolution is shown for density and inflow velocity. This solution gives the evolution of a protostellar core formed in a subcritical cloud/cloud core.

Using equations (4.65) and (4.66) and assuming the inflow velocity should reduce at large radius, we obtain

$$V(\xi) = -\frac{A-2}{\xi} - \frac{(A-2)(A-6)}{6\xi^3} + \cdots, \tag{4.69}$$

$$\Omega(\xi) = \frac{A}{\xi^2} - \frac{A(A-2)}{2\xi^4} + \cdots. \tag{4.70}$$

Since $\xi \to \infty$ means $t \to t_0$ (if r is finite), $\Omega(\xi) \to A/\xi^2$ means that

$$\rho(r, t_0) = \frac{Ac_{\rm is}^2}{4\pi G r^2}. \tag{4.71}$$

Comparing with the SIS, when $A = 2$ this gives the SIS and when $A > 2$ this gives a density distribution in which the pressure is inefficient and the cloud is contracting. The solution with $A > 2$ is obtained by a procedure as (1) at a sufficiently large radius ξ_1, calculate $V(\xi_1)$ and $\Omega(\xi_1)$. (2) from these values, integrate equations (4.59) and (4.60) inwardly. Figure 4.7 show the solution of this type. The solution with $A > 2$ inflow speed is accelerated towards the center. Decreasing A ($A \to 2$), it is shown that an outer part $\xi \gtrsim 1$ reaches $V \to 0$. For $A = 2^+$, the solution reaches the singular line $V = -\xi + 1$ at $\xi = 1$ ($V = 0$) [2] . Since $V = 0$ and $\Omega = 2$ at $\xi = 1$, this solution with $A = 2^+$ converges to the SIS at $\xi = 1$. This means that if there is an infinitesimally small amount of excess mass at the center of SIS, the accretion begins from the center while outside a radius the cloud is left static. The inner part of the solution $\xi \lesssim 1$, V and Ω are well expressed as $V \propto \xi^{1/2}$ and $\Omega \propto \xi^{3/2}$.

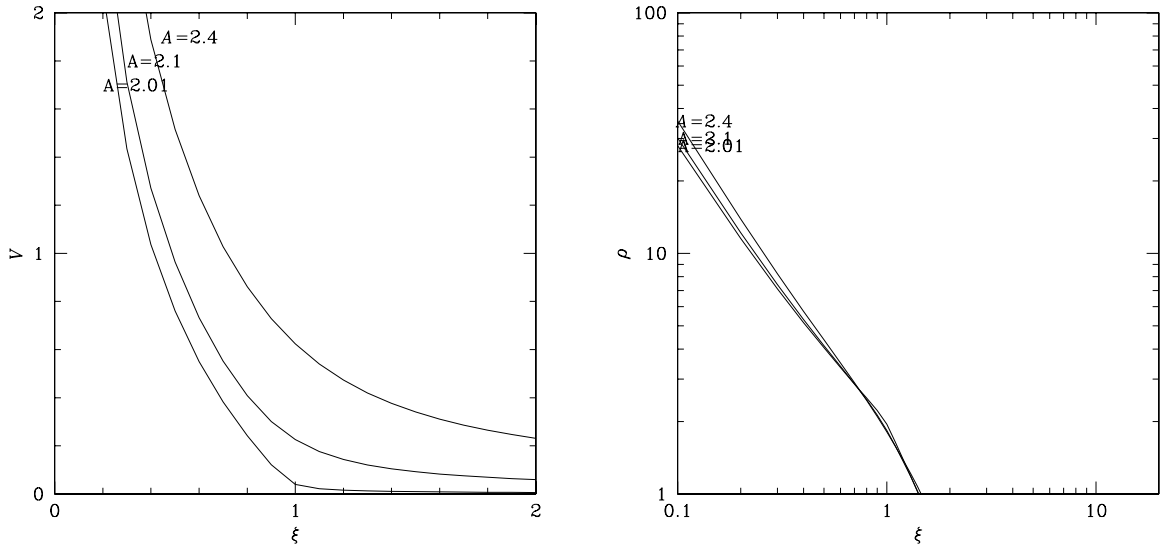

Figure 4.7: Self-similar solution which shows the inside-out collapse. (*Left*:) Infall velocity ($-V = -v/c_{\rm is}$) is plotted against the similarity variable $\xi \equiv r/c_{\rm is}(t - t_0)$. Three curves correspond to models $A = 2.4$, 2.1, and 2.01. (*Right*:) Density ($\Omega = 4\pi G\rho(t - t_0)^2$) is plotted against the similarity variable $\xi \equiv r/c_{\rm is}(t - t_0)$.

[2] This means $A = 2 + \epsilon$ and $\epsilon > 0$ and $\to 0$

The power-law distributions of $V \propto \xi^{1/2}$ and $\Omega \propto \xi^{3/2}$ are explained as follows: Conservation of the total energy of an inflowing gas shell is expressed as

$$\frac{v^2}{2} - \frac{GM_r}{r} = -\frac{GM_{r_0}}{r_0}, \tag{4.72}$$

where r_0 denotes the initial radius of a gas shell and $M_{r_0} = M_r$ represents the mass inside the gas shell. Neglecting GM_{r_0}/r_0 compared with the term GM_r/r, this gives

$$v \simeq \left(\frac{2GM_r}{r}\right)^{1/2} \propto r^{-1/2}, \tag{4.73}$$

where we assumed a major part of M_r comes from the mass of a protostar M_*, that is, $M_r = M_* + \int_0^r \rho 4\pi r^2 dr \simeq M_*$ Since the average density inside the radius r $\bar{\rho}(< r) = \int_0^r \rho 4\pi r^2 dr / \int_0^r 4\pi r^2 dr = 3\rho(r)$ for SIS distribution, the time necessary for a gas shell to reach the center is proportional to $\propto \bar{\rho}(< r)^{-1/2} \propto \rho(r)^{-1/2} \propto r^1 \propto (t - t_0)^1$, where we used a fact that the front of accretion expands with a constant speed $c_s$is. This means that the time necessary for the gas shell to travel from the radius of the accretion wave front to the center is proportional to $t - t_0$. Since the mass of the shell which begins accretion in a unit time is equal to $\rho(r)4\pi r^2 c_{\rm is}$ and is constant irrespective of $t - t_0$. These two facts indicate that the mass accretion rate is constant in time. That is,

$$\dot{M} = 4\pi r^2 \rho v = \text{const.} \tag{4.74}$$

Since the mass swept by the sound wave per unit time is equal to $\dot{M}_{sw} = 4\pi r^2 \rho_{\rm SIS} c_s = 2c_s^3/G$, the accretion rate is proportional to c_s^3/G. Shu (1977) obtained the accretion rate

$$\dot{M} = 0.975 \frac{c_s^3}{G}, \tag{4.75}$$

for SIS $A = 2^+$. Using this equation, equations (4.73) and (4.74) indicate that the spatial density distribution is expressed by a power-law as

$$\rho(r) \propto r^{-3/2}, \tag{4.76}$$

which is valid for the region except for the vicinity of the front of the accretion.

4.5.2 Protostellar Evolution of Supercritical Clouds

What is a protostellar core formed in a supercritical cloud/cloud core? Is this different from the inside-out solution of Shu (1977)? A solution which corresponds to the protostellar core is obtained by Hunter (1977) and Whitworth and Summers (1985). This is a solution with $t > t_0$ in equation (4.55). The asymptotic behaviors of the density and infall velocity reaching the center are different from that of the Larson-Penston self-similar solution for a prestellar collapse. That is,

$$\Omega \quad \begin{cases} \to \text{finite} & (\text{LP}) \\ \to \text{infinite} & (\text{Inside} - \text{out}) \end{cases} \tag{4.77}$$

$$V \quad \begin{cases} \to \text{finite} & (\text{LP}) \\ \to \text{infinite} & (\text{Inside} - \text{out}) \end{cases} \tag{4.78}$$

Using the boundary conditions suitable for the inside-out type solution, another self-similar solution is obtained. In Figure 4.6, such kind of solution is also plotted for $t > 0$.

Take notice that the solutions of $t < t_0$ (prestellar) and $t > t_0$ (protostellar) agree with each other at $t = t_0$. Even if the boundary conditions at the center for the **similarity variables**, V and Ω, are completely different, the difference between the two is small in the physical variable v and ρ. Therefore, the evolution of a supercritical core is thought to be expressed by the Larson-Penston self-similar solution extended to the protostellar core phase by Hunter (1977) and Whitworth and Summers (1985).

Assume that we observe a protostellar core and obtain their density and infall velocity spatial distributions. Can we distinguish which solution is appropriate for the Shu's inside-out solution or the extended Larson-Penston solution? This seems hard, because the structure of density and velocity distributions are similar after the protostar is formed: the density and velocity show almost similar power-law as $\rho \propto r^{-3/2}$ and $v \propto r^{-1/2}$ irrespective of the inside-out solution or the extended Larson-Penston solution. The region where the infall velocity is accelerated toward the center (accretion-dominated region) is expanding after the protostar is formed. Therefore, to distinguish between the two solutions becomes harder and harder after the protostar is formed. The difference would be large and we would have a definite answer which solution is appropriate to describe the cloud collapse, if we can observe a very young protostellar core or a preprotostellar core which shows dynamical collapse. However, since the time-scale of such a phase is much shorter than the evolved protostellar phase or a younger preprotostellar core, the number of such kind of objects would be small ($\tau_{\rm ff} \propto \rho^{-1/2}$). Therefore, we are looking for such objects just before or after the protostar formation.

4.6 Accretion Rate

Using equation (2.26), the necessary time for a mass-shell at R to reach the center (free-fall time) is expressed as

$$T(R) \equiv \left(\frac{R^3}{2GM(R)} \right)^{1/2} \frac{\pi}{2} \tag{4.79}$$

(for detail of this section see Ogino, Tomisaka, & Nakamura 1999).

Consider two shells whose initial radii are R and $R + \Delta R$. The time difference for these two shells to reach the center $\Delta T(R)$ can be written down using equation (4.79) as

$$\Delta T(R) = \frac{\pi R^{1/2}}{2^{3/2}(GM(R))^{1/2}} \left[\frac{3}{2} - \frac{R}{2M(R)} \frac{dM(R)}{dR} \right] \Delta R. \tag{4.80}$$

Mass in the shell between R and $R + \Delta R$, $\Delta M \equiv M(R + \Delta R) - M(R) = (dM/dR)\Delta R$, accretes on the central object in $\Delta T(R)$. Thus, mass accretion rate for a pressure-free cloud is expressed as $\Delta M/\Delta T$. This leads to the expression as

$$\frac{dM}{dT}(R) = \frac{2^{3/2}}{\pi} \frac{G^{1/2} M(R)^{3/2}}{R^{3/2}} \frac{\frac{R}{M(R)} \frac{dM(R)}{dR}}{\frac{3}{2} - \frac{R}{2M(R)} \frac{dM(R)}{dR}}. \tag{4.81}$$

This gives time variation of the accretion rate. Consider two clouds with the same density distribution $\partial \log \rho / \partial r$ but different absolute value. Since these two clouds have the same $\partial \log M(R)/\partial \log R$, the mass accretion rate depends only on $M(R)/R$, and is expressed as

$$\frac{dM}{dT}(R) \propto M(R)^{3/2}. \tag{4.82}$$

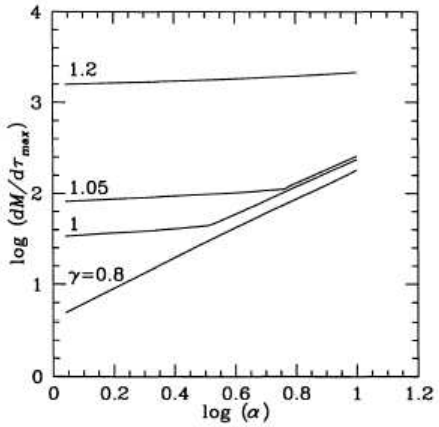

Fig. 8. Maximum of mass-accretion rate as a function of α for the models with various γ. The unit of the mass-accretion rate is taken to be c_s^3/G, which is equal to $1.6 \times 10^{-6} M_\odot$ yr^{-1} for $c_s = 0.19$ km s^{-1} ($T = 10$ K). The unit of time is taken to be $1/\sqrt{G\rho_{eq}}$, which is equal to 6.3×10^5 yr for $\rho_{eq} = 10^4$ cm^{-3}. The number attached with each line denotes the value of γ. For each line, we calculated many models with different α, i.e., $\alpha = 1.1, 1.5, 2, 2.5, \ldots, 10$.

Figure 4.8: Mass accretion rate against the typical density of the cloud.

This indicates that the accretion rate is proportional to $\rho^{3/2}$, while the time scale is to $\rho^{-1/2}$. This is confirmed by hydrodynamical simulations of spherical symmetric isothermal clouds (Ogino et al.1999). When the initial density distribution is the SIS as $\rho \propto r^{-2}$, the mass included inside R is proportional to radius $M(R) \propto R$. In this case, equation (4.81) gives a constant accretion rate in time. In Figure 4.8 we plot the mass accretion rate against the cloud density. α represents the cloud density relative to that of a hydrostatic Bonnor-Ebert sphere. This shows clearly that the mass accretion rate is proportional to $\alpha^{3/2}$ for massive clouds $\alpha > 4$. This is natural since the assumption of pressure-less is valid only for a massive cloud in which the gravity force is predominant against the pressure force.

Similar discussion has been done by Henriksen, André, & Bontemps (1997) to explain a decline in the accretion rate from Class 0 to Class I IR objects. They assumed initial density distribution of

$$\rho \begin{cases} = \rho_0 \quad (r \le r_N), \\ = \rho_0 \left(\frac{r}{r_N}\right)^{-2/D_1} \quad (r > r_N), \end{cases} \tag{4.83}$$

as shown in Figure 4.9. Since the free-fall-time of the gas contained in the inner core $r \le r_N$ is the same, such gas reaches the center once. It makes a very large accretion rate at $t = (3\pi/32G\rho_0)^{1/2}$ as $\dot{M} = (4\pi/3)\rho_0\delta(t - (3\pi/32G\rho_0)^{1/2})$. If $D_1 = 1$, $\rho \propto r^{-2}$ for $r \gtrsim r_N$. Since $M \propto R^1$ and $t_{ff} \propto R$, equation(4.81) predicts $\dot{M} \propto R^0 \propto t^0$. A constant accretion rate is expected for this power-law and the accretion rate is converged to a constant value after $M(r_N) \ll M(r)$. If $D_1 = 2$, $\rho \propto r^{-3}$ for $r \gtrsim r_N$. Since for this power $M \propto R^2$ and $t_{ff} \propto R^{1/2}$, equation(4.81) predicts $\dot{M} \propto R^{3/2} \propto t^3$. They gave $\dot{m} \propto t^{3D_1-3}$ for $D_1 > 2/3$.

Problem

Show that $\dot{M} \propto t^{3D_1-4/3D_1}$ if $\rho \propto r^{-2/D_1}$ and $D_1 < 2/3$ [Henriksen, André, & Bontemps (1997)].

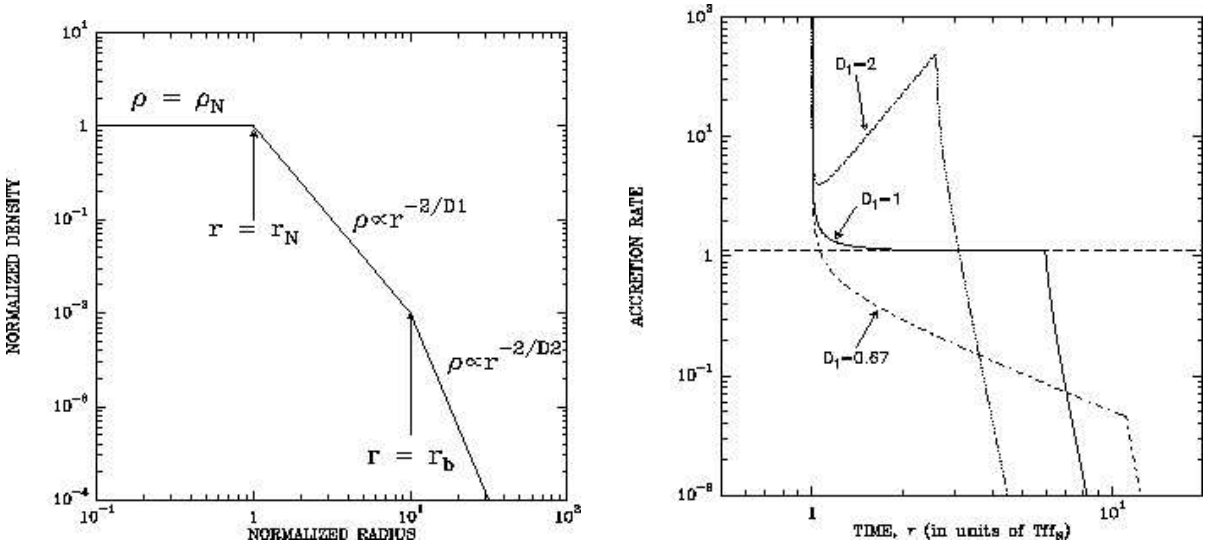

Figure 4.9: A model proposed to explain time variation in accretion rate by Henriksen, André, & Bontemps (1997). The density distribution $\rho(r)$ at $t = 0$ (left) and expected accretion rate (right).

4.7 Outflow

In chapter 1, we mentioned 'outflows' ejected from the protostars and pre-main-sequence stars. L1551 IRS5 is a typical example which shows a number of outflows are ejected in the course of star formation. One is molecular outflow, whose lobes extends $L \sim 0.5(D/160\mathrm{pc})\mathrm{pc}$ in two opposite directions from the IRS-5 (Snell et al 1980). This is traced by CO $J = 1 \rightarrow 0$ emission line. They estimated an expansion velocity of the CO gas of $V_{\mathrm{CO}} \sim 15\mathrm{km\,s^{-1}}$, a mass of 0.3 $M_\odot$. The dynamical age is equal to $\tau_{dyn} = L/V_{\mathrm{CO}} \sim 3 \times 10^4\mathrm{yr}$. Inside the CO outflow lobe, several Herbig-Haro objects are found, which are emission-line nebulosities. Proper motion studies have revealed the motion of such H-H objects. Cudworth & Herbig (1979) reported HH28 and 29 have $0.15 - 0.20\mathrm{arcsec\,yr^{-1}}$, which corresponds to $150 - 200\mathrm{km\,s^{-1}}$. In a neighbor of the IR source a stellar jet is found (Mundt & Fried 1983) by optical emission lines. Its size is equal to $17\mathrm{arcsec} = 4 \times 10^{16}\mathrm{cm}(D/160\mathrm{pc})$ and the jet indicates rather well-collimated shape (the opening angle $\simeq 10°$). The relationship between these two outflows (massive molecular outflow and less massive optical jet) are not clear yet.

4.7.1 Magneto-driven Model

To accelerate gas till supersonic speed, the magnetic force is considered to be an important player. Blandford & Payne (1982) have proposed the "magneto-centrifugal wind model" for the acceleration in two-dimensional axisymmetric configuration.

Figure 4.10 explains the magneto-centrifugal wind mechanism (Fig. 1 of Blandford & Payne 1982). Consider a disk under the gravity of a central star with mass M_*. Assume that gas in the disk at the radius r_0 rotates with a Kepler speed of

$$v_\phi(r_0) = \left(\frac{GM_*}{r_0}\right)^{1/2}. \tag{4.84}$$

Consider a gas parcel whose original position was $(r_0, z = 0)$. The effective potential for the particle

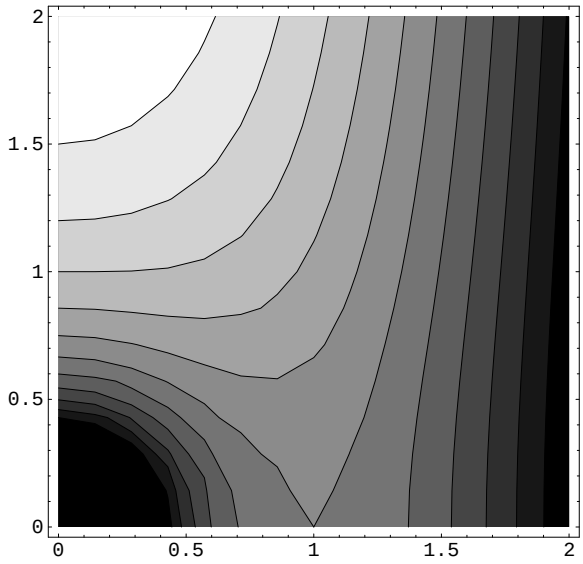

Figure 4.10: Magneto-centrifugal wind model. Figure shows the effective potential for a gas parcel with conserving the angular rotation speed ω_0 of the disk (eq.4.85). The gas parcel is assumed to located originally at $(r_0, 0)$. The x- and y-axes mean normalized distance from the central star as r/r_0 and z/r_0. The darker color represents the deeper potential.

rotating with an angular rotation speed of $\omega_0 = v_\phi(r_0)/r_0$ is written as

$$\phi(r,z) = -\frac{GM_*}{(r^2+z^2)^{1/2}} - \frac{1}{2}r^2\omega_0^2 = -\frac{GM_*}{r_0}\left[\frac{r_0}{(r^2+z^2)^{1/2}} + \frac{1}{2}\left(\frac{r}{r_0}\right)^2\right], \tag{4.85}$$

where $\omega_0 = (GM)^{1/2}/r_0^{3/2}$. (Be careful that ordinary effective potential is calculated for constant angular momentum. However, this is for constant angular rotation speed.) The gas will co-rotate with the same angular rotation speed as the disk, if the magnetic field is sufficiently strong. Equation (4.85) corresponds the effective potential for the gas co-rotating with the disk at r_0. Figure 4.10 plots the isopotential contour lines for the effective potential [eq.(4.85)]. The contour line passing the point $(r_0, 0)$ represents $\Phi = -3GM/2r_0$. The angle between the isopotential line of $\Phi = -3GM/2r_0$ and the r-axis is equal to $\pm 60^\circ$ (see problem below). Further, it can be obtained that the effective potential increases upwardly while it decreases with reaching the central star or radially outwardly.

This leads to an important conclusion that

1. If the angle between the magnetic field line and the r-axis $\theta_{\rm mag}$ is larger than 60° ($\theta_{\rm mag} > 60^\circ$), gas parcel moving along the field line must climb the effective potential. It needs extra energy to depart from the disk.
2. If $\theta_{\rm mag} < 60^\circ$, gas parcel moving along the field line slides down the effective potential. It can depart from the disk without extra energy.

Be careful that this is valid if the magnetic field is sufficiently strong. If the Kepler disk is threaded with the magnetic field lines with a shallow angle, and if the angular momentum is sufficiently transferred along the magnetic field line, in this case, the gas is accelerated by the extra centrifugal force and finally escapes from the potential well of the central star. This mechanism is called the "magneto-centrifugal wind" mechanism.

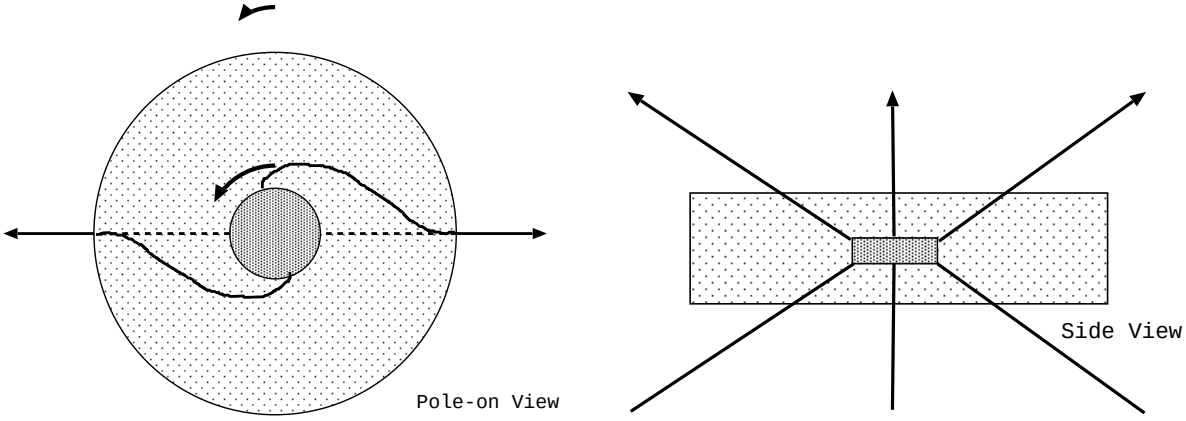

Figure 4.11: Pole-on (left) and side (right) views of the magnetic field lines, which drive the outflow.

Problem

Show that the angle between the isopotential line which passes the point $(r_0, 0)$ and the r-axis is equal to $\pm 60°$. Calculate the Taylor expansion of the effective potential near the point $(r_0, 0)$ and show that to satisfy $\phi(r_0 + \Delta r, \Delta z) = \phi(r_0, 0)$, $(\Delta z/\Delta r)^2$ must be equal to 3.

Angular Momentum Transfer

In the axisymmetric case, the poloidal (z, r) and toroidal (ϕ) components of the magnetic field $\boldsymbol{B}$ and current $\boldsymbol{j}$ are decoupled with each other. That is, the poloidal (B_p) and toroidal (B_ϕ) magnetic fields are made by the toroidal (j_ϕ) and poloidal (j_p) electric currents, respectively. As for the Lorentz force $\boldsymbol{j} \times \boldsymbol{B}$, the poloidal component comes from $j_\phi B_p$ or $j_p B_\phi$, while the toroidal component does from $\boldsymbol{j}_p \times \boldsymbol{B}_p$. Even if there is no toroidal magnetic field (thus no poloidal electric current), there exists the poloidal component of the Lorentz force, which acts as a pressure to counter-balance the self-gravity (§4.2). On the other hand, the toroidal component of the Lorentz force appears only the case with the poloidal electric current and thus toroidal component of magnetic field B_ϕ. This means that the angular momentum is transferred by the magnetic field only when B_ϕ exists. Equation (B.14) explains how the angular momentum density $\rho v_\phi r$ is transferred. The left-hand side of equation (B.14) represents the advection of the angular momentum density, while the right-hand side

$$\frac{r}{4\pi}\left[\frac{1}{r}\frac{\partial}{\partial r}(rB_\phi)B_r + \frac{\partial B_\phi}{\partial z}B_z\right] = \left(\frac{\boldsymbol{B}_p}{4\pi}\right)\cdot\nabla(rB_\phi), \tag{4.86}$$

represents the torque exerted on the gas parcel.

The induction equation of the magnetic field [eq.(B.17)] shows that B_ϕ is generated from poloidal magnetic field by the effect of rotational motion v_ϕ. This indicates that the angular momentum is transferred as follows:

1. The toroidal component of magnetic field B_ϕ is amplified by the dynamo process [equation (B.17)]. The magnetic field lines run like spiral viewing from the top like Figure 4.11.
2. Negative torque works near region attached to the fast-rotating disk, while positive one appears in the region connected to the radial magnetic field. The angular momentum is transferred from inside to outside along the same field line.

3. Angular momentum received by the gas near disk surface leads the excess centrifugal force which accelerate the gas. The disk inside which is affected by the negative torque loses its angular momentum and insufficient centrifugal force drives further accretion.

This angular momentum transfer on the same magnetic field has a character of *angular momentum redistribution.*

Centrifugal Radius

In a diffuse cloud, the centrifugal force does not play an important role. Consider a gas parcel whose specific angular momentum is equal to j. When the gas element contracts till the distance r from the center, the centrifugal force per mass of

$$\frac{v_\phi^2}{r} = \frac{j^2}{r^3}, \tag{4.87}$$

works. Contraction stops when the gravitational acceleration GM/r^2 is balanced by the centrifugal force. Its radius (centrifugal radius) is expressed as

$$r_c = \frac{j^2}{GM}. \tag{4.88}$$

Assuming that the disk is near the hydrostatic balance in z-direction, total column density is related to the volume density on the $z = 0$ plane as

$$\sigma = \left(\frac{2c_s^2\rho_c}{\pi G}\right)^{1/2}. \tag{4.89}$$

We can show that a nondimensional ratio of specific angular momentum to the mass is equal to the ratio of the free-fall time to the rotation period as follow:

$$\frac{c_s j}{GM} = \frac{c_s \omega_c r^2}{G\sigma\pi r^2} = \frac{\omega_c}{(2\pi G\rho_c)^{1/2}}. \tag{4.90}$$

Many numerical simulations confirm that the contracting disk in the runaway isothermal contraction phase has some 'universality.' The ratio of the free-fall time to the rotation period is approximately equal to

$$\frac{\omega_c}{(2\pi G\rho_c)^{1/2}} \simeq 0.3, \tag{4.91}$$

regardless of the initial conditions (Matsumoto, Nakamura, & Hanawa 1997). Thus, $c_s j/GM \simeq 0.3$. Finally, we can see the centrifugal radius as

$$r_c = \frac{GM}{c_s^2}\left(\frac{c_s j}{GM}\right)^2 \simeq 0.3\frac{GM}{c_s^2}, \tag{4.92}$$

increases with time in proportional to the mass M, because gas element with large j contracts later. As the centrifugal radius increases with time, the launching point of the outflow also expands with time.

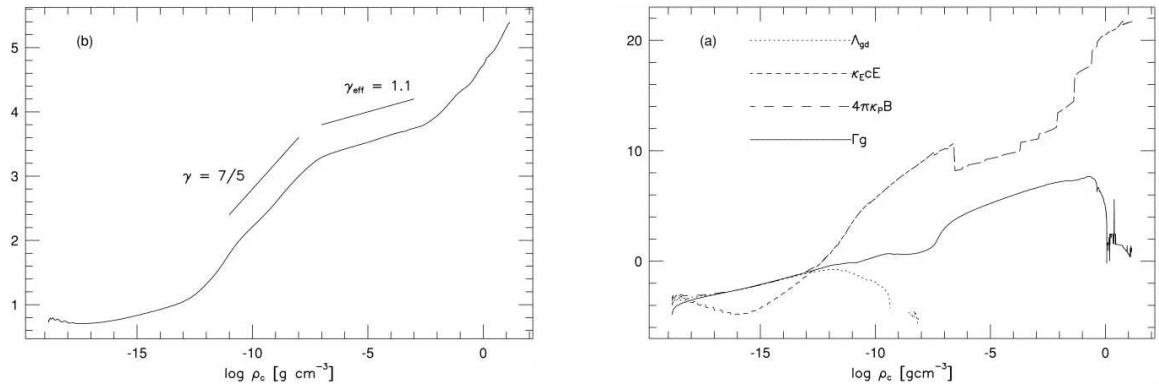

Figure 4.12: (Left) Relation between density and temperature at the center of the cloud. (Right) Cooling and heating rates, which are calculated for the cloud center are plotted against the density.

4.7.2 Entrainment Model

Models that a protostar is driving a jet and the jet transfers its momentum to the ambient material and forms a molecular outflow are called as entrainment models. From hydrodynamical calculations, De Young (1986) pointed out there are two mechanisms of entrainment. The ejected jet forms a bow shock and matter hit by the bow shock is accelerated promptly (prompt entrainment). His numerical simulations predicted that gas within the radius from the jet axis of $(1-3)\times$ jet radius is entrained in this mechanism. After the bow shock has passed away, slower mechanism of entrainment works, in which a turbulent layer is developed around the jet and the Reynolds stress in the layer transfers the momentum (Stahler 1994). In this mechanism, the ratio of entrained ambient gas to the injected mass by the jet is estimated as $(1/3-3)$ (De Young 1986).

4.8 Evolution to Star

In the proceeding sections we have seen the evolution from gas cloud to stars. However we were restricted to the isothermal gasses. To understand the change in the temperature, we have to consider the radiation which keeps the gas isothermal. Spherical symmetric radiative hydrodynamical simulations have been studied to understand the evolutionary path from interstellar cloud to star. Figure 4.12 (left) illustrates the relation between ρ and T obtained by Masunaga & Inutsuka (2000). Several characteristic power-laws are seen in the figure. Figure 4.13 plots the density and temperature distribution.

Isothermal Phase

Below $\rho \lesssim 10^{-13}\mathrm{g\,cm^{-3}}$, gas is essentially isothermal $T \propto \rho^0$. This corresponds to points number 1-3 of Figure 4.13. Since internal energy of gas is transferred to the thermal energy of dusts by collisions, the main coolant in this regime is the dust thermal radiation. The cooling rate per mass is

$$\Lambda = 4\kappa_p \sigma T^4, \tag{4.93}$$

where $\kappa_p(10\mathrm{K}) \sim 0.01\mathrm{cm^2\,g^{-1}}$ and σ represent Planck mean absorption coefficient and the Stephan-Boltzman constant. Main heating process for $\rho \lesssim 10^{-14}\mathrm{g\,cm^{-3}}$ is cosmic-ray heating: $\epsilon_{\mathrm{CR}} \sim 2\times$

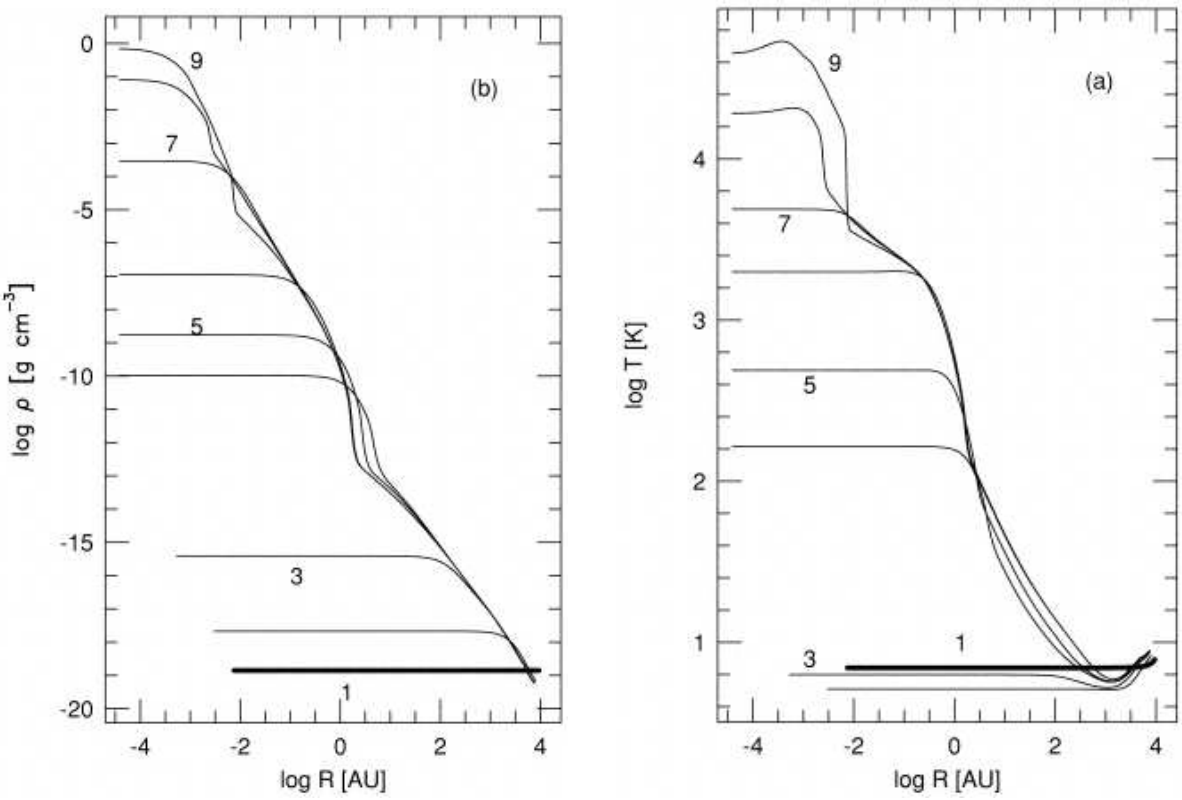

Figure 4.13: Dynamical evolution of a spherical cloud studied with RHD simulation. Density (left) and temperature (right) distributions are plotted against the radius.

$10^{-4}\mathrm{erg\,s^{-1}\,g^{-1}}$ (Goldsmith & Langer 1978). Balance between these two majors asks that temperature is constant as

$$T \sim 3\mathrm{K}\left(\frac{\epsilon_{\mathrm{CR}}}{2\times10^{-4}})\right)^{1/4}\left(\frac{\kappa_p}{0.01\mathrm{cm^2\,g^{-1}}})\right)^{1/2}. \tag{4.94}$$

Heating rate due to dynamical compression,

$$\Gamma = -p\frac{d(1/\rho)}{dt} \simeq c_s^2(4\pi G\rho), \tag{4.95}$$

increases according to the contraction and it balances with the above cooling at the density $\rho_{\mathrm{A}} \sim 10^{-14}\mathrm{g\,cm^{-3}}$ (Masunaga, Miyama, & Inutsuka 1998).

The cloud in this phase experiences the dynamical contraction as described in section 4.5. Structure of $\rho(r)$ and $v_r(r)$ is well represented by the Larson-Penston self-similar solution.

First Core

After $\rho \gtrsim \rho_A$, gas is no more isothermal and becomes adiabatic. Between $10^{-13}\mathrm{g\,cm^{-3}} \lesssim \rho \lesssim 10^{-9}\mathrm{g\,cm^{-3}}$, gas obeys the $\gamma = 5/3$ polytropes. Above the density $\rho \gtrsim \rho_{\mathrm{A}}$, the optical depth for the thermal radiation exceeds unity $\tau \gtrsim 1$ and radiative cooling can not compensate the compressional heating. As long as the temperature is low as $T \lesssim 100\mathrm{K}$, neither rotation nor vibration is excited for H_2 molecule. Even H_2 gas behaves like single-atom molecule. Thus $\gamma \simeq 5/3$.

Between $10^{-9}\mathrm{g\,cm^{-3}} \lesssim \rho \lesssim 10^{-7.5}\mathrm{g\,cm^{-3}}$, the exponent becomes $\gamma = 7/5$, which characterizes that the gas consists of two-atom molecule H_2.

In this phase, relatively large gas pressure supports against the gravity and the cloud becomes hydrostatic (points number 4-6 of Figure 4.13). This is called as "first core" made by the molecular hydrogen. The density structure of the first core is well represented by a polytrope sphere with the specific heat ratio of $\gamma = 7/5$ or the polytropic index $n = 2\frac{1}{2}$. From equation (C.11) in Appendix C.1, such a polytrope has a mass-density relation as

$$M_{c1} \propto \rho_c^{1/10}, \tag{4.96}$$

where M_{c1} and ρ_c represent, respectively, the mass of the first core and the central density. At the beginning, the core mass is equal to $M_{c1} \simeq 0.01 M_\odot$. As long as the mass increases a factor 3, the central density increases 5 orders of magnitude.

Second Collapse

For $10^{-7.5}\mathrm{g\,cm^{-3}} \lesssim \rho \lesssim 10^{-2.5}\mathrm{g\,cm^{-3}}$, the exponent becomes $\gamma = 1.1$. In this density range of $\rho \gtrsim 10^{-7.5}\mathrm{g\,cm^{-3}}$ the temperature exceeds 10^3K. Due to this temperature, the hydrogen molecules begin to dissociate and the dissociation process absorbs the energy. By this, gas becomes much softer ($\gamma \to 1$) than the first core. This introduces another dynamical contraction, the second collapse (points number 6-7 of Figure 4.13).

Second Core

After the dissociation is completed, the exponent becomes $\gamma = 5/3$. This gas forms a second core composed of atomic hydrogen, which is called the second core (points number 7-8 of Figure 4.13).

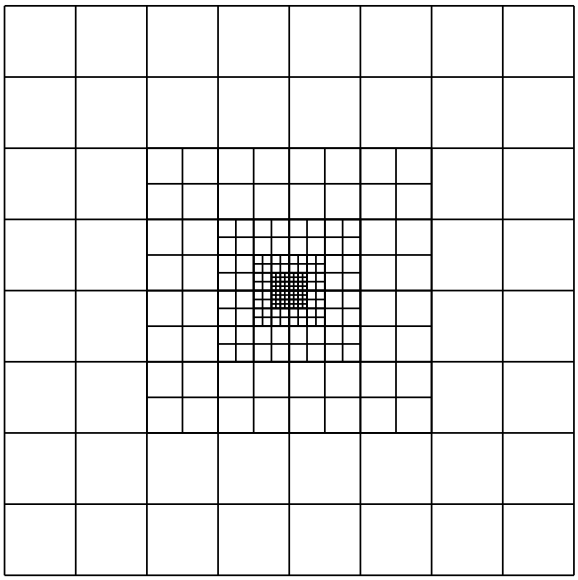

Figure 4.14: Explanation of nested grid method.

Since the accretion rate [eq.(4.75)] is proportional to c_s^3 or $T^{3/2}$, the accretion rates onto the second core $\dot{M}_{\rm 2nd}$ is larger than that of the first core $\dot{M}_{\rm 1st}$ as

$$\frac{\dot{M}_{\rm 2nd}}{\dot{M}_{\rm 1st}} \simeq 5 \times 10^3 \frac{(T/10^{3.5}{\rm K})^{3/2}}{(T/10{\rm K})^{3/2}}. \tag{4.97}$$

Thus, the first core disappears quickly and after that the gas begins to accrete onto the second core, which will be a protostar. However, this is the case of non-rotating, spherical symmetric cloud collapse. As previously seen, the angular momentum plays a crucial role and forms a disk. The evolution must be different completely for such a case.

4.9 Example of Numerical Simulation

We have described the cloud run-away collapse and succeeding accretion process In the latter phase, there is a possibility that the outflow is driven by the effect of magnetic Lorentz force. A restricted number of numerical simulation can simulate such evolution throughout. The size of the molecular cores $\sim$ 0.1pc is more than 3×10^4 times as large as the typical size of the first core $\sim$ 1AU. Therefore numerical scheme to calculate such process must have a large dynamic-range. In the finite-difference scheme, the spatial dynamic range is restricted by the number of the cells. Although at least $3 \times 10^5 \times 3 \times 10^5$ grid points (in 2D) seems necessary to resolve a factor of 3×10^4, to solve the MHD equation **with the Poisson equation** of the self-gravity have not been done. This is done by the Eularean nested-grid simulation. This method uses a finite number of grid systems with different spatial resolutions are prepared. Coarse grid covers whole the cloud and is to see a global structure. Fine grid covers only the central part of the cloud and is to see the fine-scale structure appeared near the center. Figure 4.14 explains grid cells of the nested grid method. The size of the cells of the n-th level grid (Ln) is taken equal to a half of those of the L$n-1$.

A cylindrical cloud with coaxial magnetic field in hydrostatic balance is studied. Rotation vector $\boldsymbol{\omega}$ and the magnetic field $\boldsymbol{B}$ are parallel to the symmetric axis of the cylinder (z-axis). For the

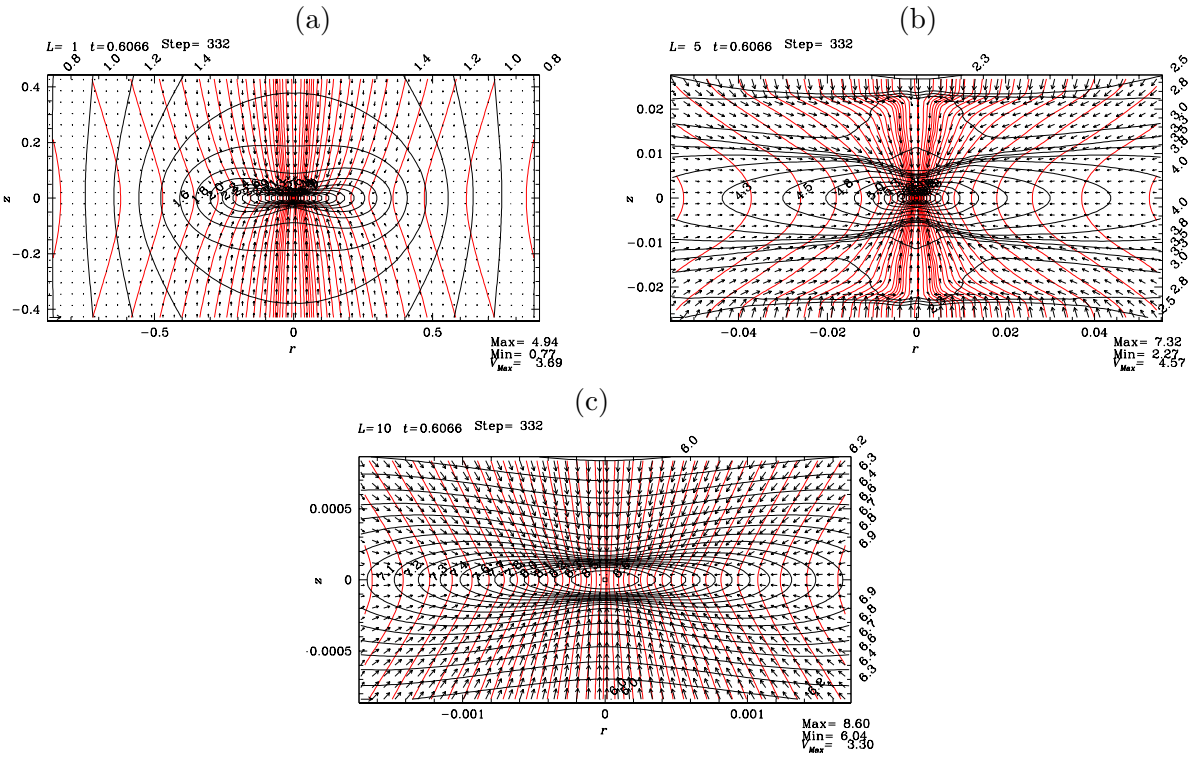

Figure 4.15: $\Omega_c = 10^{-13}\mathrm{rad\,s^{-1}}$, $B_c = 10\mu\mathrm{G}$, $\rho_c = 10^4\mathrm{H_2\ cm^{-3}}$, and $c_s = 190\mathrm{m\,s^{-1}}(T/10\mathrm{K})$. Snapshots at the time of $0.6066\tau_{\mathrm{ff}} = 1.061\mathrm{Myr}$ represented in different levels are shown: L1 (upper-left), L5 (upper-right), and L10 (bottom). The actual size of the frames of L5 (upper-right) and L10 (bottom) are, respectively, 1/16 and 1/512 smaller than that of L1 (upper-left). Magnetic field lines (dotted lines) and isodensity contours (solid lines) are presented as well as the velocity vectors by arrows.

energy equation, a double-polytropic equation of state is adopted, since the radiation hydrodynamical calculation (for example Masunaga & Inutsuka 2000) predicts $\rho - T$ relations like shown in Figure 4.12, which consists of a number of power-laws for some density ranges.

$$p = \begin{cases} c_s^2 \rho \quad (\text{for} \quad \rho < \rho_{\rm A}), \\ c_s^2 \rho_{\rm A} \left(\frac{\rho}{\rho_{\rm A}}\right)^{7/5} \quad (\text{for} \quad \rho > \rho_{\rm A}), \end{cases} \tag{4.98}$$

where we take $\rho_A = 10^{10}{\rm H_2\,cm^{-3}}$. Figure 4.15 is the model of $\Omega_c = 10^{-13}{\rm rad\,s^{-1}}$, $B_c = 10\mu$G, $\rho_c = 10^4{\rm H_2\ cm^{-3}}$, $c_s = 190{\rm m\,s^{-1}}(T/10{\rm K})$, and scale-length $H = 0.341{\rm pc}(c_s/190{\rm m\,s^{-1}})(\rho_c/10^4{\rm H_2\ cm^{-3}})^{-1/2}$. This is a snapshot of $0.6066\tau_{\rm ff} = 1.061$Myr. The cylindrical cloud breaks into pieces with a length in z-direction equal to the most unstable wavelength of the gravitational instability (Matsumoto, Nakamura, & Hanawa 1994) as

$$\lambda_{\rm max} \simeq \frac{2\pi(1+\alpha/2+\beta)^{1/2}}{0.72\left[(1+\alpha/2+\beta)^{1/3} - 0.6\right]^{1/2}} \frac{c_s}{(4\pi G\rho_c)^{1/2}}. \tag{4.99}$$

The magnetic fields prevent gas motions perpendicular to the field lines $\boldsymbol{B}$. Further, the centrifugal force works in the perpendicular direction to $\boldsymbol{\omega}$. A disk forms which running in the perpendicular direction to $\boldsymbol{B}$ and $\boldsymbol{\omega}$ and thus to the z-axis. Figure 4.15 illustrates a snapshot at the time of $0.6066\tau_{\rm ff} = 1.061$Myr. Level 1 grid (upper-left) captures the global structure of the contracting disk perpendicular to the z-axis. Close up view is shown in L5, which has 16 times finer spatial resolution (upper right). Since speed, v_z, of infalling gas is larger than the sound speed, a number of shock fronts are formed near $z \simeq 0.02H$ and $z \lesssim 0.01H$. Further inner structure is represented in L10 grid (bottom) which has 32 times finer resolution than L5. Another discontinuity in density is now forming near $z \sim 0.0002H$. Since gas inside of this discontinuity has the density larger than the critical density $\rho > \rho_{\rm A}$, in this phase the first core (p.93) begins to be formed. In the isothermal collapse phase, a characteristic power-law for the Larson-Penston self-similar solution is seen in the radial distributions of density as $\rho(r, z=0) \propto r^{-2}$, and $B_z(r, z=0) \propto r^{-1}$.

After $t > 0.6067\tau_{\rm ff}$ the first core is formed. Radial infall motion is accelerated toward the surface of the first core and the rotational motion v_ϕ also increases. This amplification promotes the toroidal magnetic field, B_ϕ. Since the torque is proportional to $(\boldsymbol{\nabla}\times B_\phi \boldsymbol{e}_\phi)\times \boldsymbol{B}_p$, the amplitude of the torque increases after the first core formation.

Structure just after ∼500 yr has passed from Figure 4.15 is shown in Figure 4.15 In $\tau \sim 500$ yr from the epoch of Figure 4.15, flow is completely changed and outflow is launched. Panel (b), which corresponds to a four-times close-up of panel (a), shows clearly that outflow is ejected from a region near $r \simeq 1.5 \times 10^{-4} H$ and $z \simeq 0.5 \times 10^{-4} H$. And the outflow vectors and the disk has an gngle of approximately 45 deg. The magneto-centrifugal wind model favors a small angle between the magnetic field and the disk, $\theta_{\rm mag} < 60$deg. This model predicts that the angle between the flow and the disk is also smaller than 60 deg. Numerical results is not inconsistent with this prediction of magneto-centrifugal wind model.

To see which force is driving such outflow, amplitudes of three forces are compared: the Lorentz force $\boldsymbol{F}_m = (\boldsymbol{\nabla} \times \boldsymbol{B})\times \boldsymbol{B}/4\pi$, the centrifugal force $\boldsymbol{F}_c = (\rho v_\phi^2/r)\boldsymbol{e}_r$, and the thermal pressure gradient $\boldsymbol{F}_t = -\nabla p$. The parallel components to the poloidal magnetic field of the three forces are as

$$\begin{aligned} \boldsymbol{F}_m \cdot \frac{\boldsymbol{B}_p}{|\boldsymbol{B}_p|} &= \frac{\boldsymbol{\nabla} \times \boldsymbol{B})\times \boldsymbol{B}}{4\pi} \cdot \frac{\boldsymbol{B}_p}{|\boldsymbol{B}_p|}, \\ &= -\frac{1}{8\pi r^2} \frac{\boldsymbol{B}_p}{\boldsymbol{B}_p|} \cdot \nabla (r B_\phi)^2 \end{aligned} \tag{4.100}$$

(Ustyugova et al. 1999)

$$\boldsymbol{F}_c \cdot \frac{\boldsymbol{B}_p}{|\boldsymbol{B}_p|} = \rho v_\phi^2 r \cdot \frac{B_r}{|\boldsymbol{B}_p|}, \tag{4.101}$$

and

$$\boldsymbol{F}_p \cdot \frac{\boldsymbol{B}_p}{|\boldsymbol{B}_p|} = -\nabla p \cdot \frac{\boldsymbol{B}_p}{|\boldsymbol{B}_p|}. \tag{4.102}$$

Figure 4.16 illustrates the largest force at each grid point. Centrifugal force dominated region (region C), which is shown by asterisk (*), overlaps the outflow region around point P1 ($z = 10^{-4}H$, $2.5 \times 10^{-4}H$). Just radially exterior to this region C, there is another region near point P2 ($z = 2 \times 10^{-4}H$, $3.5 \times 10^{-4}H$) filled with puls signs where the magnetic force is dominated (region M). Comparing with the flow vectors in the left, the strong outflow coincides with this region M and the above region C. Therefore, the outflow is driven by the centrifugal force and the Lorentz force (pressure gradient by toroidal magnetic fields).

Difference between models with different magnetic field strength but the same rotation speed is illustrated in Figure 4.17. Magnetic to thermal pressure ratio α is taken 1 [panels (a), and (d)], 0.1 [panels (b), and (e)], and 0.01 [panels (c), and (f)]. Panels (a), (b), (c) in the left column are snapshots when the central density reaches $\rho_{\rm A}$ while panels (d), (e), (f) in the right column show the structure after $\tau = 4.5 \times 10^{-3}\tau_{\rm ff} = 8000$yr passed. In the model with $\alpha = 1$, the outflow gas flows through a region whose shape resembles a capital letter U. This is similar to that observed in model ($\alpha = 1$ and $\Omega = 5$) shown in Figure 4.16. Decreasing the magnetic field strength $\alpha = 1 \rightarrow 0.1$ and $\rightarrow 0.1$, the shape of disk changes from a flat disk to a round ellipsoid. The model with neither magnetic field nor rotation shows a spherical contracting core. Outflow is also affected by decrease in magnetic field strength. Globally folded magnetic field lines are seen in the outflow region in panel (e). Smaller-scale structure folding the magnetic field lines develops in the outflow region in panel (f). The strucure seen in the polidal magnetic field is well correlated to the distribution of toroidal magnetic field strength. That is, a packet of strong B_ϕ pinch the gas and poloidal magnetic field lines radially inwardly. This means that the toroidal magnetic field is amplified by the rotation motion and becomes predominant over the poloidal one in the case with meak initial magnetic field. Thus, the whoop stress, which is expressed by the first term of the Lorentz force of equation(B.13) and comes from the tension of toroidal magnetic field, pinches the plasma contained inside of the loop of B_ϕ. For this case, the magnetic force dominant region is widely spread compared with the centrifugal force dominant region, which is far from the model with strong magnetic field. In this case, the magnetic pressure gradient plays an important role. Gas of outflow is ejected perpendicularly from the disk and forms flow similar to the capital letter I. In conclusion, U-type and I-type outflows are generated for strong magnetic model and weak magnetic model, respectively.

4.10 Evolution in the H-R diagram

4.10.1 Main Accretion Phase

Before Deuterium Ignition

Gas accreting onto the protostar generates energy as follows

$$L_{\rm acc} = \frac{GM_*\dot{M}_*}{R_*} \tag{4.103}$$

where M_*, R_* and $\dot{M}_*$ represent the mass and radius of protostar and the mass accretion rate.

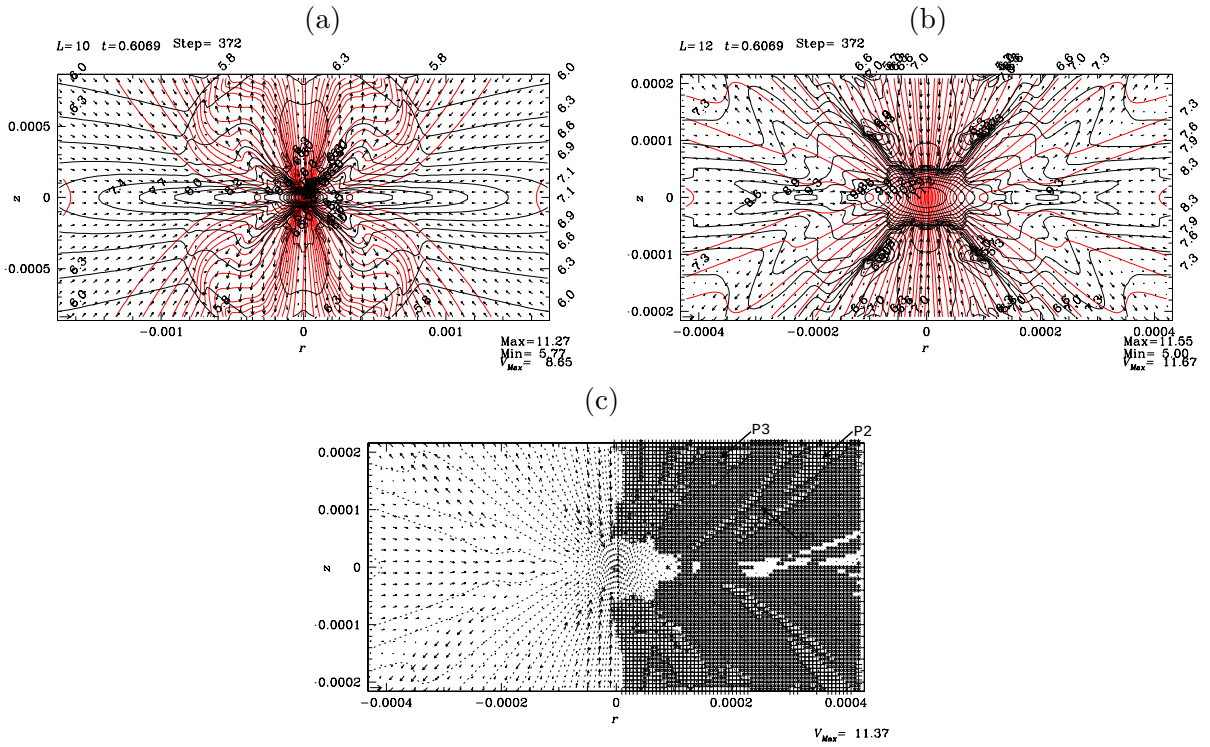

Figure 4.16: Continuation of the evolution shown in Fig.4.15. Snapshots at the time of $0.6069\tau_{\rm ff} = 1.066$Myr just ~ 500 yr after from Fig.4.15. Panel (a) plots the structure of L10 which is similar to Fig.4.15 (c). Spherical region inside $\sim 1.2 \times 10^{-3}H$ has been swept by the outflow. Panel (b) is a snapshot of L12 grid which has 4-times finer spatial resolution than L10 (a). In panel (c), we plotted magnetic force dominated region with '+', centrifugal force dominated with '*', and thermal pressure force dominated with blank ' '.

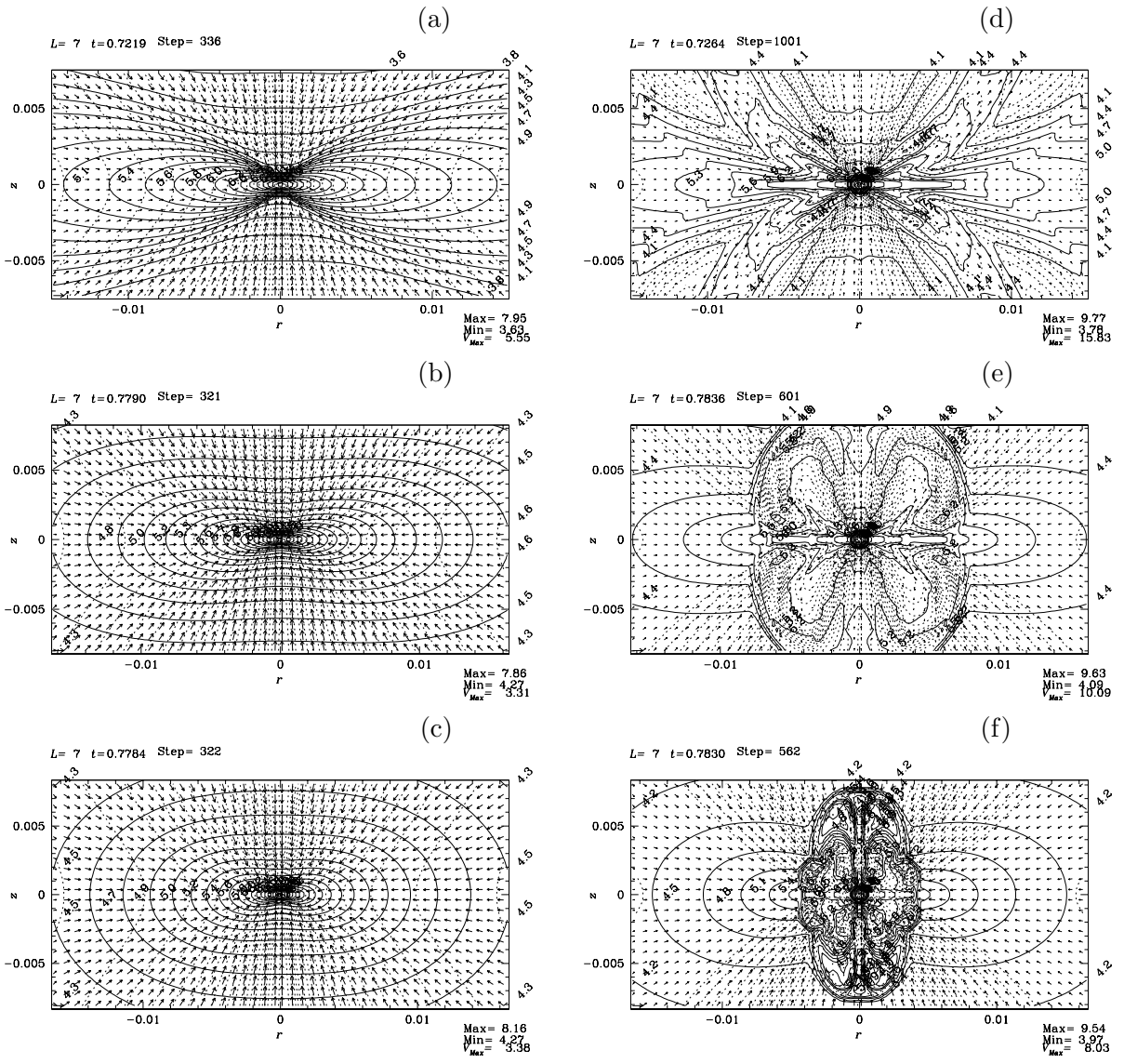

Figure 4.17: Difference in models with the same rotation speed $\Omega = 2 \times 10^{-14}\mathrm{rad\,s^{-1}}$ but different magnetic field strength ((a) and (d): $B_c = 10\mu$G, (b) and (e): 3μG, and (c) and (f): 1μG).

The central temperature increases with time. Finally thermonuclear fusion reaction of Deuterium $^2\mathrm{H}(p,\gamma)^3\mathrm{He}$ begins. Before Deuterium burning begins, the protostar is *radiative*, that is, the energy is transported radiatively.

When a fresh gas of Δm accrets, thermal energy of $\Delta U = GM_*\Delta m/R_*$ increases. Virial theorem (eq.[2.120]) requires the potential energy must decrease (increase in the absolute volume) at

$$\Delta W = -2\Delta U \simeq -\frac{GM_*\Delta m}{R_*/2}, \tag{4.104}$$

to achive a mechanical equilibrium. As a result, the fresh gas must contract to about half the radius at which the gas first joined the core (Stahler, Shu, & Taam 1980).

When the free-falling fresh gas accrets on the static star, an accretion shock forms. Since the gas temperature is increased with passing the shock front, temperature of the postshock gas, T_g , is much higher than that of the radiation, T_r. Thus, the postshock gas cools very effectively. The postshock region with $T_g > T_r$ is called radiative relaxation region. The outgoing luminosity at the accretion shock is much larger than that inside of the radiative relaxation region.

In the case of low mass stars since the Kelvin-Helmholtz contraction time $t_{K-H} \simeq GM_*^2/R_*L$ (L represent the luminosity at the base of the radiative relaxation region) is much longer than the acctretion time scale $t_{acc} \simeq M_*/\dot{M}_*$. This gives $L_{\rm acc} \simeq GM_*\dot{M}_*/R_*$ is much larger than L, which is consistent with the above statement that in the radiative relaxation region a large amount of accretion luminosity is radiated away. Since $t_{K-H} \gg t_{acc}$, the specific entropy inside the relaxation region is essentially frozen to that when the gas obtained passing through the relaxtaion region. Figure 4.18 taken from Stahler, Shu & Taam (1982) shows the distribution of the specific entropy against the accumulated mass M_r. The bottom curve corresponds to the state before the nuclear burning begins when no entropy generation occurs. The temperature increases with mass, bacause the star must be compressed to support an extra mass. After the temperature becomes high enough for Deuterium burning reaction $^2\mathrm{H}(p,\gamma)^3\mathrm{He}$ as $T \sim 10^6$K, an extra energy is liberated by the nuclear fusion reaction. This increases the specific entropy mainly in the offcenter region. Figure 4.18 clearly shows that shell Deuterium burning occurs at $M \sim 0.025M_\odot$.

After Deuterium Ignition

One gram of interstellar matter generates energy by the reaction of $^2\mathrm{H}(p,\gamma)^3\mathrm{He}$ as

$$\delta \equiv \left(\frac{1}{m_p\mu_H}\right)\left(\frac{n_{\rm D}}{n_{\rm H}}\right)\epsilon_{\rm D\to He} \simeq \tag{4.105}$$

where we used an energy per reaction of $^2\mathrm{H}(p,\gamma)^3\mathrm{He}$ as $\epsilon_{\rm D\to He} = 5.5$MeV and a composition of Deuterium of $n_{\rm D}/n_{\rm H} = 2.5\times10^{-5}$. This gives an estimate of the Deuterium-produced luminosity as

$$L_{\rm D} = \dot{M}\delta = 15L_\odot\left(\frac{\dot{M}}{10^{-5}M_\odot{\rm yr}^{-1}}\right), \tag{4.106}$$

for a star with the accretion rate of $\dot{M} \simeq 10^{-5}M_\odot{\rm yr}^{-1}$.

Entropy inversion $\partial s/\partial r < 0$ is unstable for the convection (see §2.7 in p.39). Convection is generated in the region of $\partial s/\partial M < 0$. Convective motion transfers the energy and the entropy. The specific entropy peak generated by the Deuterium burning is smoothed out by the convection. The convection induced with the Deuterium burning brings a fresh gas containing Deuterium into the hot Deuterium burning region. Thus, although the consent of Deuterium is small and Deuterium burning

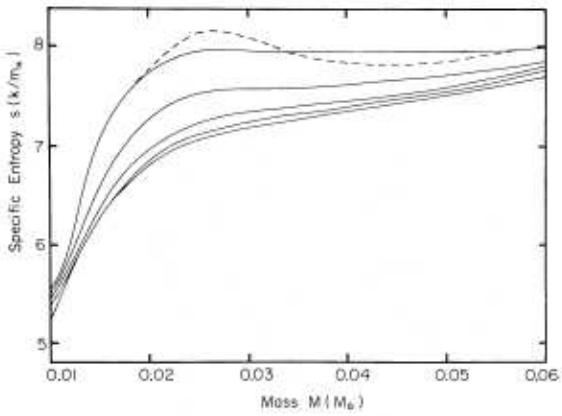

Figure 4.18: Specific entropy distribution is plotted against the accumulated mass (Stahler, Shu, & Taam 1982). The bottom curve shows the distribution at $t = 2.3 \times 10^4$yr ($M_* = 0.23 M_\odot$). The top curve is for $t = 3.4 \times 10^4$yr. The dashed curve indicates the entropy distribution if no convection is generated. While, the solid curves represent that of new distribution achieved with convection.

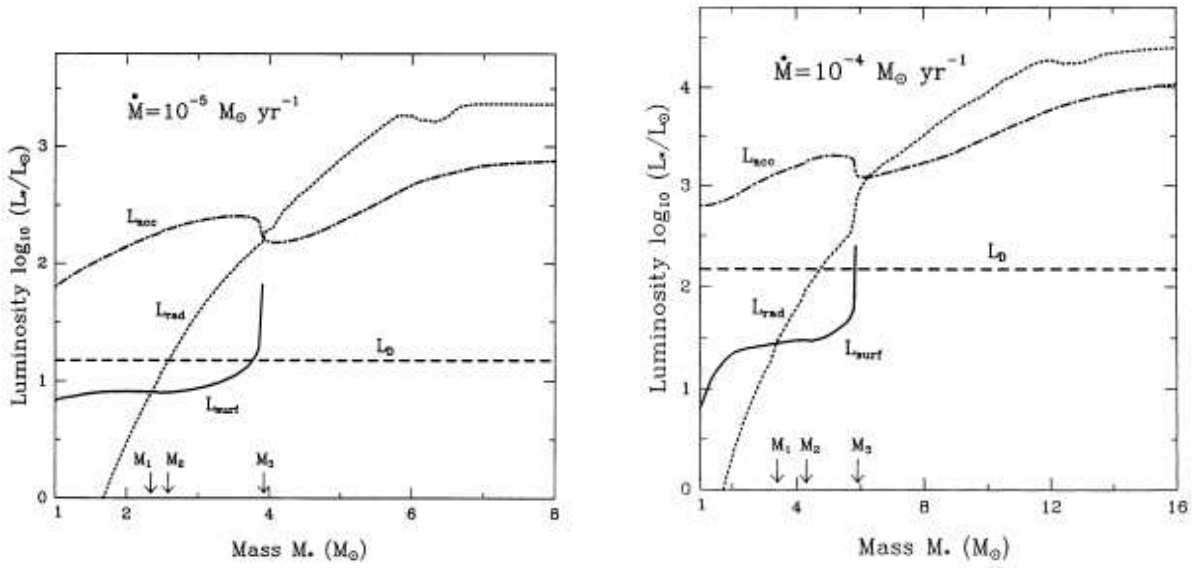

Figure 4.19: Luminosities in protostars accreting at $\dot{M}_* = 10^{-5} M_\odot \mathrm{yr}^{-1}$ (left) and $\dot{M}_* = 10^{-4} M_\odot \mathrm{yr}^{-1}$ (right) (Palla & Staler 1993). Accretion luminosity $L_{\rm acc}$, Deuterium burning luminosity $L_{\rm D}$, maximum radiatively transferable luminosity $L_{\rm rad}$ and luminosity at the surface $L_{\rm surf}$ are plotted.

could not continue long, Deuterium burning continues actually as long as the convection can mix the outer Deuterium rich fresh gas into the burning region due to the convection.

In Figure 4.19, luminosities in protostars accreting at $\dot{M}_* = 10^{-5} M_\odot \mathrm{yr}^{-1}$ (left) and $\dot{M}_* = 10^{-4} M_\odot \mathrm{yr}^{-1}$ (right) are plotted (Palla & Stahler 1993). $L_{\rm rad}$ represents the maximum luminosity transferable radiatively for a star with mass M_* and radius R_* as

$$L_{\rm rad} \sim 1 L_\odot \left(\frac{M_*}{1 M_\odot}\right)^{11/2} \left(\frac{R_*}{R_\odot}\right)^{-1/2}, \tag{4.107}$$

where the Krammers opacity $\kappa \propto \rho T^{-3.5}$ is applied for stars with $M \lesssim 5 M_\odot$. Actual luminosity at the surface of the star

$$L_{\rm surf} = 4\pi R_*^2 T_{\rm eff}^4, \tag{4.108}$$

is larger than $L_{\rm rad}$ for low mass stars ($M_* < M_1 = 2.4 M_\odot$ for $\dot{M}_* = 10^{-5} M_\odot \mathrm{yr}^{-1}$ and $M_1 = 3.4 M_\odot$ for $\dot{M}_* = 10^{-4} M_\odot \mathrm{yr}^{-1}$). Excess energy is transferred by the convection, $L_{\rm surf} = L_{\rm rad} + L_{\rm con}$. This figure also shows that except for extremely low-mass object the accretion luminosity is the major energy source over Deuterium burning $L_{\rm acc} > L_{\rm D}$. Since massive objects with $M_* > M_3$ satisfies $L_{\rm rad} \simeq L_{\rm surf} > L_{\rm acc}$, interior of such stars are fully radiative (energy is transferred by the radiation). $M_3 = 3.9 M_\odot$ for $\dot{M}_* = 10^{-5} M_\odot \mathrm{yr}^{-1}$ and $M_3 = 5.9 M_\odot$ for $\dot{M}_* = 10^{-5} M_\odot \mathrm{yr}^{-1}$.

Figure 4.20 (left) illustrates how the Deuterium burning in protostars evolves. Accumulating infalling gas and increasing M_*, the structure of protostars is changed. (a) in low-mass stars, convection feeds the Deuterium of the accreting matter to the burning center. (b) as increasing the mass and thus the temperature, the opacity of the stellar interior decreases. Finally a radiative zone appears and it prevents from mixing Deuterium. (c) as a consequence, central Deuterium is depleted and energy generation rate is reduced. Thus the central region becomes radiative. (d) For higher mass stars, Deuterium ignites as a shell source just outside the radiative central region. Due to this Deuterium shell burning, which is similar to the Hydrogen shell burning in the red giants, radius of the protostar expands. Figure 4.20 (right) plots the mass-radius relation of a protostar with accretion rate of $\dot{M}_* = 10^{-5} M_\odot \mathrm{yr}^{-1}$. The left open circle represents the beginning of central Deuterium burning (state a). On the second circle, radiative barrier appears (state b) and Deuterium shell burning begins. Beyond the mass, the radius swells dramatically. Further increase in the mass increases the gravity and the radius shrinks. At the third open circle, Hydrogen begins to burn at the center of the protostar.

In the HR diagram, the mass-radius relation for the protostars shown in Figure 4.20(right) corresponds to the dotted line (Fig.4.21). Observed premain-sequence stars: T Tauri stars ($M_* \lesssim 2 M_\odot$) and Herbig Ae/Be stars ($2 M_\odot \lesssim M_* \lesssim 5 M_\odot$) distribute below the dotted line. Thus, this line is often called the birth line for stars. In Figure 4.21, evolutionary tracks without mass accretion $\dot{M} = 0$ are plotted from the birth line. Modulation of the birth line is related to the swell and shrink of radius shown in Figure 4.20. That is, increase of luminosity around $M \simeq 1 M_\odot$ corresponds to the first swell after Deuterium burning begins (between the first and second open circles). Another increase around $M \simeq 2.5 M_\odot$ is related to the Deuterium shell burning (after the second open circle).

4.10.2 Premain-sequence Evolution

Premain-sequence evolutionary path is understood as follows: Consider a situation that a star with M_* is left when accretion stops. Figure 4.19 indicates that a less-massive star with $M_* < M_1$ is fully convective. Thus, this evolves along the convective Hayashi track (Hayashi 1961) down to the main-sequence. In contrast, a massive star with $M_* > M_3$ (Fig.4.19) is fully radiative and evolves along the radiative Henyey track (Henyey, LeLevier, & Levee 1955) to the main-sequence. These

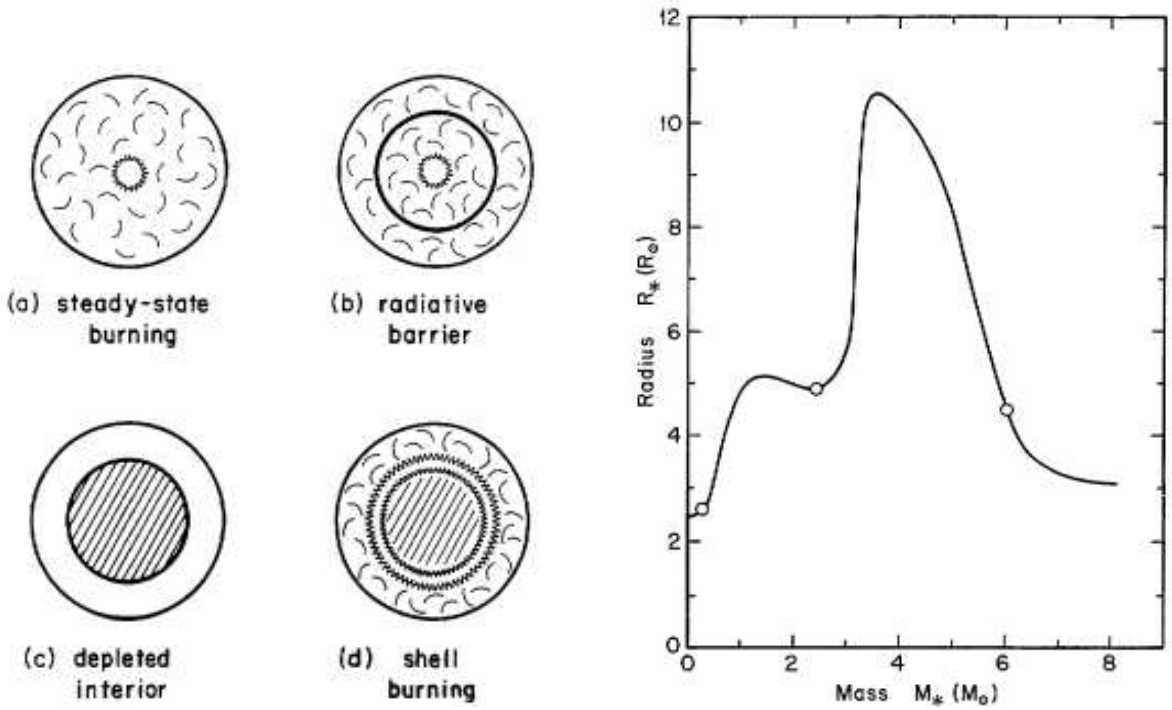

Figure 4.20: Schematic view of Deuterium burning in protostars (left). Evolution of the radius of a protostar is plotted against its mass (right). Both figures are taken from Palla & Stahler (1990).

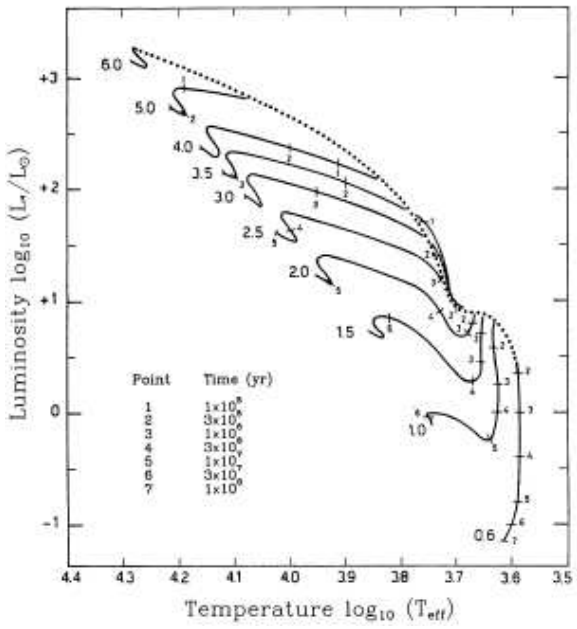

Figure 4.21: Premain-sequence evolutionary path in the H-R diagram. (Palla & Staler 1993). Evolution of stars with different masses from $0.6M_\odot$ to $6M_\odot$ are calculated from the birth line (dotted line).

differences are clearly indicated in Figure 4.21. We can see veritical Hayashi track is seen essentially for stars with $M \lesssim 1.5M_\odot$. Massive stars with $M \gtrsim 2.5M_\odot$ evolve to the upper-left direction along the Henyey track.

Bibliography

[1] Alves, J., Lada, C.J., & Lada, E.A. 2001, *Internal Structure of a Cold Dark Molecular Cloud Inferred from Extinction of background Starlight*, Nature, 409, 159

[2] Alves, J., Lada, C.J., Lada, E.A., Kenyon, S.J., & Phelps, R. 1998, *Dust Extinction and Molecular Cloud Structure: L977*, ApJ, 506, 292

[3] André, P. 1994, *Observations of Protostars and Protostellar Stages* in "The Cold Universe," eds. T. Montmerle, C.J.Lada, I.F.Mirabel, & J.Tran Thanh Van, Editions Frontières, p.179

[4] Binney, J., & Tremaine, S. 1988, *Galactic Dynamics*, Princeton Univ. Pr. Chapter 6.

[5] Bonnor W. B. 1956, *Boyle's Law and Gravitational Instability*, MNRAS, 116, 351

[6] Blandford, R. D., & Payne, D. G. 1982, *Hydromagnetic Flows from Accretion Discs and the Production of Radio Jets*, MNRAS, 199, 883

[7] Chandler, C. J., & Sargent, A. I. 1993, *The Small-Scale Structure and Kinematics of B335*, ApJ, 414, L29

[8] Chandrasekhar, S. 1939, *An Introduction to the Study of Stellar Structure*, (Univ. of Chicago Pr.; Chicago)

[9] Cudworth, K. M., & Herbig, G. 1979, *In Two Large-Proper-Motion Herbig-Haro Objects*, AJ, 84, 548

[10] De Young, D. S. 1986, *Mass Entrainment in Astrophysical Jets*, ApJ, 307, 62

[11] Ebert R. 1955, *er die Verdichtung von H I-Gebieten. Mit 5 Textabbildungen*, Z. Astrophys., 37, 217

[12] Elmegreen, B.G.; Seiden, P.E. & Elmegreen, D.M. 1989, *Spiral Arm Amplitude Variations and Pattern Speeds in the Grand Design Galaxies M51, M81, and M100*, ApJ, 343, 602

[13] Fiege, J.D., & Pudritz, R.E. 2001, *Helical Fields and Filamentary Molecular Clouds - I*, MNRAS, 311, 85

[14] Fridlund, C.V.M., & Liseau, R. 1998, *Two Jets from the Protostellar System L1551 IRS5*, ApJL, 499, 75

[15] Goldsmith, P. F., & Langer, W. D. 1978, *Molecular Cooling and Thermal Balance of Dense Interstellar Clouds,* ApJ, 222, 881

[16] Gordon, M.A., & Burton, W.B. 1976, *Carbon Monoxide in the Galaxy. I - The Radial Distribution of CO, H2, and Nucleons*, ApJ, 208, 346

[17] Haisch, K. E., Lada, E. A., & Lada, C. J. 2001, *Disk Frequencies and Lifetimes in Young Clusters*, ApJ, 553, L153

[18] Hanawa, T. 1999, *Star Formation*, in "Active Universe" in Japanese (Shokabo, Tokyo) ed. by K. Shibata, J. Fukue, R. Matsumoto, & S. Mineshige

[19] Hartmann, L. 1998, *Accretion Processes in Star Formation*, Cambridge U.Pr.

[20] Hayashi, C. 1961, *Stellar Evolution in Early Phases of Gravitational Contraction*, PASJ, 13, 450

[21] Heithausen, A., Bensch, F., Stutzki, J., Falgarone, E., & Panis, J.F. 1998, *The IRAM Key Project: Small-Scale Structure of Pre-Star Forming Regions Combined Mass Spectra and Scaling Laws*, AAp, 331, L65

[22] Henriksen, R., Andre, P., & Bontemps, S. 1997, *Time-Dependent Accretion and Ejection Implied by Pre-Stellar Density Profiles*, AAp, 323, 549

[23] Henyey, L. G., Lelevier, R. Levee, R. D. 1955, *The Early Phases of Stellar Evolution*, PASP, 67, 154

[24] Hirano, N., Kameya, O., Nakayama, M., & Takakubo, K. 1988, *Bipolar outflow in B335*, ApJL, 327, L69

[25] Honma, M., Sofue, Y., & Arimoto, N. 1995, *The Molecular Front in Galaxies. II. Galactic-scale Gas Phase Transition of HI and* H_2, AAp, 304, 1

[26] Hunter, C. 1977, *The Collapse of Unstable Isothermal Spheres*, ApJ, 218, 834

[27] Itoh, Y. et al. 2000, *A Pair of Twisted Jets of Ionized Iron from L 1551 IRS 5*, PASJ, 52, 81

[28] Kennicutt, R.C. 1998, *The Global Schmidt Law in Star-forming Galaxies*, ApJ, 498, 541

[29] Kennicutt, R.C., Tamblyn, P., & Congdon, C.W. 1994, *Past and Future Star Formation in Disk Galaxies*, ApJ, 435, 22

[30] Kramer, C., Stutzki, J., Rohrig, R., & Corneliussen, U. 1998, *Clump Mass Spectra of Molecular Clouds*, AAp, 329, 249

[31] Lada, C.J. 1999, *The Formation of Low Mass Stars*, in "The Origin of Stars and Planetary Systems" ed. C.J. Lada & N.D. Kylafis, (Kluwer) p.143

[32] Larson, R. B. 1981, *Turbulence and Star Formation in Molecular Clouds*, MNRAS, 194, 809

[33] Loren, R. B. 1989, *The Cobwebs of Ophiuchus. I - Strands of* ^{13}CO *- The Mass Distribution*, ApJ, 338, 902

[34] Masunaga, H. & Inutsuka, S. 2000, *A Radiation Hydrodynamic Model for Protostellar Collapse. II. The Second Collapse and the Birth of a Protostar*, ApJ, 531, 350

[35] Masunaga, H., Miyama, S. M., & Inutsuka, S. 1998, *A Radiation Hydrodynamic Model for Protostellar Collapse. I. The First Collapse,* ApJ, 495, 346

[36] Matsumoto, T., Hanawa, T., & Nakamura, F. 1997, *Gravitational Contraction of Rotating Clouds: Formation of Self-similarly Collapsing Disks*, ApJ, 478, 569

[37] Matsumoto, T., Nakamura, F., Hanawa, T. 1994, *Fragmentation of a Magnetized Filamentary Molecular Cloud Rotating around its Axis*, PASJ, 46, 243

[38] Mizuno, A., Onishi, T., Hayashi, M., Ohashi, N., Sunada, K., Hasegawa, T., & Fukui, Y. 1994, *Molecular Cloud Condensation as a Tracer of Low Mass Star Formation*, Nature, 368, 719

[39] Mizuno, A. et al. 1995, *Overall Distribution of Dense Molecular Gas and Star Formation in the Taurus Cloud Complex*, ApJL, 445, L161

[40] Mouschovias, T. Ch. 1976a, *Nonhomologous contraction and equilibria of self-gravitating, magnetic interstellar clouds embedded in an intercloud medium: Star formation. I Formulation of the problem and method of solution*, ApJ, 206, 753

[41] Mouschovias, T. C. 1976b, *Nonhomologous Contraction and Equilibria of Self-Gravitating, Magnetic Interstellar Clouds Embedded in an Intercloud Medium: Star Formation. II - Results*, ApJ, 207, 141

[42] Mouschovias, T. Ch., Paleologou, E. V., & Fiedler, R. A. 1985, *The Magnetic Flux Problem and Ambipolar Diffusion during Star Formation - One-Dimensional Collapse. II - Results*, ApJ, 291, 772

[43] Motte, F., & André, P. 2001, *The Circumstellar Environment of Low-Mass Protostars: A Millimeter Continuum Mapping Survey*, AAp, 365, 440

[44] Motte, F., André, P., Ward-Thompson, D.,& Bontemps, S. 2001, *A SCUBA Survey of the NGC 2068/2071 Protoclusters*, AAp, 372, L41

[45] Myers, P.C. 1978, *A Compilation of Interstellar Gas Properties*, ApJ, 225, 380

[46] Mundt, R., & Fried, J. W. 1983, *Jets from Young Stars*, ApJ, 274, 83

[47] Nakano, T. 1979, *Quasistatic Contraction of Magnetic Protostars due to Magnetic Flux Leakage - Part One - Formulation and an Example*, PASJ, 31, 713

[48] Nakano, T. Nishi, R., Umebayashi, T. 2002, *Mechanism of Magnetic Flux Loss in Molecular Clouds*, ApJ, 572, 199

[49] Ogino, S., Tomisaka, K., & Nakamura, F. 1999, *Gravitational Collapse of Spherical Interstellar Clouds* PASJ, 51, 637.

[50] Ohashi, N., Hayashi, M., Ho, P.T.P., Momose, & M., Hirano, N. 1996, *Possible Infall in the Gas Disk around L1551 IRS 5*, ApJ, 466, 957

[51] Ohashi, N. Lee, S. W., Wilner, D. J. & Hayashi, M. 1999, *CS Imaging of the Starless Core L1544: an Envelope with Infall and Rotation*, ApJL, 518, L410

[52] Onishi, T., Mizuno, A., Kawamura, A., Ogawa, H., Fukui, Y. 1996, *A* $C^{18}O$ *Survey of Dense Cloud Cores in Taurus: Core Properties*, ApJ, 468, 815

[53] Onishi, T., Mizuno, A., Kawamura, A., Tachihara, K., & Fukui, Y. 2002, *A Complete Search for Dense Cloud Cores in Taurus*, ApJ, 575, 950

[54] Paleologou, E. V., & Mouschovias, T. Ch. 1983, *The Magnetic Flux Problem and Ambipolar Diffusion during Star Formation - One-Dimensional Collapse. I - Formulation of the Problem and Method of Solution*, ApJ, 275, 838

[55] Palla, F. & Stahler, S. W. 1990, *The Birthline for Intermediate-Mass Stars*, ApJ, 360,47

[56] Palla, F. & Stahler, S. W. 1993, *The Pre-Main-Sequence Evolution of Intermediate-Mass Stars*, ApJ, 418, 414

[57] Reipurth, B., Yu, K.C., Rodríguez, L.F., Heathcote, S., & Bally, J. 1999, *Multiplicity of the HH 111 Jet Source: it Hubble Space Telescope NICMOS Images and VLA Maps*, AAp, 352, L83

[58] Saito, M., Sunada, K., Kawabe, R., Kitamura, Y., & Hirano, N. 1999, *he Initial Conditions for Formation of Low-Mass Stars: Kinematics and Density Structure of the Protostellar Envelope in B335*, ApJ, 518, 334

[59] Sanders, D.B., Scoville, N.A., & Solomon, P.M. 1985, *Giant Molecular Clouds in the Galaxy. II. Characteristics of Discrete Features*, ApJ, 289, 373

[60] Schmidt, M. 1959, *The Rate of Star Formation*, ApJ, 129, 243

[61] Shu, F. H. 1978, *Self-similar Collapse of Isothermal Spheres and Star Formation*, ApJ, 214, 488

[62] Shu, F. H. 1983, *Ambipolar Diffusion in Self-Gravitating Isothermal Layers*, ApJ, 273, 202

[63] Shu, F.H., Milione, V., & Roberts, W.W.,Jr. 1973, *Nonlinear Gaseous Density Waves and Galactic Shocks*, ApJ, 183, 819

[64] Snell, R. L., Loren, R. B., & Plambeck, R. L. 1980, *Observations of CO in L1551 - Evidence for Stellar Wind Driven Shocks*, ApJ, 239, 17

[65] Spitzer, L. Jr. 1978, *Physical Processes in the Interstellar Medium*, Wiley, Cahper 13.

[66] Stahler, S. W. 1983, *The Birthline for Low-mass Stars*, ApJ, 274, 822

[67] Stahler, S. W. 1994, *The Kinematics of Molecular Outflows*, ApJ, 422, 616

[68] Stahler, S. W., Shu, F. H., & Taam, R. E. 1980, *The Evolution of Protostars. II - The Hydrostatic Core*, ApJ, 242, 226

[69] Stutzki, J. & Guesten, R. 1990, *High Spatial Resolution Isotopic CO and CS Observations of M17 SW - The Clumpy Structure of the Molecular Cloud Core*, ApJ, 356, 513

[70] Tafalla, M., Mardones, D., Myers, P. C., Caselli, P., Bachiller, R. & Benson, P. J. 1998, *L1544: A Starless Dense Core with Extended Inward Motions*, ApJ, 504, 900

[71] Tamura, M., Hough, J.H., Hayashi, S.S., 1995, *Millimeter Polarimetry of Young Stellar Objects: Low-Mass Protostars and T Tauri Stars*, ApJ, 448, 346

[72] Tomisaka, K. 2002, *Collapse of Rotating Magnetized Molecular Cloud Cores and Mass Outflows*, ApJ, 575, 306

[73] Tomisaka, K., Ikeuchi, S., & Nakamura, T. 1988, *The Equilibria and Evolutions of Magnetized, Rotating, Isothermal Clouds. I - Basic Equations and Numerical Methods*, ApJ, 326, 208

[74] Tomisaka, K., Ikeuchi, S., & Nakamura, T. 1988, *Equilibria and Evolutions of Magnetized, Rotating, Isothermal Clouds. II - The Extreme Case: Nonrotating Cloud*, ApJ, 335, 293

[75] Tomisaka, K., Ikeuchi, S., & Nakamura, T. *The Equilibria and Evolutions of Magnetized, Rotating, Isothermal Clouds. IV - Quasi-Static Evolution*, ApJ, 362, 202

[76] Toomre, A. 1981, *What Amplifies the Spirals*, in "The Structure and Evolution of Normal Galaxies" Cambridge U.Pr., 1981, pp.111-136

[77] Tothill, N. F. H., White, G. J., Matthews, H. E., McCutcheon, W. H., McCaughrean, M. J., & Kenworthy, M. A. 2002, *The Structure and Evolution of the Lagoon Nebula. I. Submillimeter Continuum and CO Line Mapping*, ApJ, 580, 285

[78] Ustyugova, G. V., Koldoba, A. V., Romanova, M. M., Chechetkin, V. M., & Lovelace, R. V. E. 1999 *Magnetocentrifugally Driven Winds: Comparison of MHD Simulations with Theory*, ApJ, 516, 221

[79] Ward-Thompson, D., Kirk, J.M., Crutcher, R.M., Greaves, J.S., Holland, W.S., André, P. 2000, *First Observations of the Magnetic Field Geometry in Prestellar Cores*, ApJL, 537, L135

[80] Weintraub, D.A., Goodman, A.A., & Akeson, R.L. 1999, *Polarized Light from Star-Forming Regions*, in Protostars and Planets IV, ed. V.Mannings, A.P.Boss, & S.S. Russell, U. Arizona Pr. pp.247-271

[81] Whitworth, A., & Summers, D. 1985, *Self-Similar Condensation of Spherically Symmetric Self-Gravitating Isothermal Gas Clouds*, MNRAS, 214, 1

[82] Wolf, S., Launhardt, R. & Henning, T., 2003, *Magnetic Field Evolution in Bok Globules*, ApJ, 592, 233

[83] Yun, J. L., & Clemens, D. P. 1994, *Outflows from Young Stellar Objects in BOK Globules: Maps*, ApJS, 92, 145

[84] Zhou, S. 1995, *Line Formation in Collapsing Cloud Cores with Rotation and Applications to B335 and IRAS 16293-2422*, ApJ, 442, 685

[85] Zhou, S., Evans, N.J.,II, Koempe, C., & Walmsley, C.M. 1993, *Evidence for Protostellar Collapse in B335*, ApJ, 404, 232